Julio - Septiembre 2023
Volumen 62
Número 3

July - September 2023
Volume 62
Number 3

Geofísica Internacional

Revista Trimestral Publicada por el Instituto de Geofísica de la Universidad Nacional Autónoma de México
Quarterly Journal Published by the Institute of Geophysics of the National Autonomous University of Mexico

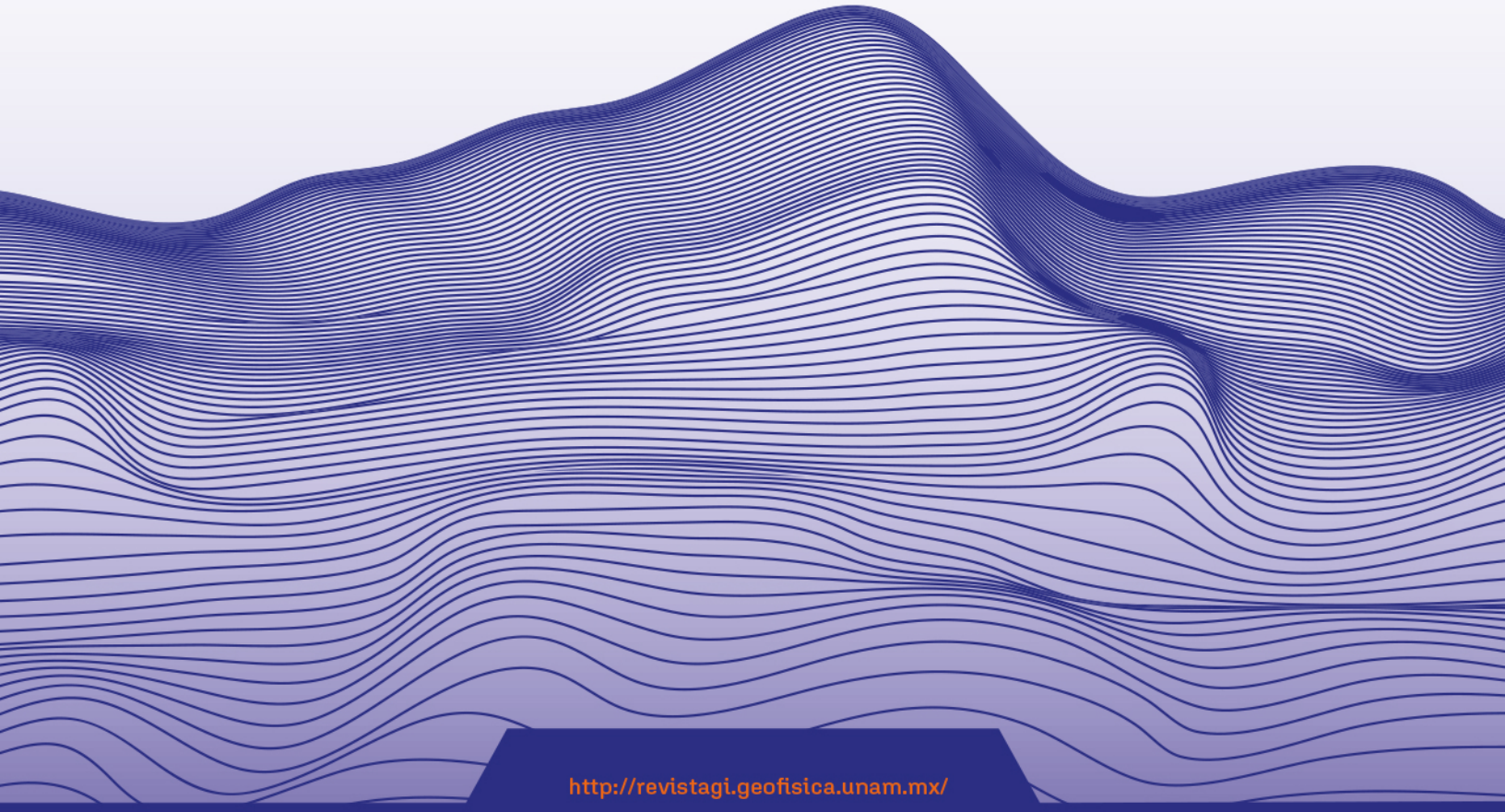

http://revistagi.geofisica.unam.mx/

ISSN 2954-436X

MÉXICO MEXICO

— Geofísica Internacional —

GEOFÍSICA INTERNACIONAL, Año 62, Vol. 62, Núm. 3, julio - septiembre de 2023 es una publicación trimestral, editada por la Universidad Nacional Autónoma de México, Ciudad Universitaria, Alcaldía Coyoacán, C.P. 04510, Ciudad de México, a través del Instituto de Geofísica, Circuito de la Investigación Científica s/n, Ciudad Universitaria, Alcaldía Coyoacán, C.P. 04510, Ciudad de México, Tel. (55)56 22 40 36. URL: http://revistagi.geofisica.unam.mx, correo electrónico: revistagi@igeofisica.unam.mx. Editor responsable: Saúl Armendáriz Sánchez. Certificado de Reserva de Derechos al uso Exclusivo del Título: 04-2022-081610251200-102, eISSN: 2954-436X, otorgados por el Instituto Nacional del Derecho de Autor (INDAUTOR). Responsable de la última actualización, Minerva Castro Escamilla Editora Técnica. Fecha de la última modificación: 1 de julio de 2023, Circuito de la Investigación Científica s/n, Ciudad Universitaria, Alcaldía Coyoacán, C.P. 04510, Ciudad de México.

https://doi.org/10.22201/igeof.2954436xe.2023.62.3

Geofísica Internacional
Vol. 62, Núm. 3, julio - septiembre de 2023

Contents

Geofísica Internacional (2023) **62-3**: 519 - 523

Significance estimation for the Kullback-Leibler divergence: the Poissonian case in seismological studies

F. A. Nava[1]*

Abstract

The Kullback-Leibler divergence, κ, is a widely used measure of the difference between an observed probability distribution and a reference one; κ=0 when the two distributions are equal, but it has no upper limit to help interpret the significance of any other κ value. Using as an example the problem of distinguishing clustering or gaps in the time occurrence of earthquakes from seismicity uniformly distributed in time, a Monte Carlo method for evaluating the significance of a particular κ value is presented, a method that takes into account the number of classes in the distributions and the length of the sample. Application of this method yields a probability according to which the hypothesis of the observed distribution being a realization of the reference one can be discarded or accepted with a quantitative degree of confidence. This method, and two possible reference values, are presented using the Poisson distribution as an example, but they can be used for other reference distributions.

Key words: Kullback-Leibler divergence, Poisson distribution, Statistical seismology.

Resumen

La divergencia Kullback-Leibler, κ, es una medida ampliamente usada de la diferencia entre una distribución de probabilidad observada y otra distribución de referencia; κ=0 cuando ambas distribuciones son iguales, pero no tiene un valor tope que permita interpretar la significatividad de cualquier otro valor de κ. Usando como ejemplo el problema de distinguir cúmulos o vacancias en la ocurrencia temporal de sismos de sismicidad distribuida con probabilidad uniforme en el tiempo, se presenta un método de Monte Carlo para evaluar la significatividad de algún valor de κ, método que toma en cuenta el largo de la muestra. Este método y dos posibles valores de referencia son presentados usando la distribución de Poisson como ejemplo, pero pueden ser utilizados con cualquier otra distribución de referencia.

Palabras clave: Divergencia Kullback-Leibler, Distribución de Poisson, Sismología estadística.

Introduction

In many kinds of statistical studies, including seismological ones, it is a common task to compare some observed probability distribution $P=\{p_j;\ j=1,\ldots,M\}$ with some reference distribution $\Pi=\{\pi_j;\ j=1,\ldots,M\}$, and the difference between them is often measured by using the Kullback-Leibler divergence (K-L) κ:

$$\kappa \sum_{j=1}^{M} p_j \log_2 \frac{p_j}{\pi_j} \qquad (1)$$

(Kullback and Leibler, 1951; Eguchi and Copas, 2006). This measure is zero when $P=\Pi$, but it does not have a fixed upper limit; it can be infinite when one or more π_j's are zero and the corresponding p_j's are not (Lin, 1991; Shlens, 2007), but, for a reasonable reference distribution with no unbalanced zeros, how large can it be? It is necessary to have a reference value in order to assess the significance of any result other than zero.

In what follows, we will present a method for evaluating the confidence that can be had about two distributions being similar, based on a K-L measure, using a seismological example.

In assessing seismic hazard for a given region a common tool is to look for clustering or gaps in the times of occurrence of earthquakes above a given magnitude in the background seismicity, because those features may be precursors to a large earthquake. If the observed seismicity appears to show clusters or gaps, to assess their significance it is necessary to test whether they may be due to random concentrations in events occurring with uniform probability over time, i.e. to test the observations versus the null hypothesis.

One way to test the null hypothesis is to use the well known fact that if events are occurring randomly with uniform probability in time at a rate of λ events per unit time,

Received: February 18, 2023; Accepted: April 10, 2023; Published on-line: July 1, 2023.

Editorial responsibility: Dra. Ana Teresa Mendoza Rosas

* Corresponding author: F. A. Nava
[1] Centro de Investigación y de Educación Superior de Ensenada, B.C., Departamento de Sismología.

Fidencio Alejandro Nava Pichardo

https://doi.org/10.22201/igeof.2954436xe.2023.62.3.1578

then the number of events n occurring within intervals of a given length T are distributed according to the Poisson distribution:

$$\Pr(n,T) = e^{-\lambda T}\frac{(\lambda T)^n}{n!} \tag{2}$$

(e.g. Mack, 1967; Dekking *et al.*, 2005; Boxma and Yechiali, 2007), so we will compare the distribution of observed n's with the Poisson distribution using the K-L divergence.

Significance of the K-L measure

Suppose that the times of occurrence of N_e=160 earthquakes ocurred over a period N_y=60 years have been observed, as shown in Figure 1 (top), which gives an occurrence rate λ=2.$\overline{66666}$ events/year, and , for the sake of simplicity, let us consider yearly intervals so T=1.0 yr in (2). Figure 1 (middle) shows the number of events per year, n, for each observed year, and (bottom) the corresponding histogram, as well as the expected number of events from the Poisson distribution.

The two distributions are not equal but, quantitatively, how different are they? We will measure their divergence using K-L. Observed probabilities are estimated from the histogram as

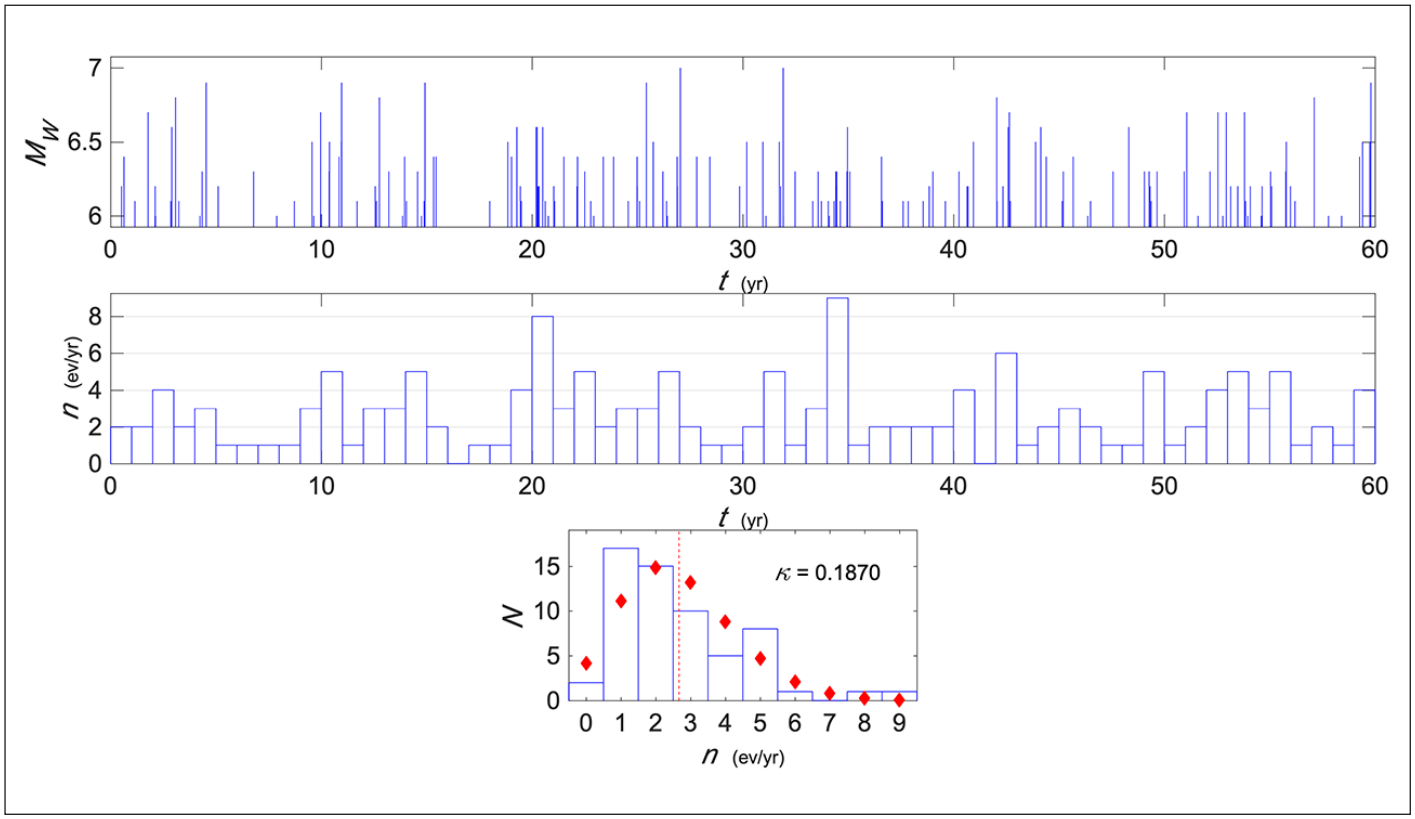

Figure 1. Times of occurrence 160 earthquakes with Gutenberg-Richter distributed magnitudes over a period of 60 years (top), number of earthquakes per year for each year (middle), and (bottom) histogram of numbers of earthquakes per year (blue line) and expected frequencies of earthquakes per year from the Poisson distribution.

$$p_n = \frac{N_n}{\sum_{k=0}^{n_{\max}} N_k}; n = 0,1,...,n_{\max}, \quad (3)$$

where N_n is the observed number of incidences of n events/year and n_{max} is the maximum observed n. We will compare this observed probability distribution with the reference

$$\pi_n = e^{-\lambda} \frac{\lambda^n}{n!}; n = 0,1,...,\infty, \quad (4)$$

as shown in Figure 2.

To evaluate the K-L divergence between these two distributions, although the Poisson distribution is non-zero for an infinite number of terms, the summation in (1) is only done from 0 to n_{max}, because P can be considered equal to zero for $n>n_{max}$ and terms with $p_n=0$ do not contribute to the summation.

The K-L evaluation yields $\kappa=0.1870$, but, what does this number mean (apart from the distributions not being equal)? Here, it must be considered that, as is common for seismological studies, particularly those involving large magnitudes, the observed distribution comes from only one very short realization consisting of only $N_y=60$ events.

Let us estimate how probable is the observed κ for samples of size N_y of a Poisson process. We will do this through a Monte Carlo simulation (Yakowitz, 1977; Rubinstein and Kroese, 2016) of $N_r=100{,}000$ realizations of synthetic samples of N_y Poisson distributed numbers n; the divergence κ between the resulting distribution P and Π from (3) is evaluated for each realization.

The probability distribution $f(\kappa)$ resulting from the simulation is shown in Figure 3 (top), the distribution has mean $\mu_\kappa=0.1066$ and standard deviation $\sigma_\kappa=0.0499$, and it is clear that the probability that a 60 samples long random realization of a Poissonian process actually results in $\kappa=0$ is extremely small. Indeed, if the sampled process were indeed Poissonian, instead of $\kappa=0$, a value around $\kappa=0.082$ would be much more probable.

The cumulative $F(\kappa)$ in Figure 3 (bottom) shows the observed $\kappa=0.1870$, and gives $\Pr(\kappa\geq0.1870)=0.0664$, so the possibility of the null hypothesis, that the observed seismicity occurred with uniform probability in time, can be rejected with 0.9336 confidence. This number constitutes a firm basis for the decision of whether to reject the null hypothesis or not; in this case the observed seismicity is, with high probability, not distributed uniformly in time, although the null hypothesis cannot be rejected at the widely used significance level of 0.05. It should be pointed out that this confidence estimation takes into account the sample length.

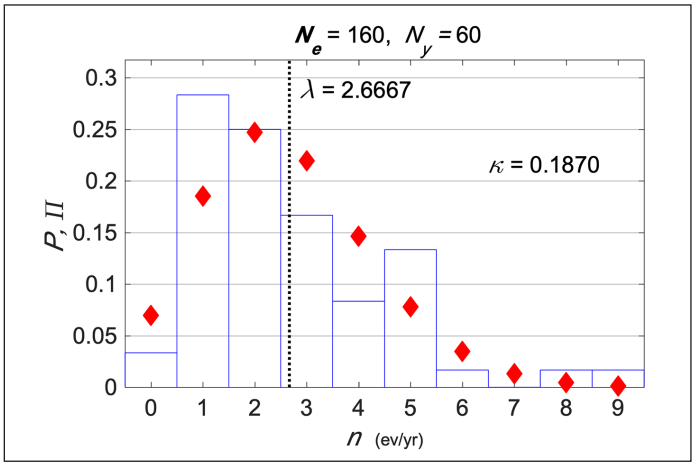

Figure 2. Observed distribution of n and corresponding values from the Poisson distribution (red diamonds) for $\lambda=2.\overline{66666}$ events/year indicated by the vertical dashed line. The K-L divergence between the two distributions is $\kappa=0.1870$.

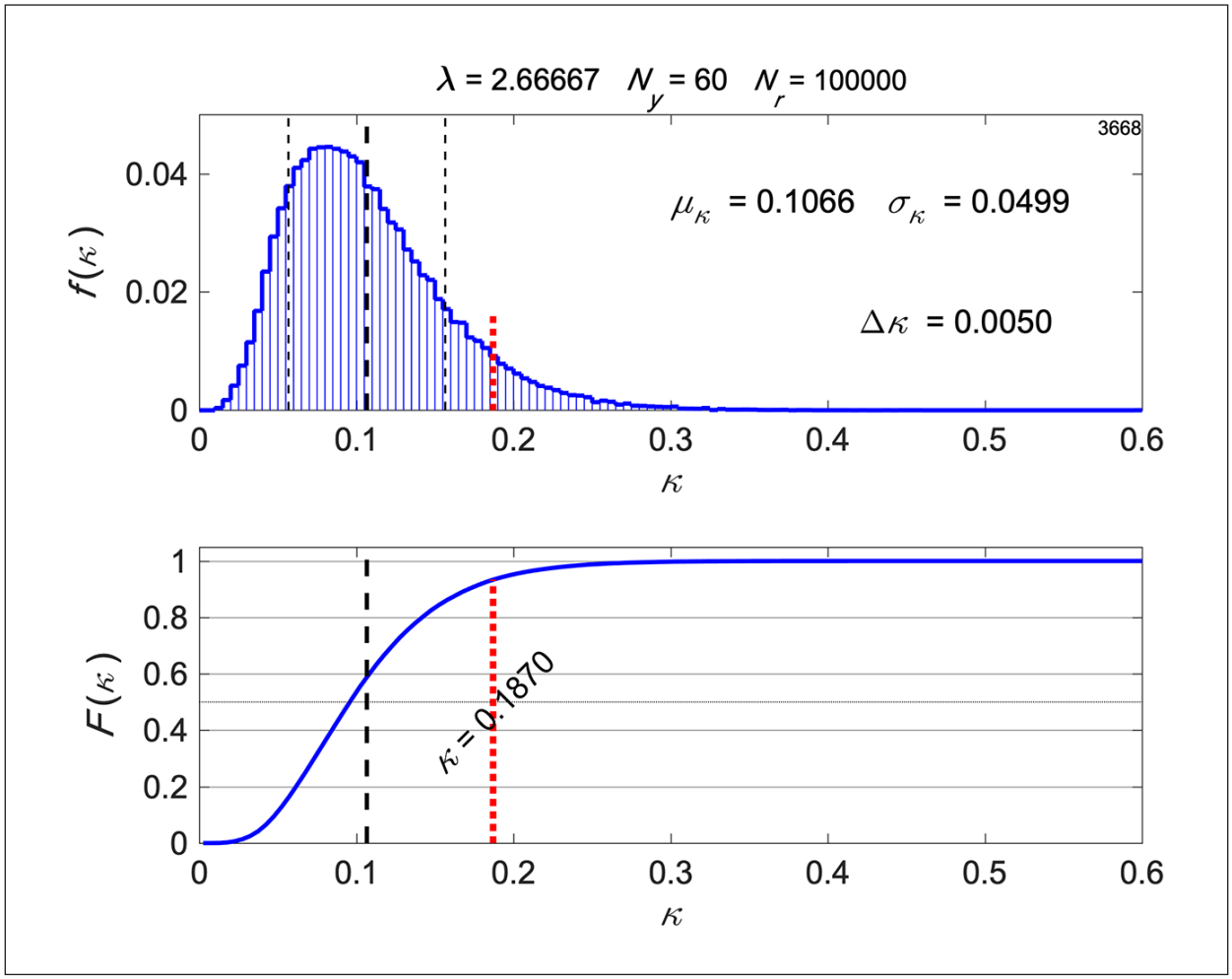

Figure 3. Distribution of κ values from the Monte Carlo simulation (top), $\Delta\kappa$ is the class width, the dashed thick vertical line indicates the mean μ_κ of the N_r=100,000 realizations, and the thin dashed vertical lines indicate plus/minus one standard deviation σ_κ from the mean. Cumulative κ distribution (bottom), the dashed black line is μ_κ, and the dotted red line indicates the observed κ=0.1870.

Other reference measures

We have presented a practical way for assessing the significance of a K-L measurement. Now, just for argument's sake, let us consider two other reference measures.

First, consider the uniform distribution, which is a common reference because it has the highest entropy (Shannon, 1948), with probabilities

$$p_n^U = \frac{1}{n_{\max}+1}; n = 0,1,...,n_{\max}, \quad (5)$$

shown as circles in Figure 4 (left). The K-L divergence between the uniform and Poisson distributions for n_{max}=9 is κ^U=1.22055, much higher than the value for our example distribution and has a probability value of nearly zero.

The second reference distribution is the "opposite" distribution to Poisson:

$$p_n^0 = \frac{\pi_{\max} - \pi_n}{\Sigma_{k=0}^{n_{\max}} \left(\pi_{\max} - \pi_\kappa\right)}; n = 0,1,...,n_{\max}, \quad (6)$$

where π_{max} is the maximum value of the Poisson distribution. It is an inverted and normalized Poisson as shown by circles in figure 4 (right). The K-L divergence for the opposite distribution is κ^O=2.82680, and it is considerably higher than the observed κ and the reference κ^U; its divergence is not the highest possible between the Poisson distribution and another distribution of the same length, but it is the most different distribution in an intuitive way.

Of course, both reference values should be estimated for the same n range as that of the observed distribution (they increase with the length of the range), and may not be very useful because they have very large κ values with vanishingly small probabilities, but still they are better reference values than infinity.

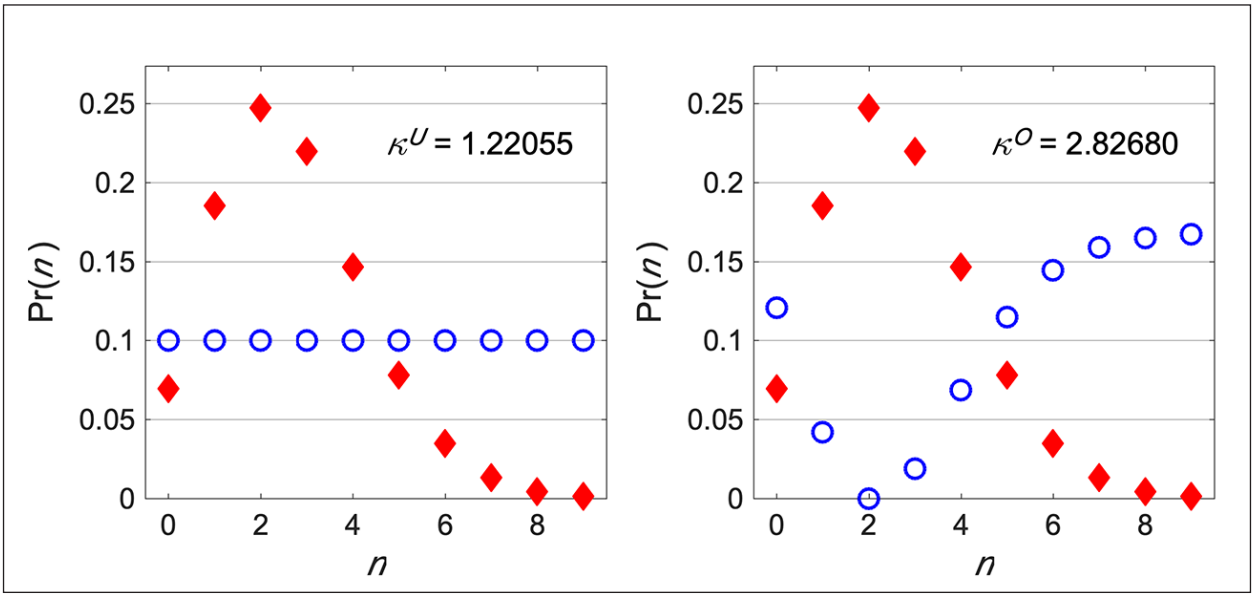

Figure 4. Poisson distribution for $\lambda=2.\overline{66666}$ events/year, and $n_{max}=9$, indicated by red diamonds, and the uniform (left) and opposite (right) reference distributions.

Discussion

We presented a method of estimating significance levels associated with measures of the K-L divergence, and proposed two possible reference values. The Poisson distribution was used as an example, but the method is applicable to any other reference distribution.

The Monte Carlo evaluation of the significance of a κ value illustrates quite clearly the problem of having to work with small samples, which is unfortunately the case with many studies in statistical seismology, due to the relative shortness and heterogeneity of the seismic catalogs, particularly for studies dealing with large earthquakes. One of the advantages of the proposed method is that it takes into account variations caused from samples that are but small realizations of a stochastic process. In the example presented here we showed that a N_y=60 long sample from a true Poissonian process has almost null probability of resulting in κ=0, because for that sample length the κ values are distributed with mean μ_κ=0.1066 and standard deviation σ_κ=0.0499, while samples of N_y=120 have μ_κ=0.0561 and σ_κ=0.0255, and for N_y=180 μ_κ=0.0384 and σ_κ=0.0171 (all for equal λ). Hence, κ values cannot be correctly interpreted without taking into account the sample length, something that our proposed method does implicitly.

The method proposed here can be a useful tool in studies of seismic hazard, where it is essential to distinguish, with a quantitative bas is, between an apparently anomalous distribution being observed and the null hypothesis.

Acknowledgments

Many thanks to two anonimous reviewers and to the editorial staff of *Geofísica Internacional*: Ana Teresa Mendoza Rosas, Servando de la Cruz, and Andrea Rostan.

References

Boxma, O. J., & Yechiali, U. (2007). Poisson processes, ordinary and compound. *Encyclopedia of statistics in quality and reliability.*

Dekking, F. M., Kraaikamp, C., Lopuhaä, H. P., & Meester, L. E. (2005). *A Modern Introduction to Probability and Statistics: Understanding why and how* (Vol. 488). London: Springer.

Eguchi, S., & Copas, J. (2006). Interpreting kullback–leibler divergence with the neyman–pearson lemma. *Journal of Multivariate Analysis*, 97(9), 2034-2040.

Lin, J. (1991). Divergence measures based on the Shannon entropy. *IEEE Transactions on Information theory*, 37(1), 145-151.

Kullback, S., & Leibler, R. A. (1951). On information and sufficiency. *The annals of mathematical statistics*, 22(1), 79-86.

Mack, C. (1967). *Essentials of statistics for scientists and technologists.* Plenum Press, New York, 173pp.

Rubinstein, R. Y., & Kroese, D. P. (2016). *Simulation and the Monte Carlo method.* John Wiley & Sons

Shannon, C. E. (1948). A mathematical theory of communication. *The Bell system technical journal*, 27(3), 379-423.

Shlens, J. (2007). Notes on kullback-leibler divergence and likelihood theory. *Systems Neurobiology Laboratory*, 92037, 1-4.

Yakowitz, S. (1977). *Computational probability and simulation.* Addison-Wesley Pub. Co.

Geofísica Internacional (2023) **62-3**: 525 - 542

Parámetros del terremoto del 05 febrero de 1938 en la Región del Eje Cafetero-Colombia a partir de datos macrosísmicos

Elkin de Jesús Salcedo-Hurtado[1,4], Mario Hernández Obregón[2,4], Nathalie García Millán[3,4]*

Resumen

El 05 de febrero de 1938 en la región del eje cafetero se produjo un terremoto histórico en Colombia. Se aplican métodos de análisis macrosísmico a partir de curvas de isosistas, para determinar los principales parámetros sismológicos del terremoto ocurrido. Los resultados indican que el epicentro macrosísmico normal (E_n) está localizado en $\phi = 5.102°$ N; $\lambda = 75.603°$ O. Se identificó que la profundidad del foco normal es $h_n = 62.9 \pm 1.44$ km. La magnitud y energía sísmica liberada se calcularon aplicando ecuaciones existentes en la literatura, obteniéndose M6.2 y M_L6.2. La energía sísmica liberada es $E = 1.37*10^{23}$ ergios. Se evaluó el momento sísmico escalar $M_0 = 2.74*10^{27}$ dinas-cm y la respectiva magnitud momento sísmico $Mw = 7.6$. Por último, se calculó la magnitud de ondas superficiales $Ms = 6.7$ y la aceleración sísmica es de 0.15g.

Palabras clave: Terremoto, campo macrosísmico, Epicentro macrosísmico, Profundidad focal, Magnitud, Momento sísmico.

Abstract

A historical earthquake ocurred in Colombia on February 5, 1938 in the Eje Cafetero zone. Macrosismic analysis methods are applied from isoseismal curves, to determine the main seismological parameters of this earthquake. The results indicate that the normal macrosismic epicenter (E_n) is located at $\phi = 5.102°$ N; $\lambda = 75.603°$ W. The normal depth of focus $h_n = 62.9 \pm 1.44$ km was identified. The magnitude and seismic energy released were calculated by applying existing equations in the literature, obtaining M6.2 and M_L6.2. The seismic energy released is $E = 1.37*10^{23}$ erg. The scalar seismic moment $M_0 = 2.74*10^{27}$ dynes-cm and the respective seismic moment magnitude $Mw = 7.6$ were evaluated. Finally, the magnitude of surface waves $Ms = 6.7$ was calculated and 0.15 g in the seismic acceleration.

Key words: Earthquake, Macrosismic field, Macroseismic epicenter, Focal depth, Magnitude, Seismic moment.

Introducción

El terremoto del 5 de febrero de 1938 es considerado como uno de los eventos sísmicos más importantes que han ocurrido en Colombia, afectando varias poblaciones del Eje Cafetero, que corresponde a la región cultural, económica y ecológica ubicada en la parte centro-occidental del país, abarcando territorios de los departamentos de Caldas, Risaralda, Quindío, Tolima, suroeste del departamento de Antioquia, y el norte y oriente del departamento del Valle del Cauca.

Debido a la energía liberada por el evento, las ondas sísmicas fueron registradas en varias estaciones sismográficas del mundo como en St. Louis (EE. UU.), San Juan de Puerto Rico, Huancayo (Perú), Ottawa (Canadá), Tortosa (España), Manila (Islas Filipinas), entre otras (Ramírez, 1938). Se tienen diversos registros históricos que dan cuenta de los efectos y daños causados por este sismo; según Ramírez (1975), por las consecuencias ocasionadas, este evento se recuerda de manera especial en casi todas las poblaciones de la región.

El departamento de Caldas concentró las mayores afectaciones, sufriendo daños generalizados en casi todo su territorio. En sus municipios se registraron colapso de viviendas y edificaciones, daños graves en iglesias, caída de postes de alumbrado público, afectaciones en las redes de acueducto y algunos muertos (Ramírez,1975; Espinosa, 2012). En el Quindío, los daños fueron menores que en Caldas, se presentaron averías en edificios de bancos, teatros, colegios y viviendas; sin embargo, en el municipio de Salento, hubo

Received: October 15 , 2019; Accepted: June 7, 2023; Published on-line: July 1, 2023.

Editorial responsibility: Dr. Raúl W. Valenzuela

* Corresponding author: Nathalie García Millán
[1] Universidad del Valle, Departamento de Geografía, Ciudad universitaria. Calle 100 No. 13-00. Cali, Colombia. elkin.salcedo@correounivalle.edu.co
[2] Estudiante Maestría en Análisis Espacial y Geoinformática, Universidad Autónoma del Estado de México. Toluca, México.
[3] Estudiante Doctorado Ciencias Ambientales, Universidad del Valle-Cali, Calle 100 No. 13-00. nathalie.garcia@correounivalle.edu.co
[4] Grupo Georiesgos, adjunto al Observatorio Sismológico y Geofísico del Suroccidente Colombiano (OSSO - REDSW), Universidad del Valle, Ciudad Universitaria. Santiago de Cali, Colombia.

Elkin de Jesús Salcedo Hurtado

https://doi.org/10.22201/igeof.2954436xe.2023.62.3.1715

destrucción parcial del casco urbano, donde la mayoría de las residencias fueron destruidas y edificios públicos resultaron gravemente averiados. En el departamento de Risaralda, hubo daños en fábricas, varios edificios destruidos, afectaciones graves en edificaciones, iglesias, plazas de mercado y establecimientos comerciales. Finalmente, en el Valle del Cauca, se presentaron averías serias sobre todo en las edificaciones y viviendas de los municipios del norte del departamento (Espinosa, 2012).

Sobre este evento sísmico se han propuesto diversas soluciones de sus parámetros sismológicos, en especial su localización epicentral, profundidad, magnitud e intensidad (Gutenberg & Richter, 1954; Goberna *et al.*, 1985; Espinosa, 1996; Ramírez, 1975; Engdahl & Villaseñor, 2002; Marín *et al.*, 2006; Cifuentes & Sarabia, 2007; SGC, 2015; Di Giacomo & Sarabia, 2021). Algunas de estas fuentes lo que hacen es reproducir los datos presentados por otros estudios anteriores sin realizar cálculos específicos de sus parámetros.

Dado que, a la fecha de ocurrencia del sismo, el país no contaba con instrumentación, ni red de estaciones, para la detección y obtención de variables físicas, la utilización de datos macrosísmicos se convierte en la mejor y única opción para obtener relaciones y fórmulas que permitan una mayor comprensión del evento y de la amenaza sísmica de la región (Gómez Capera & Salcedo Hurtado, 2002). Por lo tanto, el presente artículo, partiendo del mapa de intensidades propuesto por Espinosa (1996) y haciendo uso de modelos ampliamente difundidos en la literatura, contribuye en la ampliación del conocimiento del evento sísmico del 5 de febrero de 1938 con la determinación de los parámetros macrosísmicos del terremoto (profundidad focal, localización epicentral y magnitud); de igual manera, se evalúa la magnitud Mw, la energía y la aceleración sísmica. Los resultados obtenidos en este trabajo son comparados con los presentados por otros autores en estudios anteriores, mostrándose un gran complemento de parámetros que pueden ser útiles en estudios de amenaza y riesgo sísmico regional.

Marco tectónico regional

Desde el contexto geodinámico el territorio colombiano es una región compleja dominada por las placas tectónicas Sudamericana, Nazca y Caribe. Los movimientos relativos entre estas placas durante la era Cenozoica dieron origen al sistema orogénico de los Andes del Norte, y ha generado deformaciones continentales, actividad volcánica y una intensa dinámica sísmica (Taobada *et al.*, 1998; Cortés & Angelier, 2005).

Específicamente, el occidente colombiano se encuentra enmarcado por la convergencia de la placa Nazca bajo la placa Sudamericana, siendo la principal fuente de amenaza sísmica para Colombia y la causante de los dos terremotos más grandes que afectaron el país durante el siglo XX, en los años 1906 y 1979, con una magnitud 8.8*Mw* y 8.1Mw, respectivamente (INGEOMINAS & DAGMA, 2005).

La interacción de estas placas se da a lo largo de la trinchera Colombo-Ecuatoriana con una velocidad de subducción de aproximadamente 7.0 cm/año (Freymueller *et al.*, 1993; Taobada *et al.*, 1998; Taobada *et al.*, 2000). Sin embargo, la geometría de la placa Nazca bajo la Suramericana ha sido estudiada y debatida por diversos autores (Santó, 1969; Isack & Molnar, 1971; Dewey, 1972; Baranzagi & Isacks, 1976; Pennington, 1981; Hall & Wood, 1985; Gutscher *et al.*, 1999; Gutscher *et al.*, 2000; Quispe *et al.*, 2003; Monsalve & Mora, 2005; INGEOMINAS & DAGMA, 2005), quienes de manera general plantean que es caracterizada por presentar diferentes modos y ángulos de subducción, que se ven reflejados en la distribución de la sismicidad, sobretodo en aquella de profundidad intermedia (entre los 3°N y 4°N de latitud) y han conllevando al reconocimiento de una segmentación longitudinal de la placa (INGEOMINAS & DAGMA, 2005; Pedraza-García *et al.*, 2007).

Bohorquez *et al.* (2005), señalan que la subducción de la placa Nazca presenta cambios en el buzamiento a lo largo de la zona de colisión, teniendo al norte un ángulo de 18°, en un segmento denominado Murindó, luego un ángulo de 30°, en un segmento de transición (entre los 5°N y 6°N), y al sur 38°, en el segmento denominado Cauca. A su vez, Pedraza-García *et al.* (2007), plantean que dentro de la trinchera Colombo-Ecuatoriana se presentan tres tipos de subducciones, que varían para diferentes segmentos en su ángulo de inmersión, profundidad y distancia. Estos autores proponen la presencia de cuatro segmentos: Cali, Popayán, Nariño y Quito.

Por otro lado, en la caracterización sismotectónica del estudio de microzonificación sísmica de la ciudad de Cali (INGEOMINAS & DAGMA, 2005), se define para la zona de subducción tres segmentos (Figura 1). El segmento Norte se localiza entre 5.5ºN y 7.5ºN de latitud, frente a la costa norte del departamento del Chocó, con un azimut de 310° y 170 km de longitud. Se caracteriza por presentar las mayores profundidades para la fosa Colombo-Ecuatoriana y por la sismicidad más cercana a la fosa inferior a los 60 km de profundidad, con aumento en la profundidad hacia el noreste y concentrada hacia los extremos del segmento.

El segmento Centro está localizado frente a la costa sur de Chocó, entre 4.0°N y 5.5°N de latitud, con 20° de azimut en un tramo de 160 km. La sismicidad superficial se concentra en la parte norte del segmento, aumentando la profundidad hacia el oriente bajo las cordilleras Occidental y Central, con sismos de hasta 210 km de profundidad. Según este estudio de microzonificación sísmica (INGEOMINAS & DAGMA, 2005), el plano de Benioff tiene 40º de buzamiento, que se introduce hasta los 210 km de profundidad bajo la cordillera Central, donde se localiza el vulcanismo activo en esta zona del país.

Por último, el segmento Sur se encuentra frente a las costas de los departamentos de Valle del Cauca, Cauca, Nariño y norte de Ecuador, entre 0° y 4°N de latitud y 40° de azimut, con una longitud cercana a los 550 km. La actividad sísmica en este tramo muestra dos comportamientos, el primero de tipo superficial (< 30 km), próxima a la fosa y la segunda, con sismos algo más profundos (40 km) hacia el continente (INGEOMINAS & DAGMA, 2005).

Sismos representativos en la zona de estudio

La región del Eje Cafetero, históricamente ha sido sometida a eventos sísmicos que han dejado fuertes afectaciones en su

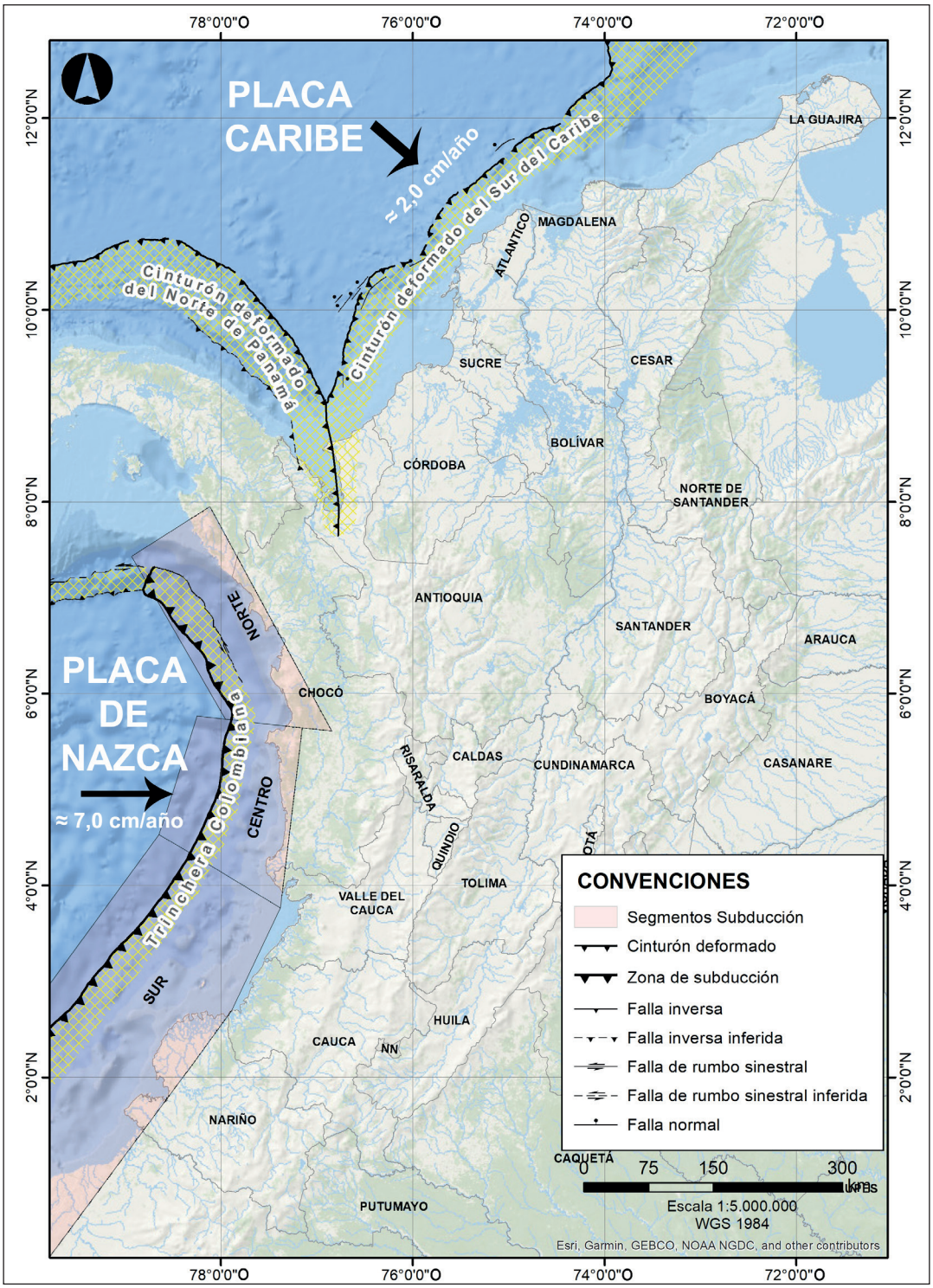

Figura 1. Marco tectónico regional: a) convergencia de placas tectónicas en la esquina noroccidental de Sudamérica, (Fuente: modificado de París *et al.*, 2000; INGEOMINAS & DAGMA, 2005).

territorio. Se tiene conocimiento que el evento más antiguo registrado, que haya ocasionado algún tipo de consecuencia, es del año 1785 y el más reciente de 1999 (Espinosa, 2012). Según lo descrito por Ramírez (1975) y Espinosa (2012), por sus implicaciones en la región, es conveniente citar los eventos sísmicos del 5 de febrero de 1938 (objeto de análisis en el presente estudio), 20 de febrero de 1961, 30 de julio de 1962, 23 de noviembre de 1979, 8 de febrero de 1995 y el del 25 de enero de 1999; los cuales lograron intensidades por encima de VII.

De estos, sobresalen el sismo del 23 de noviembre de 1979, que dejó enormes pérdidas en toda la región, sobretodo en Manizales (Caldas) y Pereira (Risaralda), y el ocurrido el 25 de enero de 1999, que se destaca por los graves daños ocasionados, sobretodo en la ciudad de Armenia (Quindío), donde más de 50 edificaciones colapsaron y centenares quedaron muy afectadas (Espinosa, 2012).

Por otro lado, al analizar el catálogo sísmico de la Red Sismológica Nacional de Colombia (RSNC), se obtiene que desde el año 1993 hasta diciembre de 2018, en la región se han presentado 8122 eventos sísmicos (Figura 2a), que en su mayoría son superficiales (Figura 2b y 2c) y presentan valores de magnitud entre 1.8 y 6.5 Ml. Para este set de datos, el valor global del parámetro *b* obtenido a partir de la relación Gutenberg–Richter, corresponde a un rango bajo (Figura 2d), que puede interpretarse como una alta concentración de esfuerzos (energía elástica), asociados posiblemente a procesos de deformación tectónica (Wiemer & Wyss, 1997; Zuniga & Wiss, 2001) y a la probabilidad de presentarse sismos de una magnitud grande en la región (Condori & Pérez, 2015). Sin embargo, dado que no es el objeto de la presente investigación, no se realiza un análisis de las variaciones espaciales de este parámetro y no se contemplan procesamientos estadísticos específicos para mejorar el ajuste de los datos en las magnitudes superiores a 5 Ml, donde se carece de registros.

2. Estudios anteriores

Alrededor de las 02:23 UTC del 05 de febrero de 1938 fuentes primarias escritas reportan la ocurrencia de un terremoto

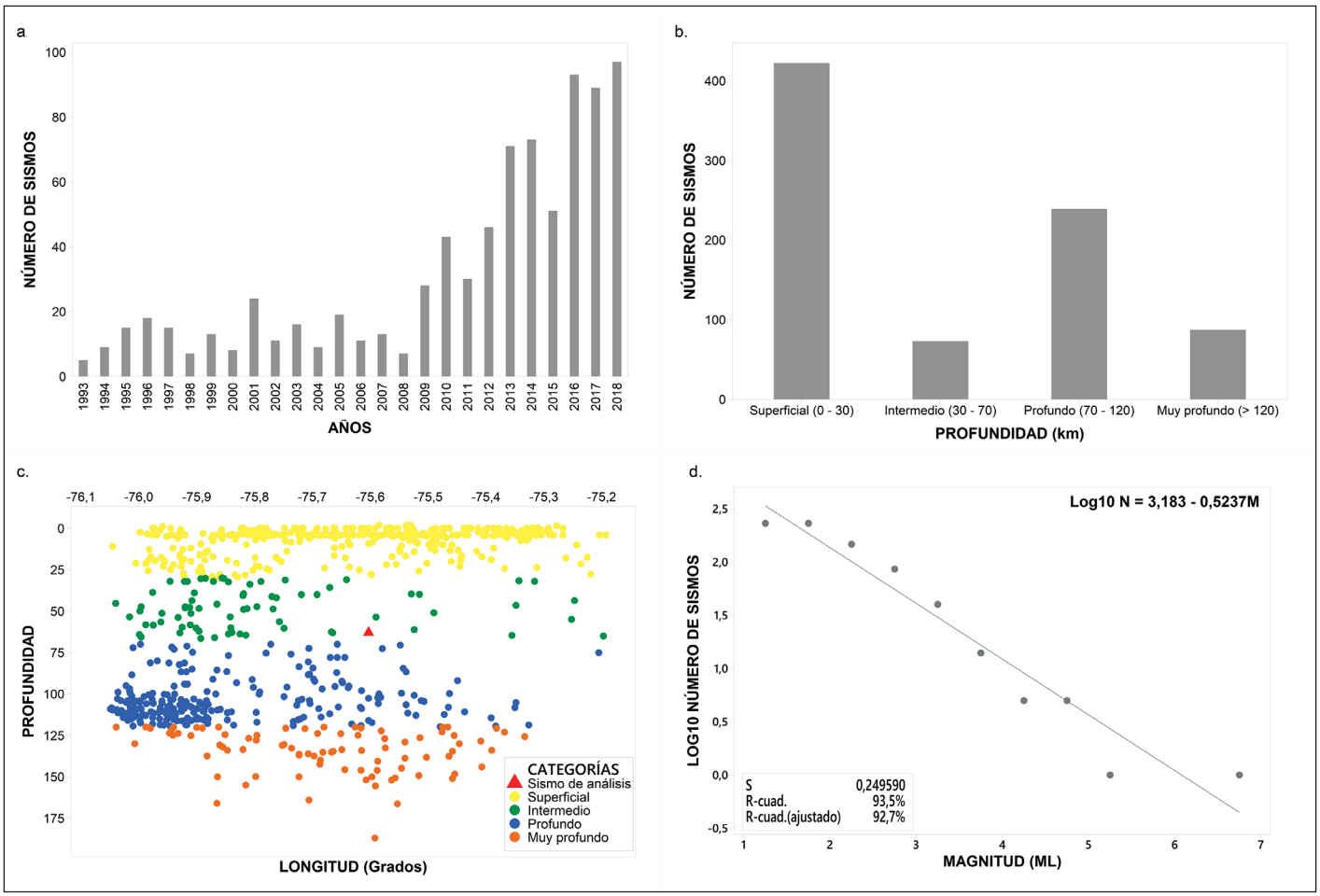

Figura 2. Características de la sismicidad en la zona de estudio: a) distribución temporal de la sismicidad en el periodo de 1993 a 2018, b) número de sismos por profundidad, c) distribución de la sismicidad con la profundidad y d) relación G-R, frecuencia de ocurrencia de los sismos (Fuente: gráficas realizadas con información del catálogo sísmico de la Red Sismológica Nacional de Colombia (RSNC).

que, debido a la violencia del choque de las ondas, causó que las plumas de los sismógrafos se salieran (Periódico La Voz de Caldas, 1938). La Figura 3 muestra los diferentes estudios que reportan datos macrosísmicos e instrumentales sobre este evento sísmico.

2.1 Datos Instrumentales

Gutenberg & Richter (1954), reportan la ocurrencia del terremoto a las 02:23:24 del 05 de febrero de 1938 en hora universal, es decir, 5 horas después del horario en Colombia, localizado en las coordenadas 4.500ºN y 76.250ºO, en cercanías al municipio El Dovio, Valle del Cauca, con profundidad de 160 km, y magnitud 7.0 *Ms*.

En el trabajo del Centro Regional de Sismología para América del Sur (Goberna *et al.*, 1985), el sismo se relocaliza en 4.500ºN y 76.300ºO, con la misma profundidad y hora de ocurrencia planteada por Gutenberg & Richter en 1954, además indican que la intensidad máxima en la Escala MM fue IX, con magnitud 7.0 *Ms*.

Engdahl & Villaseñor (2002, en USGS) por su parte plantean la ocurrencia del sismo a las 02:23:41 UTC, a 4.555ºN latitud y 75.919ºO longitud, en cercanías del municipio Obando, Valle del Cauca, con profundidad 155.7 km y magnitud 6.9mB.

2.2 Datos Macrosísmicos

Según el estudio desarrollado por Ramírez (1975), el epicentro del terremoto estuvo localizado en las coordenadas 5.100ºN y 75.500ºO en Manizales, Caldas, a 160 km de profundidad, con intensidad mayor que VIII (Escala Rossi-Forel), los mayores daños causados se reportan en las poblaciones de Támesis, Aguadas, El Jardín, Valparaíso,

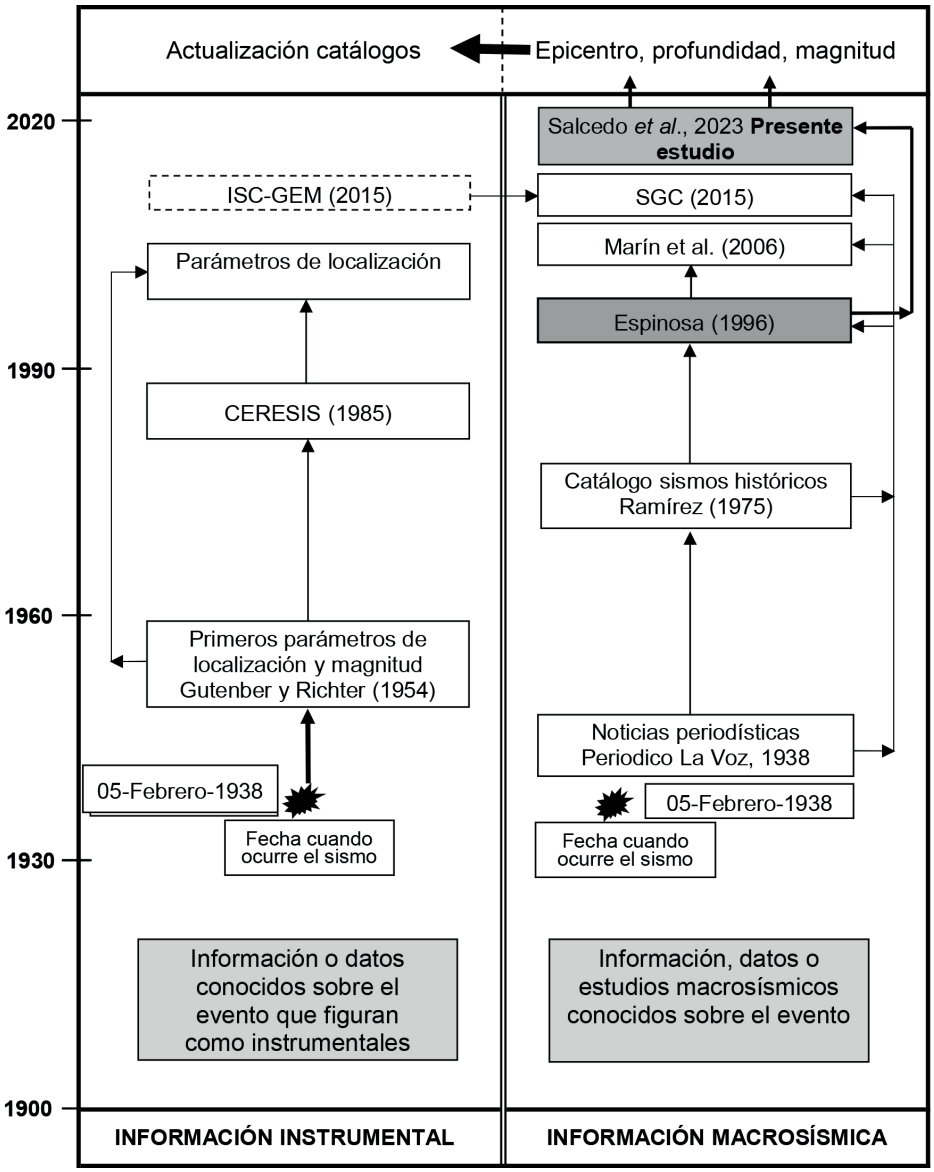

Figura 3. Árbol de estudios sobre el terremoto del 5 de febrero de 1938 en Colombia (Fuente: elaboración propia).

etc., en las vertientes orientales del Cauca. Sin embargo, el sismo se sintió casi en toda la nación, propagándose con mayor facilidad a lo largo de los ejes de las cordilleras.

Posteriormente, Espinosa (1996), propuso como epicentro macrosísmico al municipio de Filadelfia, Caldas. Las coordenadas correspondientes fueron 5.360ºN latitud y 75.63°O longitud, define una profundidad instrumental de 90 km y una macrosísmica mayor a 45 km, con una intensidad máxima regional de VII – IX en la escala MSK (Medvedev, Spohneuer & Karnik, 1965).

Marín *et al.*, (2006), a partir de diversas fuentes documentales, proponen que el epicentro del terremoto de 1938 estuvo localizado en Riosucio, Caldas, en coordenadas 5.355ºN y 75.625ºO, con profundidad de 90 km y magnitud 5.8*Ms*; registran intensidades en la Escala Macrosísmica Europea (EMS-98) de X en las poblaciones de Aguadas y Aranzazu, IX en Manizales, VII en Riosucio y Villamaría.

El Servicio Geológico Colombiano (SGC, 2015) y Di Giacomo & Sarabia (2021) recopilan distintos parámetros instrumentales del sismo, entre ellos la localización epicentral que está dada en las coordenadas 4,684ºN y 75,695ºO, cerca al municipio de Filandia, Quindío, y la profundidad (150 km) los cuales fueron tomados del International Seismological Centre. La magnitud 7.0*Ms* corresponde a la calculada por Gutenberg & Richter, además indican una magnitud 7.5Mw. Por otra parte, también recopilan información de fuentes primarias para dar cuenta de los efectos del sismo en distintos municipios del país, definiendo una intensidad máxima de VIII en la escala EMS-98.

La Tabla 1 resume los datos y parámetros reportados por las fuentes arriba reseñadas sobre el terremoto del 05 de febrero de 1938 ocurrido en la región del Eje Cafetero en el territorio de Colombia.

3. Campo macrosísmico

El campo macrosísmico de un terremoto, es decir, la sistematización de los efectos dejados por el evento en la superficie terrestre, se relaciona con las características del foco por medio de una relación que representa el decaimiento de la intensidad con el aumento de la distancia hipocentral (distancia al epicentro y profundidad), de la siguiente manera:

$$I_i = I_0 - f(r_i) \tag{1}$$

Donde I_i – intensidad de la i-ésima isosista, I_0 – intensidad epicentral, y r – distancia hipocentral expresada como:

$$r^2 = \sqrt{x_i^2 + h^2} \tag{2}$$

Con x definida como la distancia epicentral dada por el valor de la i-ésima isosista y h la profundidad focal del sismo.

La ecuación (1) muestra que la intensidad en un punto determinado depende de la profundidad focal del terremoto,

Tabla 1. Datos instrumentales y macrosísmicos del terremoto del 05 de febrero de 1938 en el Eje Cafetero (Colombia), reportados en estudios anteriores (Fuente: elaboración propia).

Fuente	Localización	Profundidad (km)	Magnitud	Intensidad
Gutenberg & Richter (1954)	4.500ºN 76.250ºO	160	7.0 *Ms*	---
Goberna et al., (1985)	4.500ºN 76.300ºO	160	7.0 *Ms*	IX (MM)
Espinosa (1996)	5.360ºN 75.630ºO	90 (Instrumental) > 45 (Macrosísmica)	---	VII Io (MSK) VIII – IX Máxima Regional
Ramírez (1975)	5.100ºN 75.500ºO	160	7.0	> VIII (Rossi-Forel);
Engdahl & Villaseñor (2002)	4.555ºN 75.919ºO	155.7	6.9 mB	---
Marín et al., (2006)	5.355ºN 75.625ºO	90	5.8 *Ms*	X (EMS-98)
SGC, 2015	4.684ºN 75.695ºO	150	7.0 *Ms* 7.5 Mw	VIII (EMS-98)
Di Giacomo & Sarabia (2021)	4.684ºN 75.695ºO	150	---	VIII (EMS-98)

lo que hace que su determinación sea un parámetro fundamental en todo análisis macrosísmico. Así, con este objetivo, en el presente trabajo se usa el modelo teórico propuesto por Blake (1941), modificado por Shebalín (1968), por lo cual se denomina como modelo Blake-Shebalín.

3.1 Caracterización del Campo Macrosísmico

El efecto macrosísmico dejado por un terremoto no se crea por el movimiento en toda la falla que lo produce sino en un segmento de ella, lo que demuestra porqué en las zonas inmediatas a ésta la intensidad es comparativamente elevada. Así, se establece que la formación de la parte de corto período de todo el espectro de radiación de un terremoto, es la responsable del desarrollo no solo del foco en total, sino de un conjunto de subfocos que, con ciertas propiedades y características definidas, se desarrolla dentro de las dimensiones del foco (Shebalin, 1972). Se tiene que en un foco grande existen dos tipos fundamentales de subfocos de emisión de corto período que, por un lado, corresponden a múltiples y pequeñas grietas, y, por el otro, a las complejidades tectónicas locales generadas por el movimiento en la falla principal.

Según Shebalin (1972), la combinación de los efectos del campo lejano y cercano en la aparición de un nivel de intensidad, en un punto específico de la superficie de la tierra, Pi, la geometría del campo macrosísmico se modifica por un incremento en el valor de intensidad producido por los efectos locales del terreno. Por lo cual, el foco del terremoto se entiende como la mínima región suficientemente isométrica, dentro de la cual se encierran todas las deformaciones irreversibles iniciales generadas por la liberación de la energía acumulada en un volumen en el interior de la Tierra. En otras palabras, el foco del terremoto puede considerarse puntual sólo si éste se ubica en una distancia suficientemente lejana del punto de observación (cuando la distancia hipocentral de todas las subfuentes de los semifocos, quedan al lado del observador y satisfacen la condición $Dmin < D < kDmin$). Para los sismos más cercanos al punto de observación, se ponen de manifiesto los efectos locales del campo macrosísmico.

3.2 Efectos de extensión del foco del terremoto

El modelo cinemático más sencillo de la fuente de un terremoto, es considerarlo como un foco puntual, es decir, que se reduce a un punto sin dimensiones; sin embargo, esto es válido sólo si las observaciones se hacen a grandes distancias y son de frecuencias muy bajas comparadas con las dimensiones de la fuente. De esta forma, el foco de un terremoto puede considerarse como un punto para todas las distancias epicentrales definidas como (Shebalín, 1972):

$$D = \sqrt{\Delta^2 + h^2} \tag{3}$$

También han sido considerados modelos de focos con dimensión, en los cuales la dislocación producida se extiende a lo largo de una cierta superficie S. En este caso, es necesario especificar la geometría de la superficie de la fractura. Los dos modelos más sencillos y comunes son el de una fractura rectangular, propuesto por Haskell (1964), y el de fractura circular, presentado por Brune (1970). En el primer caso, la fractura se propaga unilateralmente en una dirección a lo largo de la longitud de la falla, que también tiene un ancho específico. En el caso de la fractura circular, la dislocación es representada por un pulso de esfuerzos tangenciales aplicado instantáneamente sobre toda la superficie de la falla. Este puede ser considerado como un modelo intermedio entre los modelos cinemáticos y los dinámicos.

Sin embargo, Savage (1966) propuso un modelo un poco más complejo, en el cual se considera que la fractura contiene un efecto de comienzo o nucleación y la correspondiente parada o finalización. Este modelo se representa en una fractura elíptica en la que su nucleación se origina en uno de los focos, que al prolongarse se detiene cuando llega al borde de la elipse. Es necesario mencionar, que el punto de origen de la fractura es el que se determina instrumentalmente como foco del terremoto, cuya profundidad es la que se ha denominado como profundidad normal Shebalin (1968, 1971).

De acuerdo con el modelo de comienzo y finalización de la ruptura focal propuesto por Savage (1966) y teniendo en cuenta las propiedades del medio geofísico, considerado como discreto y jerárquico donde se supone que las fracturas no son lineales sino que se propagan por las zonas de contacto entre bloques, podemos suponer que el foco de un terremoto, para alcanzar o acercarse a la superficie terrestre encierra necesariamente un área elíptica que en su propagación experimenta una extensión tanto horizontal como vertical. De manera que, el foco se presentará como la sucesión de subfocos que se han propagado casi oblicuamente.

Para esto, es necesario suponer, siguiendo el principio de Huygens que, al interior de toda la fractura, entre los focos de iniciación y terminación, existe una sucesión finita de subfocos (cadenas y barreras), a través de los cuales progresivamente se va transmitiendo la radiación de la energía elástica. Es posible considerar que estos subfocos son producidos por la oscilación de corto periodo de todo el espectro de radiación (Shebalin, 1972).

En términos generales, la solución del problema de determinar las dimensiones y ubicación del foco principal, usando la información de los mapas de isosistas, corresponde a resolver el problema inverso de la macrosísmica, que básicamente consiste en definir las relaciones fundamentales entre la profundidad del foco del terremoto h y las dos dimensiones lineales del foco, es decir, sus extensiones horizontal l_x y vertical l_z. En este caso, como profundidad

del foco se entiende el centroide de irradiación de la energía macrosísmica y no la profundidad del hipocentro, punto donde se inicia la ruptura.

3.2.1 Extensión horizontal del foco

De acuerdo con Shebalin (1972), se puede considerar que existe una relación directa entre la magnitud y las dimensiones de la ruptura en un terremoto, por lo que el foco de gran extensión horizontal l_x, puede representarse por una cadena de subfocos. De manera aproximada, la extensión horizontal podría definirse de acuerdo a la relación Shebalin (1991). Así, es justo suponer que la forma de la primera isosista hereda la extensión horizontal del foco local; en este caso la absorción anisotrópica en las pequeñas distancias puede despreciarse. Shebalin (1972) propuso que en términos generales la extensión horizontal del foco puede calcularse a partir de la siguiente fórmula:

$$l_x = d_{1\max} - d_{1\min} \tag{4}$$

En un terremoto grande, dependiendo de las condiciones del terreno, puede suceder que la aparición de la primera isosista, la de mayor valor de intensidad, esté relacionada con el efecto local de la extensión vertical del foco. En estos casos toda la extensión horizontal del foco se manifiesta en la forma de la siguiente isosista, libre del efecto local de la misma; de tal manera que l_x está representado por el promedio de las dos primeras isosistas:

$$l_x = \frac{\left(d_{1\max} - d_{1\min}\right) + \left(d_{2\max} - d_{2\min}\right)}{2} \tag{5}$$

La extensión horizontal del foco representa uno de los factores que definen la falta de coincidencia de los epicentros instrumental y macrosísmico. Los otros dos factores son el error de la definición instrumental y las grandes heterogeneidades del medio de la región del foco. Para terremotos donde es evidente la aparición de una gran extensión horizontal del foco, el epicentro macrosísmico se toma como el centro de la primera isosista.

3.2.2 Extensión vertical del foco

De acuerdo con Shebalin (1972), la extensión vertical (l_z) del foco puede calcularse a partir de la siguiente expresión:

$$\log l_z = 0{,}3M - 0{,}8 \tag{6}$$

En el caso del foco con gran extensión vertical, se establecen los criterios de existencia del efecto macrosísmico de extensión vertical con:

$$0{,}3\mathrm{M} - 0{,}7 \geq \log h_n \geq 0{,}3M - 0{,}95 \tag{7}$$

donde h_n (km) es la profundidad "normal" del foco. El primer límite significa la aparición de la ruptura en la superficie. El límite derecho marca la desaparición del efecto no puntual.

Además del criterio representado por la ecuación (7) los efectos macrosísmicos de la extensión vertical pueden ser revelados por la relación de las áreas de las isosistas vecinas. De manera que si la curva $f(i) = S_1 / S_{(i+1)}$ tiene un mínimo o un máximo en la segunda - tercera isosista, entonces, esto significa la existencia del efecto local, condicionado por la gran extensión vertical del foco; sin embargo, la ausencia de este mínimo no significa la ausencia del efecto de extensión vertical. El efecto local puede ser evidenciado en el caso del foco inclinado cuando el epicentro local (E_l) se corre a un lado del epicentro normal (E_n) en la mitad del sistema principal de isosistas (Shebalín, 1972).

El efecto macrosísmico de extensión vertical del foco, sensiblemente aumenta a causa de que la parte superior del foco de la ruptura se enriquece de subfuentes (rupturas secundarias) considerablemente en mayor cantidad que la parte inferior, además se crea un exceso de fuentes de radiación "macrosísmica" (de corto periodo) en la parte más superior del foco (Shebalín, 1972).

Un buen modelo de foco con gran extensión vertical lo representa el sistema de dos fuentes. Uno de ellos, el cual representa el centro geométrico de la parte principal del foco es designado como O_n; su profundidad se denomina "profundidad normal, dada por h_n". La segunda fuente, que responde al centro de la parte más superior del foco, es designada por O_l, su profundidad es h_l. La extensión vertical del foco se define por la relación entre h_n y h_l de la siguiente manera (Shebalin, 1971, 1972):

$$l_z = 1{,}5(h_n - h_l) \tag{8}$$

Si el efecto macrosísmico de extensión vertical del foco no se expresa claramente en el mapa de isosistas, los datos macrosísmicos sólo permiten realizar el cálculo para la definición de la profundidad normal del foco del terremoto, por cuanto son dos métodos independientes. El decrecimiento relativo de las isosistas con la distancia define la profundidad local del foco, designada por h_l (Shebalin, 1971).

4. Método

4.1 Modelo Blake-Shebalín

En términos generales, el modelo Blake-Shebalín para la representación del campo macrosísmico, es expresado mediante la siguiente ecuación:

$$I_i = a_i - \gamma \log x_i \tag{9}$$

Comprando las ecuaciones (1) y (3) para focos superficiales ($h \to 0$), se puede ver que $a_i = I_0$ y $\gamma log\ x_i = f(x_i)$.

Ahora, derivando (3) respecto a x_I e invirtiendo términos, se obtiene:

$$\frac{dx}{dl} = (-2,303/\gamma)x \tag{10}$$

Análogamente, para focos no superficiales se tiene que:

$$\frac{dr}{dl} = \left(-2,303/\gamma\right)r \tag{11}$$

Integrando la ecuación 11 se establece que:

$$\ln r = \frac{-2,303}{\gamma} I + k \tag{12}$$

En el epicentro, donde $I = I_0$ y $r = h$ se tiene

$$\ln(h) = -2,303/\gamma(I_0) + k \tag{13}$$

Eliminando la constante k a partir de las ecuaciones (12) y (13) y despejando I, se llega al postulado de Blake-Shebalín, que en términos de la i-ésima isosista es expresado como:

$$I_i = I_0 - \gamma \log(r_i/h) \tag{14}$$

De esta manera, la ecuación (14) define el campo macrosísmico cuando la atenuación anelástica de las ondas sísmica es despreciable en comparación con la atenuación geométrica, de tal manera que γ es el coeficiente de atenuación geométrica, por tanto, denominado también como coeficiente de Blake-Shebalín.

4.2 Determinación de la profundidad focal a partir del Modelo Blake-Shebalín

La determinación de la profundidad del foco de un terremoto se logra satisfactoriamente usando la ecuación (14) siempre y cuando sea conocido el coeficiente de Blake-Shebalín, que representa la atenuación geométrica en la ecuación general del campo macrosísmico, de tal manera que h se determina por la siguiente expresión:

$$h_n = \frac{1}{N}\sum_{i=1}^{n} \frac{x_1}{\sqrt{\left(10^{2(I_0 - I_i)/\gamma} - 1\right)}} \tag{15}$$

Donde N es el número total de isosistas correspondiente al campo macrosísmico normal del terremoto y x_j es la distancia epicentral de la i-ésima isosista.

En la ecuación (15) h_n representa la profundidad normal del terremoto, la cual es asociada con el lugar donde inicia la ruptura. La profundidad local h_l, que corresponde a la prolongación y culminación de la ruptura, y a la cual se asocian los efectos locales del terremoto, se determina por la expresión:

$$h_l = \frac{x_j}{\sqrt{\left(10^{2(I_0 - I_j)\gamma} - 1\right)}} \tag{16}$$

En este caso, x corresponde a las isosistas de mayor valor que claramente indican el incremento de la intensidad para la generación de efectos locales. Tanto en la ecuación (15) como (16) el coeficiente de Blake-Shebalín (γ), puede ser determinado por la siguiente relación (Shebalín, 1968):

$$\gamma = -\frac{2}{\log(S_i / S_{i+1})} \tag{17}$$

donde; S_i es el área de i-ésima isosista.

Como puede verse, el coeficiente de Blake-Shebalín (γ) no depende explícitamente de la profundidad focal. El área de las isosistas se obtiene directamente del mapa de isosistas, a diferencia de la profundidad que se calcula a partir de los datos que se deducen de las isosistas (x_i, I_i e I_0). Como se muestra a continuación, el coeficiente de Blake-Shebalín (γ) tiene un error asociado muy pequeño.

4.3 Determinación de la Magnitud, Energía, Momento Sísmico y Aceleración

Para determinar estos parámetros sismológicos del terremoto del 05 de febrero de 1938, se aplicaron relaciones empíricas propuestas en la literatura que han sido usadas exitosamente en otras regiones del mundo. Dichas relaciones se específican más adelante con los resultados obtenidos.

5. Datos macrosísmicos utilizados

Para la evaluación de la profundidad focal y demás parámetros sismológicos del terremoto del 5 de febrero de 1938 ocurrido en el Eje Cafetero (Colombia) se utilizó el mapa de isosistas (Figura 4) propuesto por Espinosa (1996), a partir del cual, usando sistemas de información geográfica, se determinó datos del área y el radio equivalente de cada una de las isosistas en la elongación principal de las mismas y en el sentido transversal, es decir, en las direcciones SSO–NNE y SEE–NOO, respectivamente.

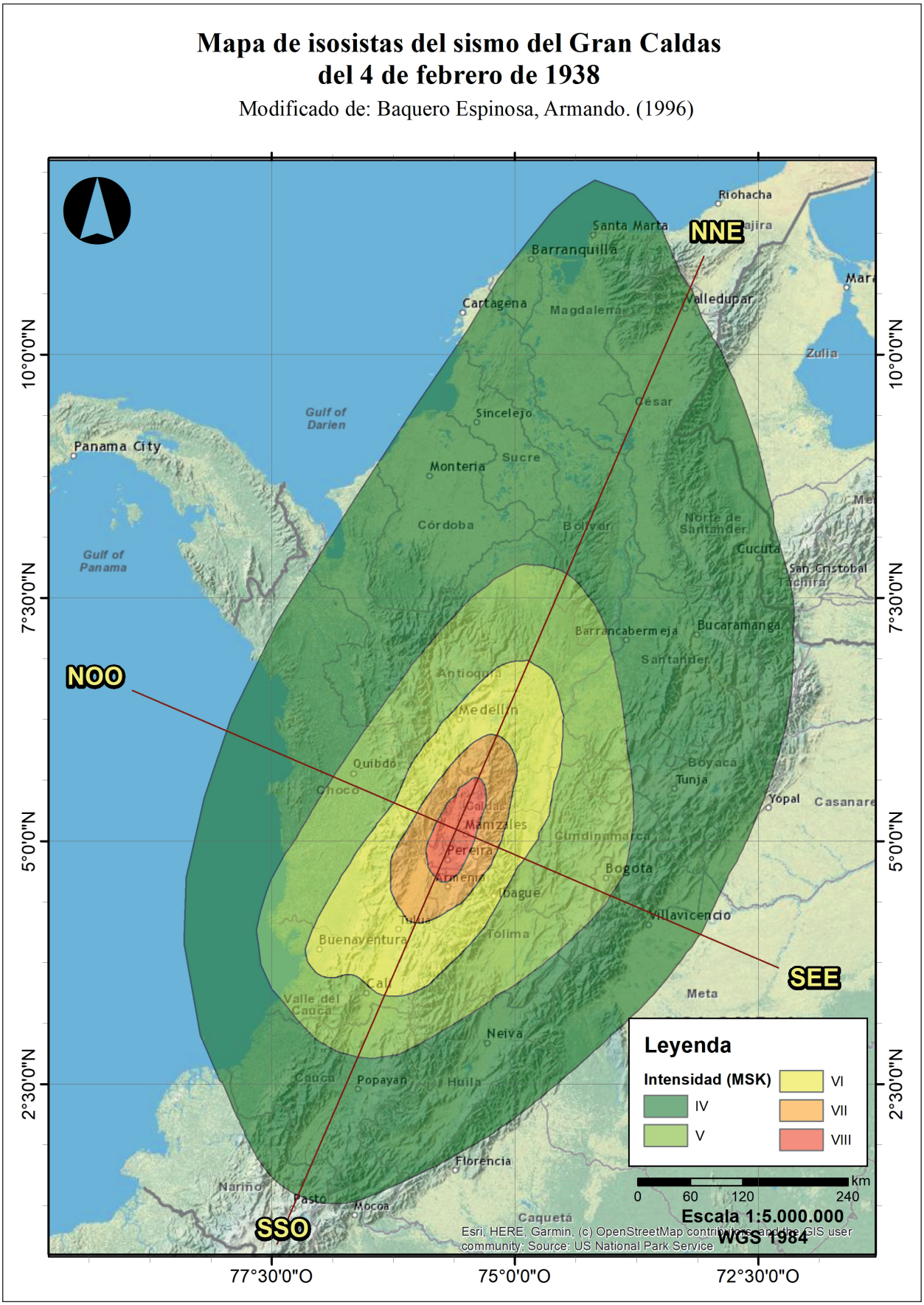

Figura 4. Mapa de isosistas del terremoto del 05 de febrero de 1938 ocurrido en la región del Eje Cafetero – Colombia (Fuente: adaptado de Espinosa, 1996).

5.1 Área y radio equivalente de las isosistas

El Instituto Geográfico Agustín Codazzi (IGAC, 2016) indica que el área continental de Colombia es de aproximadamente un poco más de 1.140.000 km^2, al comparar esta área con las áreas calculadas para cada isosista del sismo de 1938 (Tabla 2), se encuentra que en más del 40% del territorio continental del país se presentaron efectos del sismo, representados con intensidades entre IV y VIII en la escala macrosísmica MSK (Espinosa, 1996).

En la Tabla 3 se presentan los resultados de las mediciones de los radios equivalentes para cada una de las isosistas, estas mediciones se realizan desde el punto central donde se cruzan las líneas imaginarias que dividen las isosistas en las direcciones NNE-SSO y NOO-SEE, hasta el límite en cada dirección de las isosistas.

Tabla 2. Área de las isosistas del terremoto del 05 de febrero de 1938 (Fuente: elaboración propia).

Intensidad	Área (km^2)
IV	514.666
V	155.672
VI	60.117
VII	18.704
VIII	4.792

Tabla 3. Radios equivalentes en diferentes direcciones de elongación para cada una de las isosistas del terremoto del 05 de febrero de 1938 (Fuente: elaboración propia).

Intensidad	RADIOS (km)			
	NWW	NNE	SEE	SSW
IV	343.3	672.3	303.1	453.6
V	152.2	316.6	191.5	282.3
VI	76.6	208.4	85.1	205.7
VII	48.3	116.1	52.7	116.3
VIII	24.1	63.5	24.4	60.0

Tabla 4. Parámetros de círculos de geometría mínima de delimitación (Fuente: elaboración propia).

Isosista circular	Área (km^2)	$\frac{S_{i+1}}{S_i}$	Radio (km) R_i	$\frac{R_{i+1}}{R_i}$
IV	1.140.270	0.25	602.5	0.50
V	286.234	0.51	301.9	0.71
VI	146.060	0.30	215.6	0.54
VII	43.043	0.29	117.0	0.53
VIII	12.376	--	62.8	--

5.2 Círculos de geometría mínima de delimitación

La geometría mínima de delimitación es definida por el *Environmental System Research Institute* (ESRI, 2019), como la entidad geométrica mínima de delimitación que engloba a una entidad o grupo de entidades de entrada, en este caso las isosistas de intensidades. Cómo se explicó anteriormente, el trazado de dichas isosistas puede ser simplificado al dibujarse de manera circular, obteniendo como resultado para el caso de las isosistas del terremoto de 1938, los datos especificados en la Tabla 4.

6. Resultados

La aplicación del modelo Blake-Shebalín y otras relaciones empíricas propuestas en la literatura, y el uso de los datos extraídos de las curvas de isosistas, permitieron determinar los principales parámetros sismológicos del terremoto ocurrido el 05 de febrero de 1938 en el territorio colombiano.

6.1 Epicentro y profundidad focal

El epicentro macrosísmico corresponde a la localización del baricentro de la isosista de mayor intensidad, el cual se determinó en las coordenadas $\Phi = 5.102°$ N y $\lambda = 75.603°$ O, en cercanía al corregimiento El Rubí, perteneciente al municipio de Manizales en el departamento de Caldas.

Para calcular la profundidad normal, se determinó el coeficiente de atenuación sísmica de Blake-Shebalín (γ) usando las áreas de las isosistas de intensidad IV y V, arrojando un valor de 3.85.

Así, la profundidad normal del terremoto, se calculó a partir del coeficiente de atenuación sísmica y los radios de las isosistas circulares, siguiendo el modelo Blake-Shebalín, de tal manera que la profundidad focal es $h_n = 62.9$ km. El error medio asociado a la profundidad, se determinó usando el procedimiento propuesto por Gómez y Salcedo (2002), siendo $\Delta h_n = 1.44$ km. Por tanto, la profundidad focal normal, obtenida mediante datos macrosísmicos corresponde a $h_n = 62.9 \pm 1.44$ km.

Los parámetros obtenidos de localización epicentral y profundidad del terremoto del 5 de febrero de 1938, permiten clasificarlo como un evento de profundidad intermedia, asociado con el plano de Benioff del segmento centro de la zona subducción de la Placa Nazca, la cual, se caracteriza por presentar sismicidad de profundidad intermedia que aumenta conforme pasa por debajo de la cordillera central Colombiana (Figura 5).

6.2 Magnitud, Energía, Momento Sísmico y Aceleración

Se ha realizado el cálculo de la magnitud del sismo, para este propósito se utiliza la relación empírica propuesta por Karnik (1969), válida para cualquier región siendo conocida la profundidad h. Se expresa de la siguiente manera:

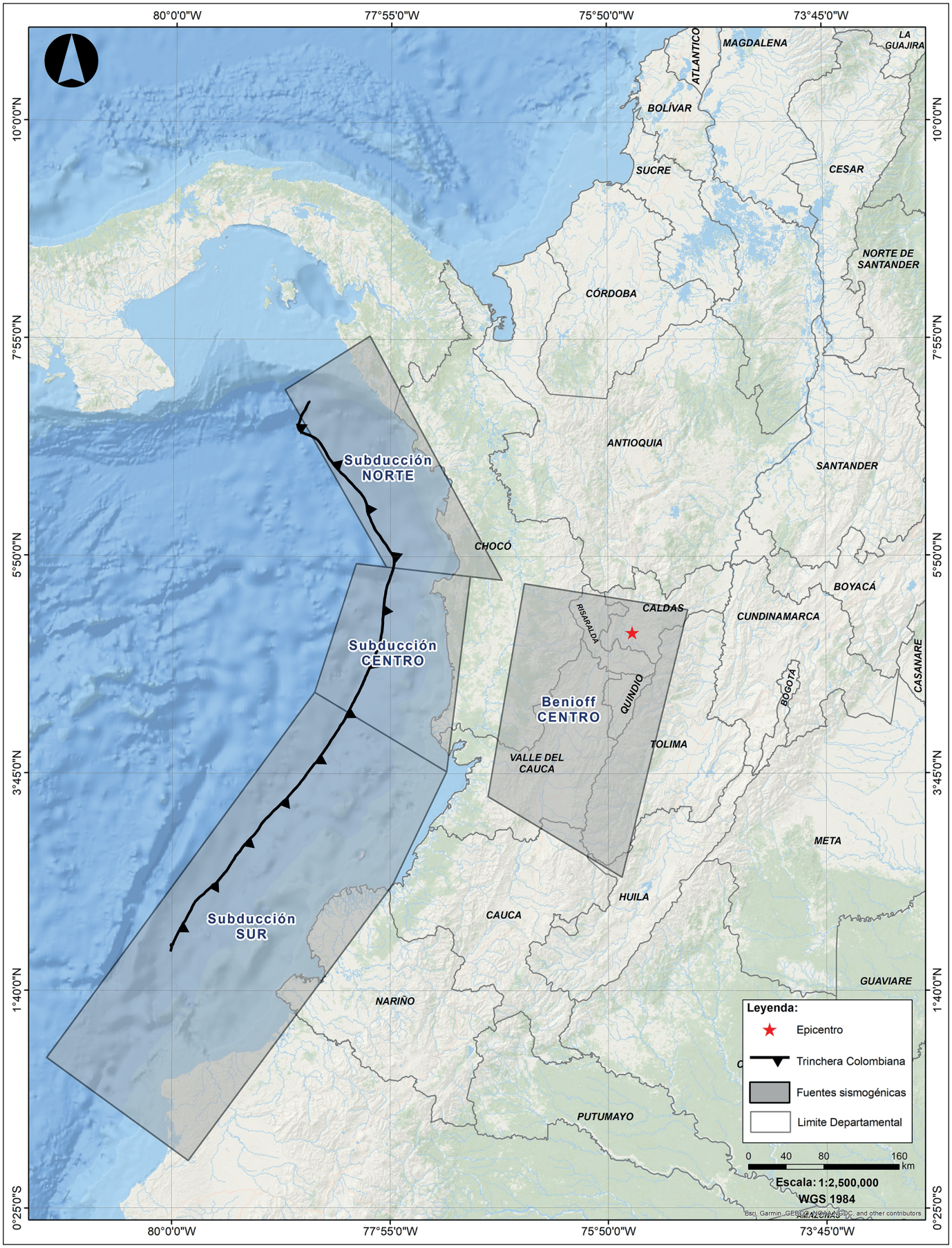

Figura 5. Fuentes asociadas al proceso de subducción. (Fuente: INGEOMINAS & DAGMA, 2005).

$$M=0,5I_0+\log h_n+0,35 \quad (21)$$

Donde $M = Ms$ para $h < 60$ km y $M = mB$ para $h \geq 60$ km (Gutdeutsch, Kaiser, Jentzsch, 2002).

Para el caso del terremoto del 5 de febrero de 1938 el valor de M es igual a *6.2*.

A partir de las intensidades consideradas en el mapa de isosistas, también es posible realizar un cálculo aproximado de la magnitud *Ms* considerando la siguiente ecuación (Bommer, 1994):

$$Ms = 0,83Log(r_3^2) + 0,28I_0 - 0,13 \quad (22)$$

Ms – magnitud de ondas superficiales, r_3 – radio equivalente del límite de perceptibilidad (en kilómetros) y I_0 – intensidad epicentral o la máxima intensidad registrada. El límite de perceptibilidad del terremoto está definido como el área comprendida entre las isosistas de mayor valor y la de intensidad III (Bommer, 1994). De donde:

$$\log E=11,1+6,4\log R-3,2\log h \quad (23)$$

Donde *E*, es la Energía; *R*, el radio de perceptibilidad, y *h* la profundidad hipocentral.

Según Gutenberg and Richter (1942), estas dos ecuaciones pueden usarse para calcular la magnitud y la energía sísmica si la profundidad es conocida; sin embargo, los resultados disminuyen en fiabilidad a medida que aumenta la profundidad. En parte debido las suposiciones involucradas en el desarrollo de dichas ecuaciones, pero también debe considerarse que los valores de I_0 y R generalmente son inciertos para los terremotos de foco profundo.

Bajo esta consideración, para el cálculo de estos parámetros se hace uso de los datos del radio de percepción *N* (Tabla 4) y la profundidad focal h_n determinados anteriormente. Con ello se obtiene lo siguiente:

$$Ms = 6.7$$
$$E = 1.37*10^{23} \text{ ergios}$$

Según Ambraseys & Bommer (1990), la magnitud M_L se adquiere a partir del valor de la magnitud *Ms*, utilizando la siguiente expresión:

$$M_L=0,7M_S+1,46 \quad (24)$$

Por tanto,

$$M_L = 6.2$$

De acuerdo con (Kanamori, 1977; Kanamori, 1983; Abe, 1982; Sauter, 1989; Bormann and Giacomo, 2010), el momento sísmico escalar puede ser calculado en términos la energía sísmica liberada a partir de la siguiente relación:

$$E = \frac{Mo}{2*10^4} \quad (25)$$

Conocida *E*, energía liberada, expresada en *dinas-cm* (aproximadamente), se determina que M_0, momento sísmico escalar, es equivalente a:

$$M_0 = 2.74*10^{27} \text{ dinas-cm}$$

La ecuación (25) fue propuesta por Kanamori (1977) para terremotos superficiales a partir de argumentos elasto-estáticos; sin embargo, Vassiliou and Kanamori (1982) sugirieron que esta relación energía-momento también puede ser aplicada a terremotos profundos. De igual manera, Kanamori propuso la magnitud de momento *Mw* para eventos profundos y superficiales, a partir de M_0, expresada como (Kanamori, 1983):

$$M_w = -\frac{2}{3}\log M_0 - 10,7 \quad (26)$$

De esta manera, usando los datos obtenidos, se tiene los siguientes valores de *Mw*:

$$Mw = 7.6$$

Por último, Gutenberg and Richter (1942, 1956) proponen una relación empírica entre la intensidad macrosísmica y la aceleración sísmica expresa de la siguiente manera:

$$\log a = \frac{1}{3} - 1/2 \quad (27)$$

Señalan los autores que esta relación es idéntica a la obtenida por Cancani en 1904 a partir de los datos de Omori y Milne, con los que se formularon las bases de la asignación de intensidades en la escala macrosísmica de Mercalli. Así, la aceleración calculada es:

$$a = 146.78 \text{ cm/seg}^2$$

equivalente a:

$$a = 0.15\ g$$

En resumen, los parámetros sismológicos obtenidos a partir de datos macrosísmicos para el terremoto del 05 de febrero de 1938 en la región del Eje Cafetero colombiano, se presentan en la Tabla 5.

Tabla 5. Parámetros sismológicos del terremoto del 05 de febrero de 1938, obtenido en el presente estudio a partir de datos macrosísmicos (Fuente: elaboración propia).

Parámetro sismológico	Símbolo	Unidad	Valor
Epicentro macrosísmico normal	E_n	grados	$\phi = 5.102°$ N; $\lambda = 75.603°$ O
Coeficiente de expansión geométrica	γ	adimensional	3.85
Profundidad normal del foco	h_n	km	62.9±1.44
Intensidad macrosísmica máxima	I_0	escala EMS-98	VIII (8)
Magnitud	M = mB	adimensional	6.2
Energía sísmica liberada	E	ergios	$1.37*10^{23}$
Momento sísmico escalar	M_0	dinas-cm	$2.74*10^{27}$
Magnitud de ondas superficiales	Ms	adimensional	6.7
Magnitud Local	M_L	adimensional	6.2
Magnitud momento sísmico	M_w	adimensional	7.6
Aceleración sísmica	a	cm/seg^2	146.78 ≈ 0.15g

Discusión

Es habitual que en muchas regiones sismoactivas del planeta, los terremotos más grandes ocurrieran en momentos donde estas no poseían redes sismológicas, e incluso, aunque se encontrasen instaladas redes de este tipo, las condiciones técnicas no permitían el registro de la magnitud real de los eventos. Teniendo en cuenta, que los sismos de grandes magnitudes cuentan con periodos de retorno lo suficientemente grandes, como para no aparecer en catálogos nacionales con un adecuado registro de los distintos parámetros sismológicos, existe la dificultad para incluir en los estudios de amenaza y riesgo sísmico todos los eventos que han sido determinantes en el territorio.

Aunque se le pueda atribuir un carácter subjetivo a las asignaciones de los valores de intensidad y exista algún tipo de error e incertidumbre por la naturaleza de los datos utilizados, se puede decir que su uso mediante métodos macrosísmicos robustos, permite hacer una valoración apropiada de los parámetros sismológicos de terremotos ocurridos en cualquier región geográfica, y complementar los estudios y análisis que se desarrollen en torno a la caracterización de eventos sísmicos históricos o recientes donde no se cuente con la adecuada cobertura y sensibilidad de redes sismológicas.

Lo obtenido en el presente estudio para el sismo del 5 de febrero de 1938, muestra un avance significativo en el conocimiento de las características físicas del evento en comparación con lo abordado hasta el momento por otros estudios (Tabla 6). Se rebasa en el número de parámetros estimados, presentándose como datos nuevos, dado que ningún trabajo las había abordado, el coeficiente de expansión geométrica, el momento sísmico, la energía sísmica liberada y la aceleración sísmica. De igual forma, se encuentran algunas diferencias con lo publicado por otros autores, relacionadas posiblemente con el set de datos y los métodos utilizados para el análisis.

En la presente investigación se obtiene como resultado una profundidad intermedia 62.9±1.44 km, menor que lo reportado en estudios anteriores (Figura 6a), encontrando correlación con el marco tectónico y las características de la sismicidad en la región donde tuvo lugar el sismo bajo estudio. En relación con el epicentro macrosísmico se localiza en el departamento de Caldas en las coordenadas ($\phi = 5.102°$N; $\lambda = -75.603°$W), cercano a lo propuesto por Ramírez (1975) y Espinosa (1996) (Figura 6b).

La localización estimada, difiere de los reportes instrumentales que inicialmente determinaron el epicentro del terremoto a unos cuantos kilómetros de la cabecera municipal de El Dovio en el departamento del Valle del Cauca, el cual, posteriormente fue relocalizando un poco más al nororiente del departamento en cercanías al municipio de Obando y también en el municipio de Filandia en el departamento de Quindío. La localización del hipocentro definida en el presente estudio tiene correspondencia con el marco tectónico de la región, de tal manera que este evento puede ser atribuido a la zona de Benioff Centro (ver Figura 5), teniendo bastante coincidencia con la sismicidad reciente presentada en dicha zona.

El presente trabajo calcula las magnitudes *M*, M_L, *Mw* y *Ms* (Tabla 6). Se encuentra una fuerte correlación con el valor de *Mw* propuesto por el SGC (2015), el cual es de 7.5 y el obtenido en este estudio de 7.6. El valor de M_L obtenido es inferior a lo presentado por Engdahl & Villaseñor (2002), quienes proponen un rango de 7.1-7.4. Situación que sucede de manera similar con las magnitudes *M*, *Ms* y *mB* que son inferiores a las presentadas en los estudios anteriores. El valor estimado de *M* es de 6.2 a diferencia del presentado por Gutenberg & Richter (1954) de 7.0. Para la *Ms* se obtiene un valor de 6.7, mientas que (Goberna *et al.*, 1985; SGC, 2015) la definen en 7.0. Finalmente, el valor *mB* inferido a partir del cálculo de la magnitud *M* es de

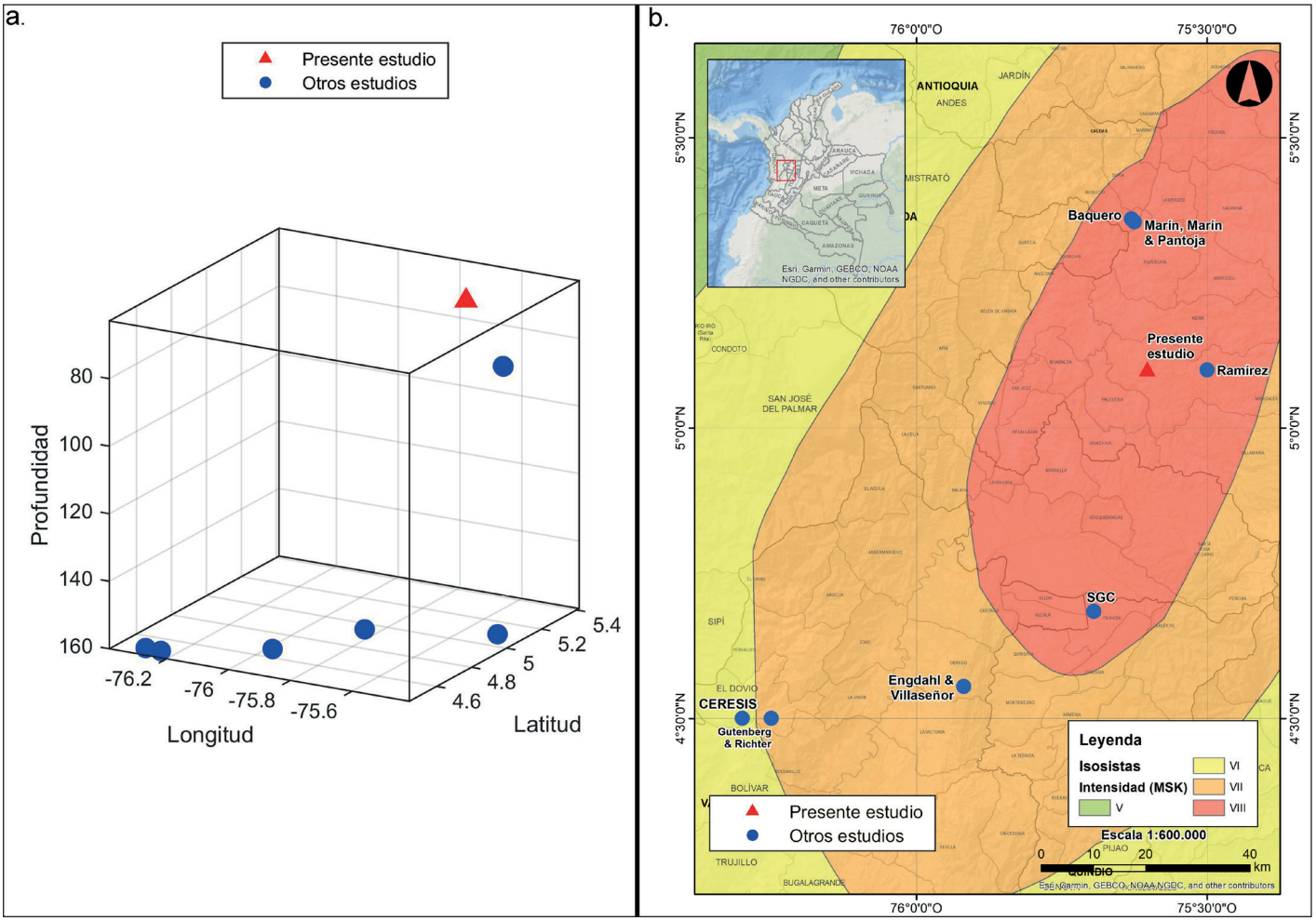

Figura 6. Representación de parámetros hipocentrales macrosísmicos e instrumentales obtenidos del terremoto del 5 de febrero de 1938: a) comparación de la profundidad reportada por otros autores y el presente estudio, el triángulo rojo representa la localización hipocentral obtenida en el presente estudio y los puntos de color azul corresponden a las localizaciones dadas por otras fuentes; b) comparación del epicentro reportado en diferentes estudios (Fuente: elaboración propia).

6.2, en contraste con el valor de 6.9 que definen Engdahl & Villaseñor (2002).

Los catálogos de eventos históricos permiten identificar que en la zona de estudio desde el año de 1884 hasta el 2008, se han presentado alrededor de 5 eventos, con magnitudes *Mw* entre 5.5 a 6.5 y profundidades que van desde los 60 km a los 135 km, lo que permite determinar un periodo de retorno de 24.8 años (Ramírez, 1975; Goberna *et al.*, 1985; Espinosa, 1996 y 2012).

Tabla 6. Comparación de los parámetros físicos del terremoto del 5 de febrero de 1938 (Fuente: elaboración propia).

Parámetro sismológico del terremoto del 05 de febrero de 1938	Resultados	Estudios anteriores						
	Presente Estudio (2023)	Gutenberg & Richter (1954)	Ramírez (1975)	Goberna et al. (1985)	Espinosa (1996)	Engdahl & Villaseñor (2002)	Marín et al. (2006)	SGC (2015) Di Giacomo & Sarabia (2021)
Epicentro macrosísmico normal (E_n)	ϕ = 5.102°N λ = 75.603°O	---	ϕ = 5.100°N λ = 75.500°O	---	ϕ = 5.360°N λ = 75.630°O	---	ϕ = 5.355°N λ = 75.625°O	---
Epicentro instrumental	---	ϕ = 4.50°N λ = 76.250°O	---	ϕ = 4.50°N λ = 76.300°O	---	ϕ = 4.555°N λ = 75.919°O	---	ϕ = 4.684°N λ = 75.695°O
Coeficiente de expansión geométrica (γ)	3.85	---	---	---	---	---	---	---
Intensidad macrosísmica máxima (I_0	VIII EMS-98	---	VIII (Rosi-Forel)	IX (MM)	VII-IX	---	X (EMS-98)	VIII (EMS-98)
Profundidad normal del foco (h_n) - km	62.9±1.44	--	160	---	>45	---	90	---
Profundidad instrumental- km	--	160	---	160	90	155.7	---	150
Magnitud Local (M_L)	6.2	---	---	---	---	7.1-7.4	---	---
Magnitud momento sísmico (M_w)	7.6	---	---	---	---	---	---	7.5
Magnitud de ondas superficiales (M_s)	6.7	7.0	7.0	7.0	---	---	5.8	7.0
Magnitud de la onda de cuerpo (mB)	6.2	---	---	---	---	6.9	---	---
Momento sísmico escalar (M_0) – dinas·cm	$2.74*10^{27}$	---	---	---	---	---	---	---
Energía sísmica liberada (E) - ergios	$1.37*10^{23}$	---	---	---	---	---	---	---
Aceleración sísmica (a) - cm/seg²	146.78 ≈ 0.15g	---	---	---	---	---	---	---

Conclusiones

El terremoto del 05 de febrero de 1938 ocurrido en la región del eje cafetero colombiano, fue sentido en casi todo el país, causando muchos daños y algunas muertes en varias poblaciones, principalmente en los municipios de la región. Tal es caso del departamento de Caldas, donde municipios como Aguadas, Palermo y Támesis presentaron serias afectaciones en diversas edificaciones municipales y la destrucción de viviendas.

La intensidad macrosísmica de este terremoto dado los efectos que tuvo en el territorio ha sido evaluada en diferentes escalas, siendo la asignación que mejor equivalencia presenta entre las distintas evaluaciones, la correspondiente al nivel VIII en la escala macrosísmica europea EMS-98.

En este trabajo se utiliza el mapa de isosistas propuesto por Espinosa (1996) y a partir de la aplicación de variados métodos de análisis macrosísmico y algunas relaciones empíricas propuestas en la literatura, se determinaron los principales parámetros sismológicos del terremoto del 05 de febrero de 1938. Los resultados arrojan que el epicentro macrosísmico normal (E_n) se localiza a ϕ = 5.102° N; λ = 75.603° O, con una profundidad normal del foco de h_n = 62.9±1.44 km.

La magnitud y energía sísmica liberada se calcularon aplicando las relaciones empíricas propuestas por Karnik (1969), obteniéndose que M=6.2, el valor de la energía sísmica liberada E=$1.37*10^{23}$ ergios y la magnitud de ondas superficiales Ms=6.7. Así mismo, teniendo como referencia la propuesta de Ambraseys & Bommer (1990), a partir del valor Ms, se obtiene la magnitud local M_L= 6.2 y se asume la equivalencia entre M y mB, para sismos mayores a 60 km de profundidad.

De igual manera, usando las relaciones empíricas desarrolladas por Kanamori (1977), se determinó el momento sísmico escalar M_0=2.74*10^{27} dinas-cm y la respectiva magnitud del momento sísmico Mw=7.6. Se obtuvo un valor de aceleración sísmica de 0.15g.

Con el presente estudio se demuestra que los análisis macrosísmicos son un insumo fundamental para la determinación de los parámetros sismológicos de terremotos históricos, lo que conlleva a fortalecer los catálogos sismológico y suministrar información valiosa para la valoración de la amenaza y el riesgo sísmico.

Agradecimientos

El presente trabajo corresponde a los resultados de un proyecto de investigación interno del Observatorio Sismológico y Geofísico del Suroccidente Colombiano perteneciente a la Universidad del Valle - Colombia (OSSO), siendo desarrollado por miembros del Grupo de Investigación Georiesgos, adjunto OSSO, por lo cual expresamos nuestro agradecimiento a los demás miembros del grupo por el apoyo brindado y la discusión dada en torno a los datos resultados obtenidos.

Se agradecen las observaciones y recomendaciones enviadas por los revisores anónimos y por el editor, las cuales han ayudado a mejorar considerablemente el manuscrito

Bibliografía

Abe K.,1982, Magnitude, seismic moment and apparent stress for major deep earthquakes. *J. Phys. Earth*, 30, 321-330.

Ambraseys, N.N., Bommer, J.J., 1990. Uniform magnitude re-evaluation for the strong-motion database of Europe and adjacent areas, Eur. Earthquake Eng., 4, 3–16.

Barazangi, M., Isacks, B. L.,1976, Spatial distribution of earthquakes and subduction of the Nazca plate beneath South America. *Geology, 4*(11), 686-692.

Blake A.,1941, On the Estimation of Focal Depth from Macroseismic Data. *Bull. Seism. Soc. Am.*, 31 (3), 225-231.

Bohorquez, O. P., Monsalve, M. L., Velandia, F., Gil, F., Mora, H., 2005, Marco tectónico de la cadena volcánica más septentrional de la Cordillera Central de Colombia. *Boletín de Geología, 27*(1), 55-79.

Bommer, J., 1994, Sismología para ingenieros. Universidad Centroamericana" José Simeón Cañas".

Bormann P., Di Giacomo D., 2010, The moment magnitude and the energy magnitude: common roots and differences. *Journal of Seismology*,15 (2), 411-427.

Brune J. N, 1970, Tectonic Stress and Spectra of Seismic Shear Waves from Earthquakes. *J. Geophys. Res.*, 75, 4997-5009.

Cifuentes, H. G., Sarabia, A. M., 2007, Estudio macrosísmico del sismo del 4 de febrero de 1938, Eje Cafetero. INGEOMINAS, Informe Interno, 134p.

Condori, C., Pérez, J. L., 2015, Análisis de la variación espacio-temporal del valor de b en el valle del Cauca, suroccidente de Colombia. GEOS, 35 (2), 1-16.

Cortés, M., Angelier, J., 2005, Current states of stress in the northern Andes as indicated by focal mechanisms of earthquakes. *Tectonophysics, 403*(1-4), 29-58.

Dewey, J.W., 1972, Seismicity and tectonics of Western Venezuela. *Bull. Seismol. Soc. Am., 62*, 1711-1751.

Di Giacomo, D., Sarabia, M., 2021. Use of macroseismic and instrumental data to reassess earthquake locations: Examples from pre-digital earthquakes in Colombia. *J. South Am. Earth Sci., 111*, 103467. **https://doi.org/10.1016/j.jsames.2021.103467.**

Engdahl, E., Villaseñor, A, 2002, Global seismicity: 1900 – 1999. USGS. Centennial Earthquake Catalog. University of Colorado, Boulder, 26 pp.

Espinosa, B., A., 2012, Enciclopedia de desastres naturales históricos de Colombia. Volúmenes 1- 7. Academia Colombiana de Ciencias Exactas, Físicas y Naturales, Colombia, [CD-ROM].

Espinosa, A., 1996, Sismicidad histórica. Informe final. Proyecto para la mitigación del riesgo sísmico de Pereira, Dos Quebradas y Santa Rosa de Cabal, Convenio Carder. Universidad del Quindío, Colombia.

ESRI, 2019, Minimun Bounding Geometry. Recuperado el 8 de Agosto de 2019, de ArcGIS Desktop Tools: desktop.arcgis.com/en/arcmap/latest/tools/data-management-toolbox/minimun-bounding-geometry.htm

Freymueller, J. T., Kellogg, J. N., Vega, V, 1993, Plate motions in the North Andean region. *Journal of Geophysical Research: Solid Earth, 98*(B12), 21853-21863.

Goberna, R., Arias, W., Duarte, J., Palencia, T., & Vargas, T., 1985, Catálogo de Terremotos para América del Sur, volumen 4 Colombia. Proyecto SISRA, CERESIS, Lima.

Gómez Capera, A., Salcedo -Hurtado, E. D. J., 2002. Leyes de atenuación de la intensidad macrosísmica en Colombia. *Earth Sciences Research Journal, 6*, 53-61.

Gutenberg, B., Richter, C., 1942, Earthquake Magnitude, Intensity, Energy and Acceleration, *Bull. Seismol. Soc. Am.*, 32,163-191.

Gutenberg, B., Richter, C.,1954, Seismicity of the Earth and Associated Phenomena. Princeton University, Princeton, 310 pp.

Gutenberg, B., Richter, C. F., 1956, Earthquake magnitude, intensity, energy, and acceleration: (Second paper). *Bull. Seismol. Soc. Am.*, 46 (2), 105-145.

Gutdeutsch, R., Kaiser, D., Jentzsch, G., 2002, Estimation of earthquake magnitudes from epicentral intensitiesand other focal parameters in Central and Southern Europe. Geophys. J. Int., 151, 824–834.

Gutscher, M. A., Malavieille, J., Lallemand, S., Collot, J. Y., 1999, Tectonic segmentation of the North Andean margin: impact of the Carnegie Ridge collision. *Earth and Planetary Science Letters*, 168(3-4), 255-270.

Gutscher, M. A., Spakman, W., Bijwaard, H., & Engdahl, E. R. (2000). Geodynamics of flat subduction: Seismicity and tomographic constraints from the Andean margin. *Tectonics, 19*(5), 814-833.

Hall, M. L., & Wood, C. A. (1985). Volcano-tectonic segmentation of the northern Andes. *Geology, 13*(3), 203-207.

Haskell N. A. (1964). Total Energy and Energy Spectral Density of Elastic Waves Radiation Propagating Faults. *Bull. Seism. Soc. Am.*, Vol. 54. p. 1811-1841.

IGAC, 2016, Preguntas Frecuentes. Recuperado el 8 de Agosto de 2019, de Servicios de Información al Ciudadano: **www2.igac.gov.co/igac_web/faqs_user/**

Instituto Colombiano de Geología y Minería (INGEOMINAS), Departamento Administrativo de Gestión del Medio Ambiente (DAGMA), 2005, Estudio de microzonificación sísmica de Santiago de Cali. Subproyecto de sismotectónica. Informe No. 1-6 Caracterización de Fuentes Sísmicas de Subducción. República de Colombia, Ministerio de Minas y Energía, Bogotá, 49 pp.

Isacks, B. L., Molnar, P., 1971, Distribution of stresses in descending lithosphere from a global survey of focalmechanism solutions of mantle earthquakes. Reviews of Geophysics and Space Physics, 9, 103- 174.

Kanamori, H, 1977. The energy release in great earthquakes. *J. Geophys Res.*, 82, 2981-2987.

Kanamori, H, 1983, Magnitude scale and quantification of earthquakes. *Tectonophysics, 93*,185- 199.

Karnik, V., 1969, Seismicity of the European Area, Part 1, Reidel, Dordrecht (KA69).

La Voz de Caldas, 1938, Violenta conmoción causó el temblor en el país. La Voz de Caldas, págs. 1,3,6,8.

Marín, J. P., Marín O. F., Pantoja J. A, 2006, Sismicidad histórica del Departamento de Caldas (Colombia). *Boletín de Geología*, 28 (1), 97 – 110.

Medvedev, S.V., Spohneuer, W. and Karnik, V., 1965, Seismic Intensity Scale Version MSK 1964. Akad. Nauk SSSR, Geofiz. Kom., 10.

Monsalve, H., Mora, H., 2005, Esquema geodinámico regional para el noroccidente de suramérica (modelo de subducción y desplazamientos relativos. *Boletín de Geología, 27* (44), 25- 53.

Pedraza García, P., Vargas, C. A., Monsalve, J., 2007, Geometric model of the Nazca plate subduction in southwest Colombia. *Earth Sciences Research Journal, 11*(2), 124-134.

Pennington, W.D.,1981, Subduction of the eastern Panama Basin and seismotectonics of northwestern South America. *Journal of Geophysical Research, 86* (B11), 10753–10770.

París, G., Machette, M., Dart, R., Kaller, K., 2000, Map and database of Quaternary faults and folds in Colombia its offshore regions. USGS open-file report 00-0284. Map at 2,500,000 scale and report, USA, 66 pp.

Quispe, R., Tavera, H., & Bernal Esquia, I., 2003, Geometría de la Placa de Nazca en el borde occidental de Sudamérica a partir de las tendencias medias de sismicidad. *Boletín de la Sociedad Geológica del Perú, 95*, 93-110.

Ramírez, J. E., 1938, Algunas notas sobre el terremoto colombiano del 4 de febrero de 1938. *Revista Javeriana, 9* (41), 340-344.

Ramírez, J. E., 1975, Historia de los terremotos en Colombia. 2 ed. Instituto Geográfico Agustín Codazzi (IGAC), Bogotá, 250 pp.

Rodríguez-Navarro, J., 1944, La forma de las isosistas en relación con la estructura geológica del terreno en el sismo de 20 de marzo de 1933. *Rev. Geofísica, 3*, 251 pp.

Santó, T., 1969, Characteristics of the seismicity in South America. *Bull. Earthq. Res. Inst.,47*, 635- 672.

Sauter, F., 1989, Introducción a la sismología. Fundamentos de ingeniería sísmica. Editorial Tecnológica de Costa Rica, Cartago, 270 pp.

Savage, J. C., 1966, Radiation from a Realistic Model of Faulting. *Bull. Seism. Soc. Am., 56*, 577-592.

Servicio Geológico Colombiano (SGC), 2015, IV Simulacro Nacional 2015. Escenario sísmico (Primera versión). Dirección de Geoamenazas, Bogotá, 9 pp.

Shebalin N.V., 1968. Methods to use engineering and seismological data for seismic zoning. In: Seismic Zoning of the USSR. Nauka, Moscow, p. 95–111 (in Russian) [Шебалин Н.В. Методы использования инженерно-сейсмологических данных при сейсмическом районировании // Сейсмическое районирование СССР. М.: Наука, 1968. С. 95–111].

Shebalin, N. V., 1971, Estimation of sizes and focal position of Tashkent earthquake from macroseismic and instrumental data. In: Tashkent earthquake 1966. Tashkent: FAN. p. 68–79 (in Russian). [Шебалин Н.В. Оценка размеров и положения очага Ташкентского землетрясения по макросейсмическим и инструментальным данным // Ташкентское землетрясение 1966. Ташкент: ФАН, 1971. С. 68–79].

Shebalin, N. V. 1972. Macroseismic data as information on source parameters of large earthquakes. *Physics of the Earth and Planetary Interiors, 6*(4), 316–323. doi:10.1016/0031-9201(72)90016-7.

Shebalin, N. V., 1991, Estimation of the size and position of the Spitak earthquake source from macroseismic data, Vopr. Inzh. Seismol, 32, 36-44. (in Russian). [Шебалин Н.В. Оценка размеров и положения очага спитакского землетрясения по макросейсмический данным // Вопросы инженерной сейсмологии, 32. М.: Наука, 1991. С. 36-44].

Taboada, A., Dimaté, C., Fuenzalida, A., 1998, Sismotectónica de Colombia: deformación continental activa y subducción. *Física de la Tierra, 11*, 111- 147.

Taboada, A., Rivera, L.A., Fuenzalida, A., Cisternas, A., Philip, H., Bijwaard, H., Olaya, J., Rivera, C., 2000. Geodynamics of the nothern Andes: Subductions and intracontinental deformation (Colombia). Tectonics, 19 (5), 787- 813.

Vassiliou, M. S., Kanamori, H., 1982, The energy release in earthquakes. *Bull. Seism. Soc. Am., 72*, 371-387.

Wiemer, S., Wyss, M.,1997, Mapping the frequency-magnitude distribution in asperities: An improved technique to calculate recurrence times?. *Journal of Geophysical Research: Solid Earth, 102*(B7), 15115-15128.

Zuniga, F. R., Wyss, M., 2001, Most-and least-likely locations of large to great earthquakes along the Pacific coast of Mexico estimated from local recurrence times based on b-values. *Bull. Seism. Soc. Am., 91*(6), 1717-1728.

Geofísica Internacional (2023) **62-3**: 543 - 561

Disturbances in the geomagnetic field, water level and atmospheric pressure associated with Mw ≥ 6.6 earthquakes in the South Atlantic Ocean

M.A. Arecco[1,2]*, P.A. Larocca[1], F.A. Oreiro[1,3], M.E. Fiore[1,3], L.A. Otero[4,5], M.F. Canero[3]

Abstract

This paper is aimed at studying disturbances in the geomagnetic field (GMF), water level (WL) and sea-level atmospheric pressure (AP) associated with Mw≥ 6.6 seismic events in the Scotia arch, in the South Atlantic. GMF records from observatories of the International Magnetic Observatory Network (INTERMAGNET), WL records from tide stations of the Intergovernmental Oceanographic Commission, and hourly AP records from databases of the Global Modeling and Assimilation Office of the National Aeronautics and Space Administration have been analyzed in the area under study. For the analysis of geomagnetic disturbances, the GMF horizontal component (H), which is more susceptible to variations, was considered. For the WL analysis, the discrepancy (residue) between the WL time series from tide stations and the predicted level of astronomical tides, for a 10-day period before and after the occurrence of each earthquake, was calculated. For the AP analysis, the variation of data gridded between 1 and 2 hours before and after the earthquake was calculated. The analysis of the geomagnetic data prior to the seismic event, using a high-pass filter and the wavelet method, showed: a) high energy ranges in all frequencies, even in very high ones; and b) oscillations in the filter with amplitude peaks of ± 0.2 nT, and with an anticipation and duration consistent with the wavelet method. As regards the WL residues calculated, there were oscillations in the largest amplitudes in the sensors located closest to the earthquake, thus, those large amplitudes corresponded to shorter times of arrival. The AP study showed a maximum followed by a local minimum within a range of ± 0.3 hPa around the location of the earthquake. While the GMF analysis anticipated seismic events within a range of 6-2 hours, the techniques used for WL and AP could detect Mw>7 earthquakes, associating them with the rising/falling surface of the sea. These three techniques can be used jointly to implement a prevention or early warning system for seismic events or related hazards such as tsunamis and/or seiches in the study region.

Key words: Earthquakes, Atmospheric pressure, Tsunamis, Horizontal component of the geomagnetic field, Sunspots.

Resumen

Este trabajo tiene como objetivo estudiar las perturbaciones en el campo geomagnético (GMF), nivel del agua (WL) y presión atmosférica a nivel del mar (AP) asociadas a eventos sísmicos Mw≥ 6.6 en el arco de Scotia, en el Atlántico Sur. Registros GMF de los observatorios de la Red Internacional de Observatorios Magnéticos (INTERMAGNET), registros WL de las estaciones de mareas de la Comisión Oceanográfica Intergubernamental y registros AP por hora de las bases de datos de la Oficina Global de Modelado y Asimilación de la Administración Nacional de Aeronáutica y el Espacio han sido analizadas en el área de estudio. Para el análisis de perturbaciones geomagnéticas se consideró la componente horizontal GMF, la cual es más susceptible a variaciones. Para el análisis WL, se calculó la discrepancia (residuo) entre la serie temporal WL de las estaciones de mareas y el nivel pronosticado de las mareas astronómicas, durante un período de 10 días antes y después de la ocurrencia de cada terremoto. Para el análisis AP se calculó la variación de los datos grillados entre 1 y 2 horas antes y después del sismo. El análisis de los datos geomagnéticos previos al evento sísmico, utilizando un filtro de paso alto y el método wavelet, mostró: a) altos rangos de energía en todas las frecuencias, incluso en las muy altas; y b) oscilaciones en el filtro con picos de amplitud de ± 0.2 nT, y con una anticipación y duración consistente con el método wavelet. En cuanto a los residuos WL calculados, hubo oscilaciones en las mayores amplitudes en los sensores ubicados más cerca del sismo, por lo que esas grandes amplitudes correspondieron a tiempos de llegada más cortos. El estudio AP mostró un máximo seguido de un

Palabras clave: Terremotos, Presión atmosférica, Tsunamis, Componente horizontal del campo geomagnético, Manchas solares.

Received: November 8, 2022; Accepted: June 23, 2023; Published on-line: July 1, 2023.

Editorial responsibility: Dr. Juan Esteban Hernández Quintero

* Corresponding author: M.A. Arecco marecco@fi.uba.ar
[1] Universidad de Buenos Aires, Facultad de Ingeniería, Instituto de Geodesia y Geofísica Aplicadas. Buenos Aires, Argentina.
[2] Universidad de la Defensa Nacional, Facultad de la Armada, Escuela de Ciencias del Mar, Buenos Aires, Argentina.
[3] Ministerio de Defensa, Servicio de Hidrografía Naval, Buenos Aires, Argentina.
[4] Universidad de la Defensa Nacional, Facultad de Ingeniería del Ejército, Buenos Aires, Argentina.
[5] Ministerio de Defensa, CITEDEF – CONICET, Villa Martelli, Argentina.

María Alejandra Arecco, Patricia Alejandra Larocca, Fernando Ariel Oreiro, Mónica María Elisa Fiore, Lidia Ana Otero y María Florencia Canero

https://doi.org/10.22201/igeof.2954436xe.2023.62.3.1440

mínimo local dentro de un rango de ± 0,3 hPa alrededor de la ubicación del terremoto. Mientras que el análisis GMF anticipó eventos sísmicos dentro de un rango de 6-2 horas, las técnicas utilizadas para WL y AP pudieron detectar terremotos Mw>7, asociándolos con la superficie ascendente/descendente del mar. Estas tres técnicas pueden ser utilizadas en conjunto para implementar un sistema de prevención o alerta temprana de eventos sísmicos o peligros relacionados tales como tsunamis y/o seiches en la región de estudio.

Introduction

The South Atlantic Ocean is one of the most active seismic regions in the world, with the Scotia Arc, which surrounds the Scotia and South Sandwich plates. The edges of this active set are represented by various types of margins. The North Scotia Ridge, which extends from Tierra del Fuego, through the Burdwood/Namuncurá Bank, up to the Georgias del Sur Islands, is mainly represented by a transcurrent and convergent margin. This ridge separates the Scotia and Sandwich plates from the South American plate. The eastern edge of the Sandwich plate, represented by the volcanic arc of the Sandwich del Sur Islands, has a convergent margin, mainly developed from N to S by the South Sandwich Trench, which separates it from the South American plate. The western edge of the Scotia plate is represented by the Shackleton Fracture Zone beneath the Drake Passage. The southern edge of the Scotia and Sandwich plates is represented by a mixed transcurrent and accretionary margin, separating it from the Antarctic plate. This margin goes through the South Scotia Ridge, Elephant Island and the Orcadas del Sur Islands up to the southern South Sandwich arc.

The activity is represented by the displacement of the Antarctic plate moving eastwards with respect to the Scotia plate at a rate of around 6 mm/year, and the South American plate subducting beneath the South Sandwich microplate at a rate of around 70 to 80 mm/year. In this region, within one year, there may be over 300 seismic events with a moment magnitude (hereinafter M_w) of M_w>4, and at least one M_w>7 earthquake (Larocca *et al.*, 2019; 2021). The North Scotia Ridge, even though it is less active than the South Ridge, has around 20 M_w>4 earthquakes in a year (Figure 1).

One of the most elusive objectives of seismology is predicting earthquakes in the short term. There are numerous studies reporting associations between earthquakes and physical phenomena, such as electromagnetic field variations (Varotsos *et al.*, 2013; Hayakawa *et al.*, 2010; Takeuchi *et al.*, 2012; Gao *et al.*, 2014; Zhao *et al.*, 2021), anomalous GMF records on the earth's surface (Ruiz *et al.*, 2011; Takla *et al.*, 2018; Arecco *et al.*, 2020; Larocca *et al.*, 2021) or very low frequency changes in the electromagnetic field (Hayakawa *et al.*, 2010; Sierra Figueredo *et al.*, 2020). In addition, Thomas and Juárez (2021) reported significant mechanical effects in the focal region of an earthquake, namely deformation of rocks, changes in their properties or a stress-strain state. Additionally, Paudel *et al.* (2018) and Spivak *et al.* (2019) found changes in the chemical composition and/or ground water temperature. Arai *et al.* (2011) studied AP changes caused by the earthquake off the Western Pacific coast of Tohoku (M_w9.0) in Japan in 2011, identified by means of atmospheric boundary waves excited by the rising and falling surface of the ocean, based on the waveform characteristics and the similarity with the data from water bottom pressure tide gauges.

Dragani *et al.* (2009) studied the vulnerability of the coastlines in the southernmost tip of South America and Antarctica to potential tectonic tsunamis (caused by undersea earthquakes) with epicenters in the region of the Scotia Arc (Orcadas, Georgias del Sur, Sandwich del Sur and Elephant islands). For example, on August 4, 2003, an M_w 7.6 earthquake, whose epicenter was located 71 km ENE of the Orcadas del Sur Islands, in Antarctica, caused a tsunami that was mitigated by the presence of 2 m-thick sea ice surrounding the islands (Roucco and del Valle, 2021). Dragani *et al.* (2009) concluded that, even though the Patagonian coastline shows a relatively low vulnerability to these phenomena, it is necessary to conduct a comprehensive study assessing the potential impact of tsunamis due to the high rate of occurrence of violent geological processes in the Scotia Arc. The joint action of a tsunami, even of a low magnitude, the local tide and the storm surge may aggravate the situation, especially in the case of low areas located a few meters above sea level. Based on observations and numerical modeling, many authors (among them, Ayca and Lynett, 2016; Kowalik and Proshutinsky, 2010; Lee *et al.*, 2015; Shelby *et al.*, 2016) demonstrated that the reach of a tsunami in rivers, coves and estuaries is strongly affected by tidal conditions. Another major factor to be considered is that tsunamis result in periodical oscillations caused by the geometrical features of the area, such as seiches (Rabinovich, 2010). The areas of Puerto Argentino, on the Malvinas Islands, and Mar del Plata and Quequén, in the province of Buenos Aires, promote the formation of seiches. Woodworth *et al.* (2005) detected in Puerto Argentino two continuous energy peaks with 87 and 26 min periods, identified as seiches.

On August 12, 2021 the region was shaken by an M_w7.5 earthquake that was 47 km deep, and three minutes later, by another M_w8.1 earthquake, which was 56 km deep and 90 km away from the previous one. Even though the surge was not destructive, it was the first one since the catastrophic tsunami in 2004, which hit three different oceans (Jia *et al.*, 2022).

This study selected $M_w \geq 6.6$ earthquakes since 1970. The time series of available GMF activity data, sunspot

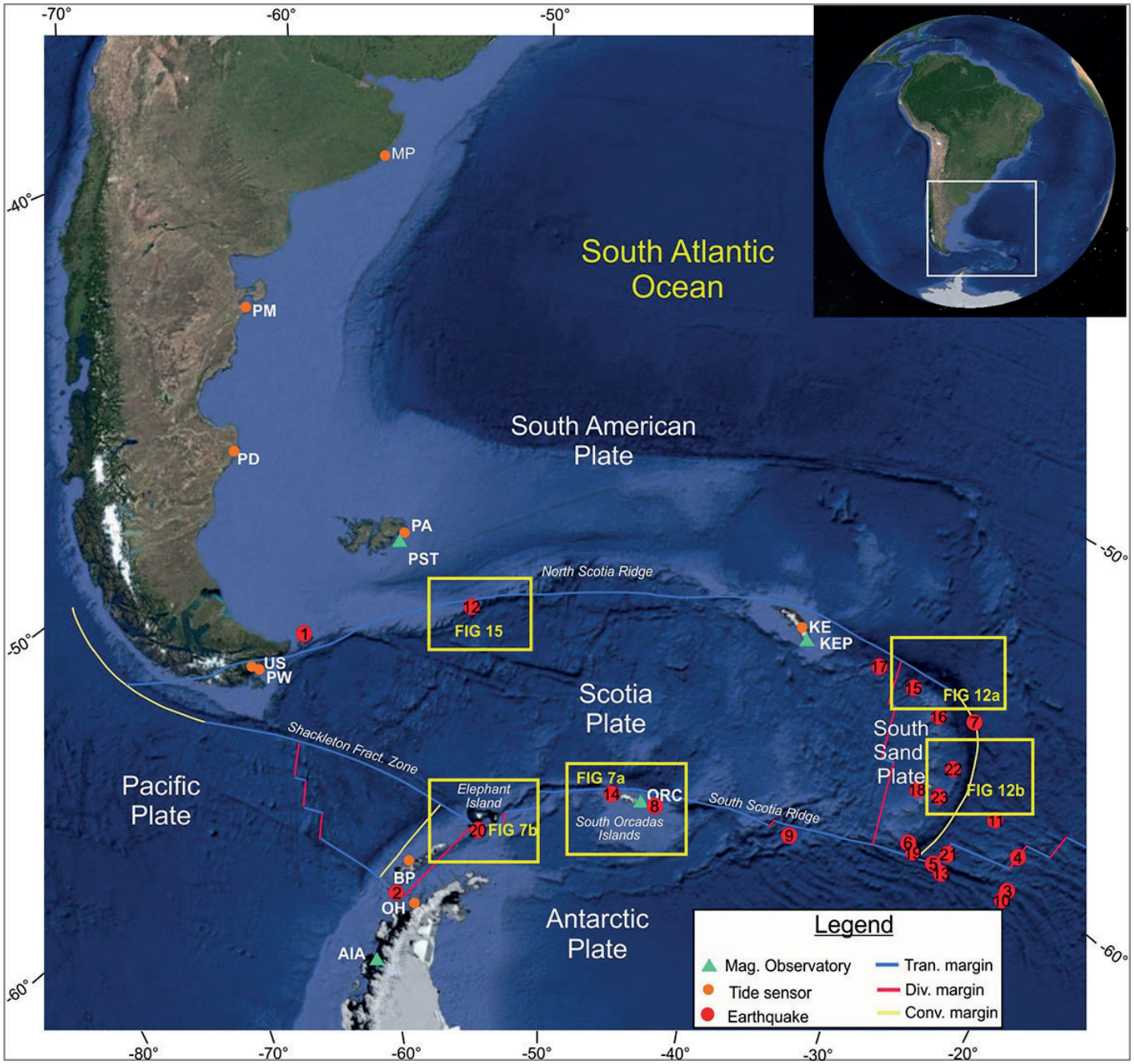

Figure 1. Location of Mw≥6.6 earthquakes in the last 20 years in the South Atlantic. Earthquakes (red circles) numbering of earthquakes in Table 1.. Margins of the South American, Scotia, South Sandwich and Antarctic pates (blue line: transcurrent margin; red line: divergent margin; and yellow line: convergent margin). Geomagnetic observatories (green triangles): Puerto Argentino (PST), King Edward Point (KEP), Argentine Island - Antarctica (AIA), Orcadas Islands (ORC). Tide stations (orange dots): King Edward (KE), Puerto Argentino (PA), Base Prat (BP), O'Higgins (OH), Puerto Williams (PW), Ushuaia (US), Puerto Deseado (PD), Puerto Madryn (PM) and Mar del Plata (MP). (Background photo taken from **http://ds.iris.edu/**)

number, WL from tide stations and AP at ocean level were analyzed. These studies were conducted based on: a) the GMF harmonic analysis applying the wavelet method and frequency filters, b) the analysis of WL residues, obtained after eliminating the astronomical tide effect, and c) the observation of the discrepancies between AP hourly grids and the analysis of the AP time series variation in three to four hours periods.

This study aims at improving the knowledge of the magnetic field, WL and AP in the presence of earthquakes in the area of the Scotia Sea. In addition, maximum heights following significant seismic events in the western coastal regions of the South Atlantic and Antarctica were analyzed as these regions can be reached by potential earthquake-generated tsunamis.

Area Under Study

The Scotia plate is located south of the South American plate, mainly in the South Atlantic Ocean, between parallels 53° S and 63° S and between meridians 25° W and 70° W, formed by oceanic lithosphere and small continental crust fragments of the Georgias del Sur and Orcadas del Sur Islands. Its boundaries are represented by the Shackleton Fracture Zone to the west and a large part of the Scotia Arc to the north, east and south. The north of the Scotia plate is represented by a transcurrent-type margin that goes through southern Tierra del Fuego up to the Georgias del Sur Islands. To the east, this pate has a divergent and also active margin, which separates it from the South Sandwich microplate, and to the south, a mixed margin (divergent and mostly transcurrent) that is represented by the South Scotia Ridge (Figure 1).

The South Sandwich microplate is located east of the Scotia Sea, between coordinates 55° S and 60° S, and it is bounded on the north and east by the South American plate, on the south by the Antarctic plate, and on the west by the Scotia plate. The Sandwich del Sur Islands and their associated seamounts make up the volcanic arc of a highly active subduction system located in the South Atlantic (South Sandwich arc) (Eagles, 2010; Leat *et al.*, 2013, 2016; Dalziel *et al.*, 2013; Maldonado *et al.*, 2013, 2015) (Figure 1).

The subduction area of the South American plate beneath the South Sandwich plate is one of the regions with the highest seismic activity in the planet (Beniest and Schellart, 2020; Larocca *et al.*, 2019; 2021). In addition, it is one of the regions in the Atlantic Ocean with a great potential to generate tsunamis due to its seismic and volcanic activity (Dragani *et al.*, 2006; 2009). These authors detected sea level oscillations in the order of 20 cm on the shores of the province of Buenos Aires caused by the M_w9.3 earthquake that hit the western coastline of northern Sumatra over 15,000 km away on December 26, 2004.

Since 1970, in this area there have been more than 20 M_w>6.6 seismic events, of which over a half have exceeded a magnitude of M_w7 (Table 1). The largest in this series, reaching M_w8.1, occurred on August 12, 2021 south of the region of the Sandwich del Sur Islands, and the following one in intensity reached M_w7.7, on November 17, 2013, in the vicinity of Laurie Island, where the permanent Argentine Antarctic base Orcadas is located (Figure 1).

Table 1. Seismic events of Mw>6.6 from 1970 to 2021. Date, magnitude and location. Information from the USGS and INPRES.

N°	Year	Month	Day	TIME (UT)	Latitude (°)	Longitude (°)	Depth (km)	Mag (MW)	Region
1	1970	6	15	11:14:51	-54.476	-64.499	10	7.2	Tierra del Fuego, Argentina region
2	1971	2	8	21:04:20	-63.398	-61.377	13	7	South Shetland Islands
3	1973	10	6	15:07:37	-60.823	-21.549	33	7	East of the South Sandwich Islands
4	1977	8	26	19:50:01	-59.426	-20.508	33	7.1	East of the South Sandwich Islands
5	1983	10	22	04:21:35	-60.665	-25.451	24	7.2	South Sandwich Islands region
6	1987	1	30	22:29:42	-60.063	-26.916	48	7	South Sandwich Islands region
7	1991	12	27	04:05:58	-56.032	-25.266	10	7.2	South Sandwich Islands region
8	2003	8	4	04:37:20	-60.532	-43.411	10	7.6	Scotia Sea
9	2006	8	20	03:41:48	-61.029	-34.371	13	7	Scotia Sea
10	2006	1	2	06:10:49	-60.957	-21.606	13	7.4	East of the South Sandwich Islands
11	2008	6	30	06:17:43	-58.227	-22.099	8	7	South Sandwich Islands region
12	2013	11	25	06:27:33	-53.9451	-55.0033	12	7	Malvinas Islands region
13	2013	7	15	14:03:39	-60.857	-25.07	11	7.3	218 km SSE of Bristol Island, South Sandwich Islands
14	2013	11	17	09:04:55	-60.2738	-46.4011	10	7.7	Scotia Sea
15	2014	6	29	07:52:50	-55.4703	-28.3956	8	6.9	154 km NNW of Visokoi Island
16	2016	5	28	09:46:59	-56.2409	-26.9353	78	7.2	53 km NNE of Visokoi Island, South Sandwich Islands
17	2016	8	19	07:32:22	-55.2852	-31.8766	10	7.4	South Georgia Island region
18	2018	12	11	02:26:29	-58.5446	-26.3856	133	7.1	54 km N of Bristol Island, South Sandwich Islands
19	2019	8	27	23:55:19	-60.2152	-26.5801	12	6.6	131 km S of Bristol Island, South Sandwich Islands
20	2021	1	23	23:36:50	-61.8117	-55.4903	10	6.9	South Shetland Islands
21	2021	8	22	21:33:20	-60.2897	-24.8801	14	7.1	South Sandwich Islands region
22	2021	8	12	18:32:52	-57.5674	-25.0316	47	7.5	South Sandwich Islands region
23	2021	8	12	18:35:20	-58.4513	-25.327	56	8.1	South Sandwich Islands region

The water level observed at a tide station results from the combination of the mean level, astronomical tide, storm surge and, on some occasions, additional effects, such as seiches, meteotsunamis and tsunamis. The simultaneous action of these factors or some of them is rare. Nevertheless, there are more susceptible regions where values that are not extreme may affect the shores, causing flash flooding.

The astronomical tide amplitudes in the continental shelf of the Southwestern Atlantic are some of the greatest in the world, reaching 12 m south of the province of Santa Cruz and falling to 5.45 m in Puerto Deseado, 3.91 m in Puerto Madryn, and 1.74 m in Mar del Plata (Argentine Naval Hydrographic Service, 2022). The storm surge amplitude also varies considerably in the area under study. The maximum values of these phenomena are usually below 0.50 m at King Edward Point, Base Prat and O'Higgins, and below 0.80 m at Puerto Williams, Ushuaia and Puerto Argentino. In addition, storm surges are not usually above 1.30 m in Puerto Deseado or Mar del Plata, or 1.5 m in Puerto Madryn. The various combinations of tides and storm surges, together with other phenomena in the area under study, may lead a potential tsunami spreading in the area, even one with small amplitude, to have a significant effect on one region, but not on another. Thus, it is necessary to analyze sea levels at the different tide stations.

Data

This study compiled GMF data from observatories of the International Real-time Magnetic Observatory Network (INTERMAGNET), AP data at sea level from the Global Modeling and Assimilation Office (GMAO) published in the database MERRA-2 (Rienecker *et al.*, 2021), WL records from tide stations of the Intergovernmental Oceanographic Commission (IOC) (Flanders Marine Institute, 2021) and information about $M_w > 6.6$ earthquakes from the United States Geological Service (USGS) and the Argentine Institute of Seismic Forecasting (INPRES) in the area under study of the South Atlantic on the earthquake occurrence dates in Universal Time (UT).

The observatories selected from the INTERMAGNET network in the area were King Edward Point (KEP) (54.3° S; 36.5° W), Puerto Argentino/Port Stanley (PST) (51.7° S; 57.8° W), Orcadas Islands (ORC) (60.7° S; 44.7° W) and Faraday Islands Argentine Island- Akademik Vernadsky Base (AIA) (65.25° S; 64.25° W), whose data are available at **https://intermagnet.github.io**. These observatories provide information about GMF components per minute. The observatories report the components of the horizontal plane (X and Y) and the vertical axis (Z), as well as Declination (D) and Horizontal component (H). The INTERMAGNET network has GMF data in the area since 2003, that is why, from that year, 16 $M_w > 6.6$ seismic events were chosen.

In addition, geomagnetic activities indices Dst (Disturbance Storm Time) and AE (Auroral Electrojet) were considered for the purposes of disregarding observations due to rapid geomagnetic variations caused by solar activity. Dst monitors magnetic variations due to an increased ring current, measured in nT. AE represents the global activity of electrojets in the auroral zone, measured in nT (Davis and Sugiura, 1966). These indices are available at the World Data Center for Geomagnetism, Kyoto (WDC for Geomag.) (**http://wdc.kugi.kyoto-u.ac.jp/wdc/Sec3.html)**.

In addition, so as to compare the solar activity cycles with the biggest earthquakes in the 1970s, the analysis included the sunspot number, available at WDC-SILSO, Royal Observatory of Belgium, Brussels (**http://www.sidc.be/SILSO/)**.

Table 2. Stations with available WL data on the earthquake date, and type of sensor recording the data (Pressure: P; Radar: R; Floating: F; Acoustic: A).

Date	Depth (km)	Mag (Mw)	KE	PA	BP	OH	PW	US	PD	PM	MP
2003/08/04	8	7	-	R	-	-	P	-	-	-	-
2013/07/15	11	7.3	P	R	P	-	P	-	-	P	F
2013/11/17	10	7.7	P	R	P	-	P	-	F	P	R
2013/11/25	11.8	7	P	R	P	-	P	-	F	P	R
2016/05/28	78	7.2	P	P	P	-	P	R	F	P	R
2016/08/19	10	7.4	P	P	P	-	P	R	F	P	R
2018/12/11	133	7.1	P	-	P	-	P	R	F	P	F
2021/08/12	47	7.5	P	P	P	P	P	R	F	P	F
2021/08/12	55.7	8.1	P	P	P	P	P	R	F	P	F
2021/08/12	47.2	7.5	P	P	P	P	P	R	F	P	F
2021/08/22	14	7.1	P	P	P	P	P	R	F	P	F

WL information was obtained from tide stations King Edward (KE) (54.28° S; 36.5° W), Puerto Argentino (PA) (51.75° S; 57.93° W), Base Prat (BP) (62.48° S; 59.66° W), O'Higgins (OH) (63.32° S; 57.90° W), Puerto Williams (PW) (54.93° S; 67.61° W), Ushuaia (US) (54.82° S; 68.22° W), Puerto Deseado (PD) (47.75° S; 65.91° W), Puerto Madryn (PM) (42.76° S; 65.03° W) and Mar del Plata (MP) (38.00° S; 57.54° W), shown on Figure 1, provided by the Sea Level Station Monitoring Facility (**https://www.ioc-sealevelmonitoring.org/**). These observatories provide information about WL per minute. Table 2 shows the stations with available WL records and the sensor used.

Sea-level AP in grids and time series from global data (Rienecker *et al.*, 2021) are obtained from the MERRA-2 database (Modern-Era Retrospective analysis for Research and Applications, Version 2) of NASA's Global Modeling and Assimilation Office (GMAO). This database draws on models of multiple data sets using a fixed assimilation system, and provides data about atmosphere, earth and ocean conditions since 1980, with a spatial resolution of 0.5° × 0.667° (approximately 50 km × 50 km) and a time resolution of 1 hour (**https://gmao.gsfc.nasa.gov/reanalysis/MERRA-2/**)

The characteristics of the earthquakes, such as date, time, magnitude, location, and depth, among others, are available at USGS (**https://earthquake.usgs.gov/earthquakes/**) and INPRES (**https://www.inpres.gob.ar/**) (Table 1).

Methodology

Treatment of the magnetic field data

With the aim of finding patterns in the behavior of the solar magnetic activity and the detection of $M_w \geq 6.6$ earthquakes, the smoothed curve of the daily sunspot number average of the solar cycles between 1970 and 2021, from the end of cycle 20 to the beginning of 25, was contrasted to the occurrence of seismic events (Figure 2).

To obtain the GMF component without secular variation, the GMF horizontal component from the International Geomagnetic Reference Frame (IGRF), **https://www.ngdc.noaa.gov/geomag/**), calculated based on the date and location of each observatory, was subtracted, as per (1).

$$H_{OBS.} = H_{OBS.INTER} - H_{IGRF} \quad (1)$$

where:

H_{OBS} is the GMF horizontal component of the Observatory without secular variation.

$H_{OBS.INTER}$ is the GMF horizontal component measured at each observatory from the INTERMAGNET network.

H_{IGRF} is the GMF horizontal component corresponding to the IGRF.

In addition, the data from observatories, taken in pairs, were deducted from each other, considering the proximity of the earthquake to the network observatory so that the farthest observatory could play the role of a Base Station (H_{Base}) and the closest one that of a field observation point ($H_{Closest}$) according to Larocca *et al.* (2021). Therefore, the differences calculated, referred to as deltas (ΔH), minimized the solar diurnal variation effects, as per (2).

$$\Delta H = H_{Base} - H_{Closest} \quad (2)$$

where: ΔH is the GMF without diurnal variation.

H_{Base} is the GMF horizontal component of the farthest observatory.

$H_{Closest}$ is the GMF horizontal component of the closest observatory.

As the time series of geomagnetic data are non-seasonal and linear, it is appropriate to perform the analysis with adequate methods, such as the continuous wavelet transform (CWT), which, within the mathematical field of harmonic analysis, provides an optimum resolution in the time-frequency plane, thus allowing for an excellent characterization of the series (Grinsted *et al.*, 2004). To this effect, the CWT was applied to the ΔH of the magnetic field at observatories, using the Morlet wavelet (con $\omega_0 = 6$) because it provides an adequate balance between time and frequency location. In addition, the solar activity was assessed based on the hourly values of the Dst and AE indices so as to identify geomagnetic storms (Gulyaeva, 2014) on the earthquake occurrence date as they can mask ΔH.

Moreover, a high-pass filter (*HPF*) with a cut-off frequency of 4 mHz was applied to the ΔH, up to 5 hours before and after the earthquake, for the purposes of identifying anomalous frequencies before the earthquake in the GMF, thus yielding the *F* ΔH.

Treatment of sea-level AP variation levels

For the purposes of detecting AP behavior patterns around a seismic event, the time evolution of the sea-level pressure was calculated, taking the mean value of pixels around the earthquake epicenter. Arai *et al.* (2011) observed that, around the earthquake detection time, the pressure drops and subsequently increases rapidly.

A space-time analysis was conducted in the area to study the sea-level AP behavior. Data were downloaded into a 4º×4º grid one or two hours before and after the earthquake. As the MERRA-2 database provides hourly information, the closest hour was rounded off. For each event, two raster-format grids were obtained. The difference between both grids was calculated, subtracting AP data before and after the earthquake. Table 3 shows the period and magnitude of this variation for each event analyzed.

Table 3. Details of the date and time of the earthquakes studied, before and after time from the MERRA-2 database grid and difference in atmospheric pressure at the location of each earthquake.

Date and time of the earthquake	Time of AP_1 (before the earthquake) (UT)	Time of AP_2 (post-earthquake) (UT)	Atmospheric pressure difference $\Delta AP = AP_2 - AP_1$ [hPa]
2003/08/04; 4:37	4:00	5:00	3.40
2006/01/02; 6:10	5:00	7:00	-0.58
2006/08/20; 3:41	2:00	4:00	-0.20
2008/06/30; 6:17	5:00	7:00	3.48
2013/07/15; 14:03	13:00	15:00	-1.80
2013/11/17; 9:04	8:00	10:00	1.65
2013/11/25; 6:27	6:00	7:00	1.04
2014/06/29; 7:52	7:00	9:00	0.65
2016/05/28; 9:46	9:00	11:00	1.77
2016/08/19; 7:32	6:00	9:00	0.85
2018/12/11; 2:26	2:00	3:00	-0.75
2019/08/27; 23:55	23:00	2:00	1.36
2021/01/23; 23:36	23:00	24:00	-0.013
2021/08/12; 18:32	18:00	19:00	-0.02
2021/08/12; 18:36	18:00	19:00	-0.3
2021/08/22; 21:33	21:00	20:02	0.7

Treatment of WL data

WL information from available sensors was downloaded for each event, and their quality was controlled using the methodology applied for the network of tide stations of the Argentine Naval Hydrographic Service (Banegas *et al.* 2021). Harmonic analyses were performed following the methodology applied by Oreiro *et al.* (2014) for the sites where harmonic constants were not available (BP, BW, OH, KP) using series with, at least, 2-year observations. Only waves with amplitudes over 5 mm were selected. For all stations, astronomical tide predictions were made 10 days before and 10 days after the moment when each earthquake occurred. The levels observed were subtracted from the predictions, yielding the residue, which was subsequently plotted for each event, for all the stations available. Then, it was sought to identify the effect of the tsunami on each station, so as to keep track of the signal, and maximum amplitudes associated with the event were analyzed.

Results

Overlapping the curve of the monthly sunspot number with the occurrence of large magnitude earthquakes from 1970 to 2021 allowed for the identification of a greater number of earthquakes during solar cycle 24 (SC24), approximately between 2010 and 2020. In addition, 65% of the seismic events occurred in periods when the monthly sunspot number was below 100 spots. Also, of a total of 23 earthquakes (Table 1), it was confirmed that 16 occurred in periods of decreased solar activity, while only 7 occurred in increased activity periods. Moreover, only 5 earthquakes coincide with the maximums of the cycles, and 2, with the minimums (Figure 2).

The Scotia and South Sandwich plates have margins of various types with distinguishing tectonic features; however, all of them show great seismic activity. Therefore, this paper was organized presenting studies according to their relative position with respect to the boundaries of the Scotia and Sandwich plates. The GMF, WL and AP results were grouped into three titles for the South Scotia ridge, the South Sandwich Arc and the North Scotia Ridge areas.

South Scotia Ridge

The events on November 17, 2013 (M_w 7.7) and January 23, 2021 (M_w6.9) were selected as representative of the study of the area based on the analysis of GMF variations and geomagnetic activity indices in an interval of ±5 hours from the occurrence of earthquakes.

The continuous wavelet transform for the ΔH observed between the different observatories was performed (Figure 3). The thick black contour lines show a 5% significance level against the red noise background, and the cone of influence (COI) shows the edge effects on the image, which are blurry.

The WT power spectra on the ΔH component from the observatories chosen (Figure 3a and b) during a period of ± 5 hours, centered on the selected earthquake, show high-energy areas in periods of 0.05 h to 0.25 h, between 1 and 3 hours before its occurrence. The spectral analysis

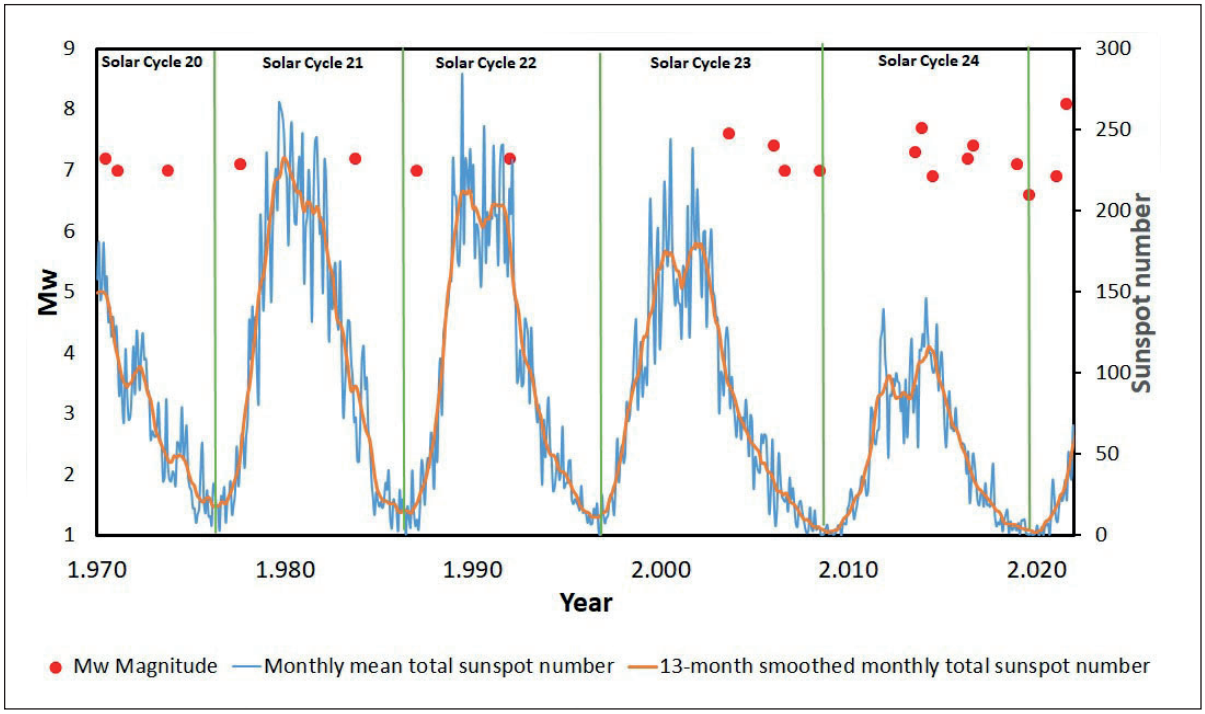

Figure 2. Graph with solar cycles and occurrence of large-magnitude seismic events since the 1970s. Monthly sunspot number (blue line) and smoothed sunspot number (red line). Start/end of solar cycles (SC) 21-25 (vertical grey lines). Earthquakes (red dots).

of the earthquake on November 17, 2013 shows a 2-4 Hz high-energy area (areas surrounded by black lines) in periods between 0.125 and 0.25 h, one hour after the event, in the presence of a solar activity index Dst of -25 nT, suggesting a weak magnetic storm, as confirmed by the AE index value above 280 nT (Figure 3 a).

While the earthquake on January 23, 2021 showed high-energy areas from the moment of the earthquake to 2 hours before and 1 hour after it, covering the entire frequency spectrum 2 hours before its occurrence, on that day the Dst index did not show geomagnetic storms (Figure 3b).

The effect of covering a wide range of frequencies around the earthquake with high energies is repeated before and after the events on August 4, 2003 and August 20, 2006, also located in the area under study, with similar magnitudes and depths.

A cross wavelet correlation (XWT) between the most intense earthquakes (August 4, 2003-November 17, 2013) with M_w7.6 and 7.0, respectively, and the least intense ones (August 20, 2006-January 23, 2021) with M_w7.0 and 6.9, respectively, was calculated separately (Figure 4a and b). The figures were drawn centered on the moment when each earthquake occurred for the purposes of highlighting common frequencies before and after both earthquakes. Both correlations show that 2-hour high-energy periods coincide up to 3 hours before and after the events. In addition, between 1 and 3 hours before and after the zero hour, direct and inverse correlations can be found (Figure 4a and b).

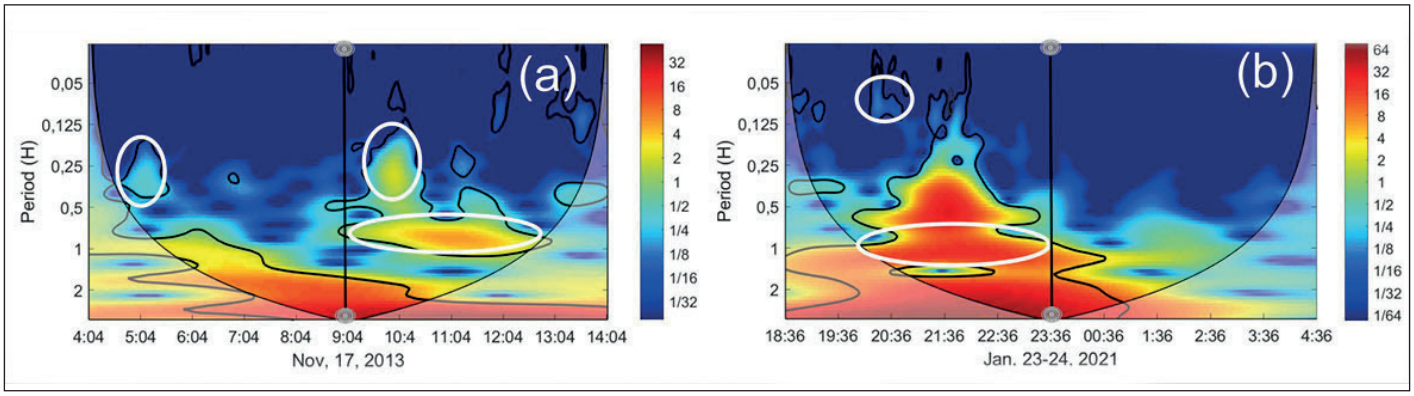

Figure 3. Continuous wavelet transform of ΔH, centered on the moment when the earthquake occurred, with a ± 5 hour range; (a) ΔAIA-ORC: November 17, 2013; (b) ΔAIA-PST: January 23-24, 2021. Earthquake (gray bar).

An HPF with a cutoff wavelength of 4 min was applied to the ΔH among observatories AIA, PST and KEP. The filtering shows oscillations with an amplitude between ±0.5 and 2 nT, occurring between 2 and 6 hours before the event (Figure 5a and b). The filtering of the seismic event on November 17, 2013 shows a significant amplitude for around 7 minutes (Figure 5a), while the event on January 21, 2021 shows the same significant amplitude for 40 minutes (Figure 5a). In both cases, events were preceded by a series of earthquakes (M_w 5.8 to 4.4) for the same length of time.

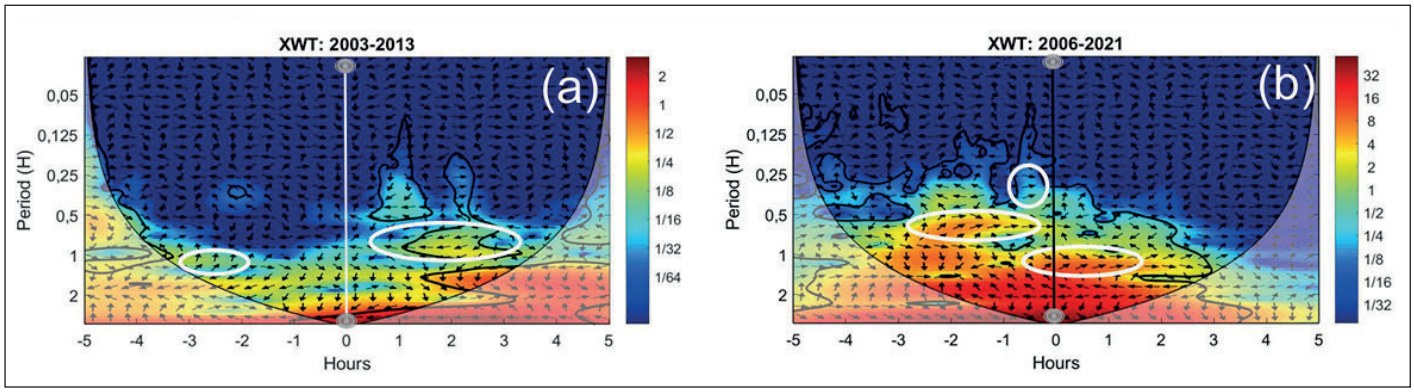

Figure 4. Crossed wavelet correlation (XWT) centered on the earthquake, between events on August 4, 2003 and November 17, 2013 (a); between events on August 20, 2006 and January 23, 2021 (b). High significance level (black curves). Direct and inverse correlation (white ovals). COI edge effects (blurry image).

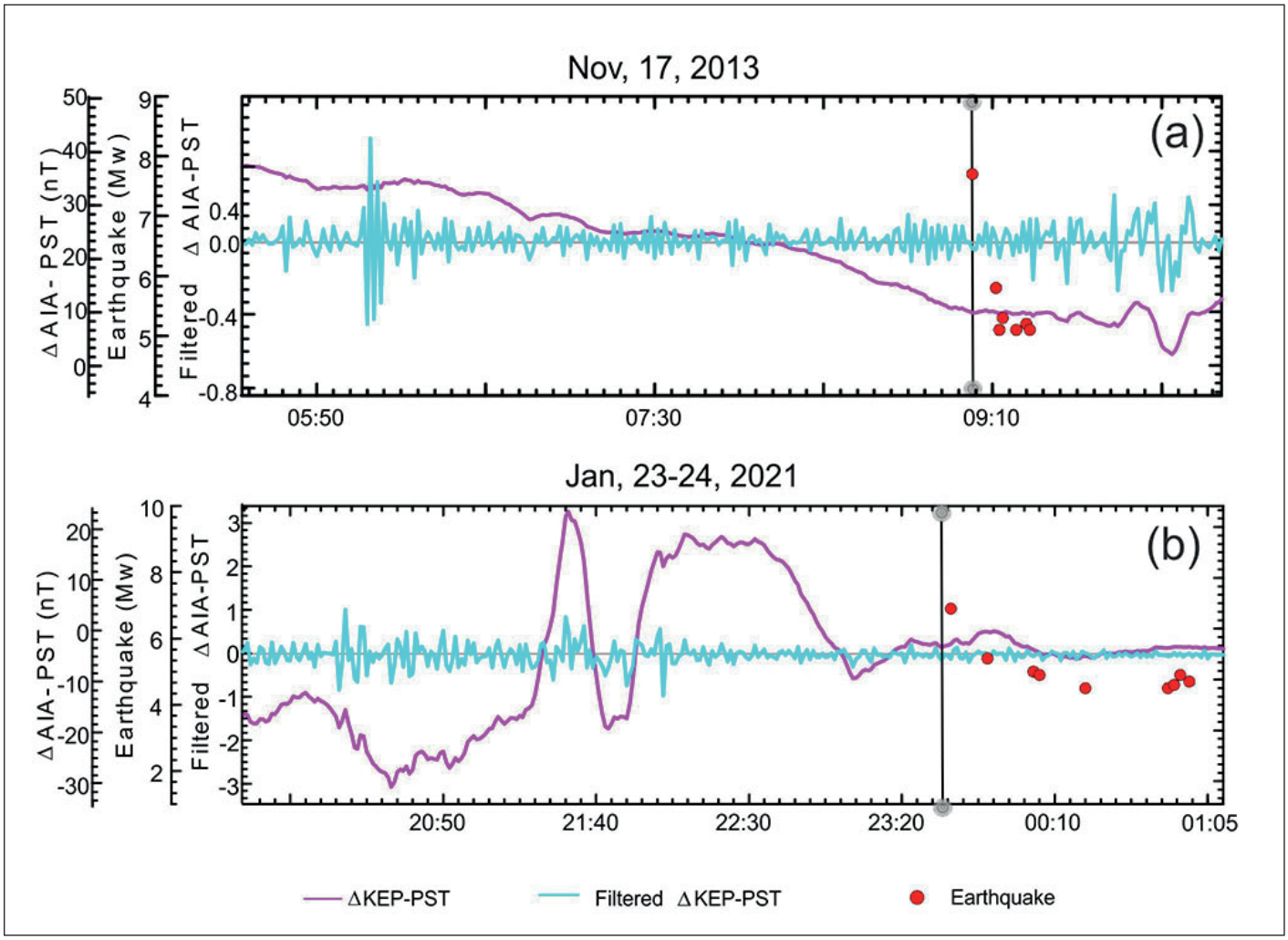

Figure 5. Difference of the H component of the magnetic field between observatories (ΔH) (magenta line). Filtered ΔH (cyan line). Earthquake (red dot). (a) ΔAIA-PST Nov 17, 2013; (b) ΔAIA-PST Jan 23, 2021.

Figure 6 shows the WL measured by the available tide stations on November 17, 2003, when the earthquake occurred (M_w7.7), and 4 days after the event; this is the only $M_w \geq 7$ magnitude event occurring in the area and for which there is available WL information. A disturbance that may be associated with the earthquake is shown, around 2.5 hours after the occurrence of the event at KE, ~930 km away, and a mild disturbance at PD, PM and MP, more than 12 hours later (Figure 6). In all cases, the disturbances show amplitudes in the order of 0.30 m, not posing potential risks, even if combined with storm surge events, like at PM and MP.

Figure 7 shows the results of the space-time analysis of the sea-level pressure variation in this area. For the earthquake on November 17, 2003, between 8:00 and 10:00 (UTC) (Table 3), around the earthquake epicenter (gray bar), an area of disturbance can be seen in the isobars, as well as pressure variation in the time series (Figure 7a and c). The AP difference represented by isobars shows a force field parallel to the transcurrent margin where the tighter lines would suggest greater stress. It is worth pointing out that 7 minutes later, an M_w5.8 earthquake occurred 200 km away from the previous one, aligned parallel to the transcurrent margin, which is why it is associated with the disturbance of isobar lines.

In addition, analyzing the earthquake on January 23, 2021 between 23:00 and 24:00 (UTC) (Table 3), we can see that within one hour from the moment when the event chosen occurred, 7 earthquakes more with magnitudes between M_w5.4 and M_w4.6 are detected. They are distributed in the area forming a wedge, not more than 30 km away from the earthquake under study, following the same pattern as that of isobars, as shown on Figure 7b. Figure 7d shows that the AP maximum occurs in the same time span. After the main earthquake, the AP drops to 0.3 hPa.

South Sandwich Arc

The most representative earthquakes in this area, occurring on June 29, 2014 (M_w6.9) and August 12, 2021 (M_w7.5 and 8.1) were analyzed. Rapid GMF variations and geomagnetic activity indices were studied in an interval of ± 5 hours from the occurrence of the earthquakes.

In addition, the continuous wavelet transform for the ΔH found among observatories KEP, PST and ORC was applied (Figure 8). It is observed that, in the time range centered on the earthquake, there are high-energy areas in periods between 0.125 and 0.50 hours, between 2 and 4 hours before or after the earthquake on June 29, 2014 (M_w6.9) at a depth of only 8 km (Figure 8a).

Meanwhile, Figure 8b shows bunch-like high frequency ranges before and after the events, given that two highly intense earthquakes (M_w7.5 and 8.1) occurred at a great depth (47 and 56 km), separated by 3 minutes and only 90 km away, which does not allow for a clear definition in a frequency range, and, within one hour, more than 5 earthquakes with intensities in the order of M_w5.9 are also added.

A cross correlation between the earthquakes (June 29, 2014-August 12, 2021) was calculated (Figure 9). The figure was drawn centering each earthquake (0 hour) for the purposes of highlighting common frequencies before and after both earthquakes. No areas of high energy significance are shown, probably due to the fact that the correlated earthquakes occurred at very different depths. In spite of that,

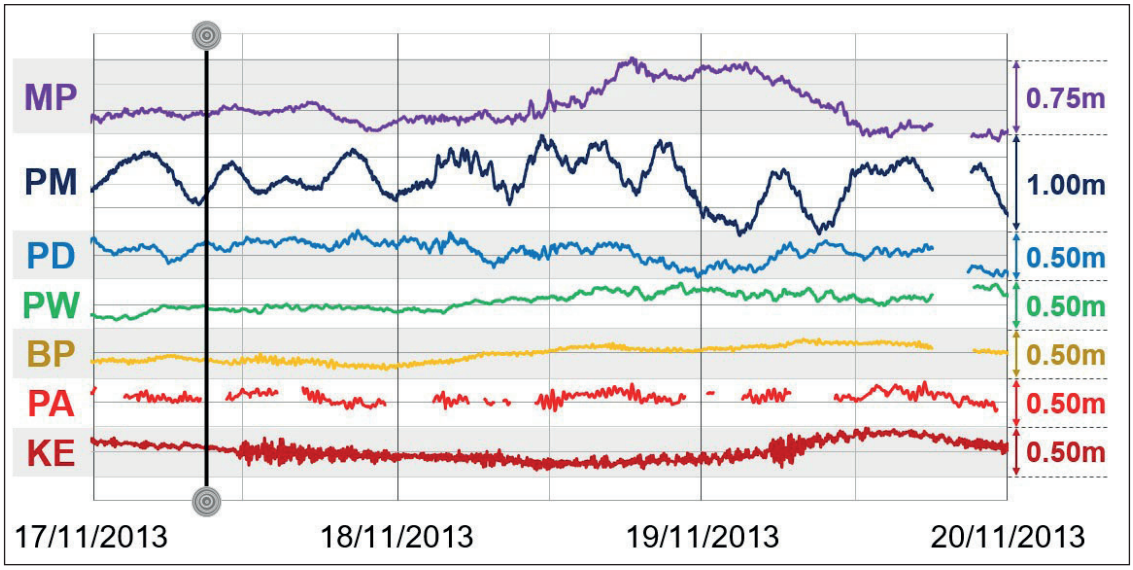

Figure 6. WL measurement from tide stations King Edward (KE), Puerto Argentino (PA), Base Prat (BP), O'Higgins (OH), Puerto Williams (PW), Ushuaia (US), Puerto Deseado (PD), Puerto Madryn (PM) and Mar del Plata (MP), after the earthquake on November 17, 2003 (M_w7.7) at 9:04 (UTC), at a depth of 11.8 km (black vertical line).

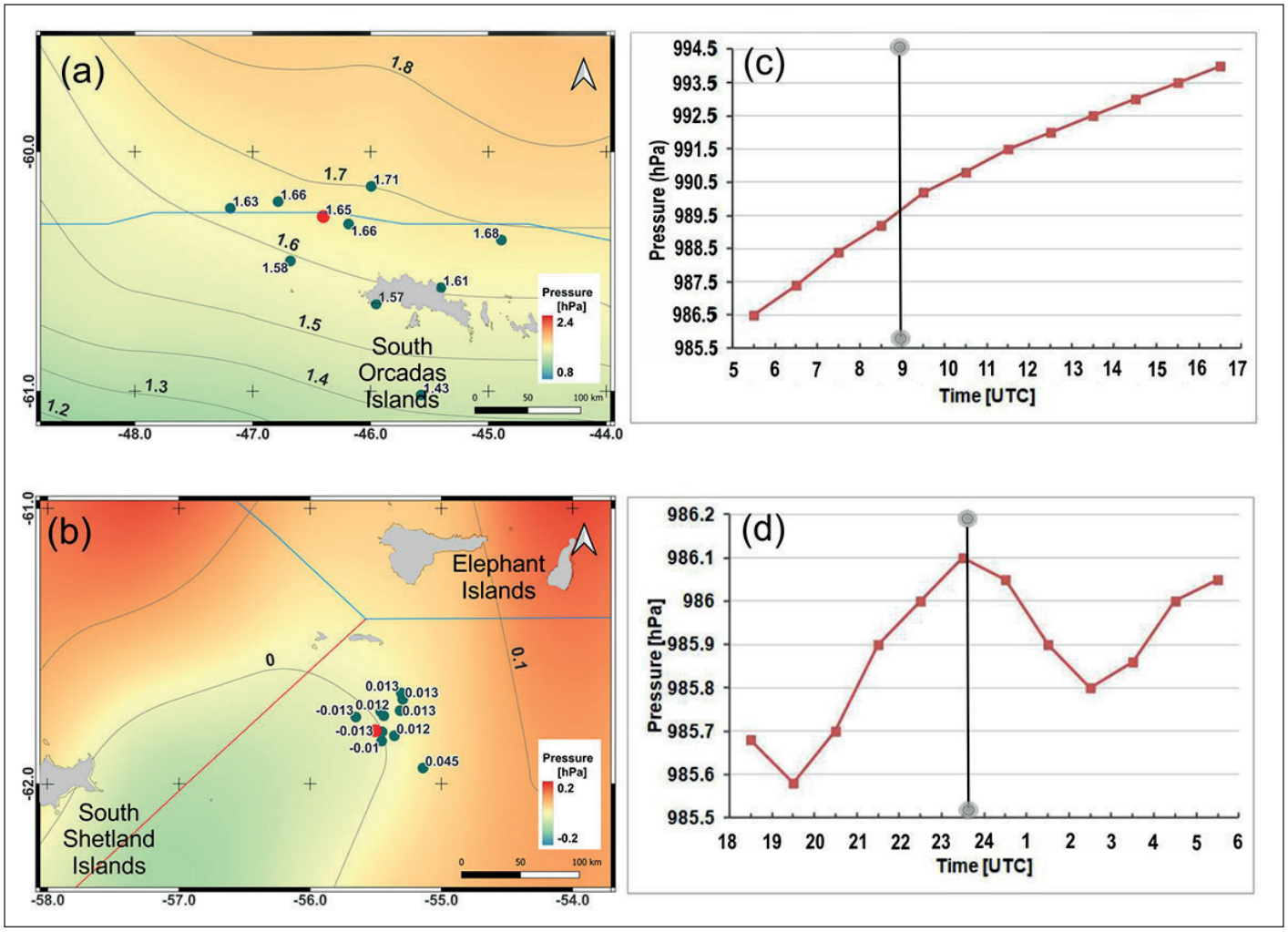

Figure 7. Differences of ocean-level AP grids on: (a) Nov 17, 2013, (8:00 -10:00); (b) Jan 23, 2021, (23:00-24:00). Time series of sea-level hourly AP: (c) Nov 17, 2013 (5:30 - 16:30); (d) Jan 23-24, 2021 (18:30 - 5:30). Plate margins: divergent margin (red line); transcurrent margin (blue line). Earthquakes: position according to the coordinates of their epicenter (left) (red dots). Local difference (green dots); time location (right) (gray bar).

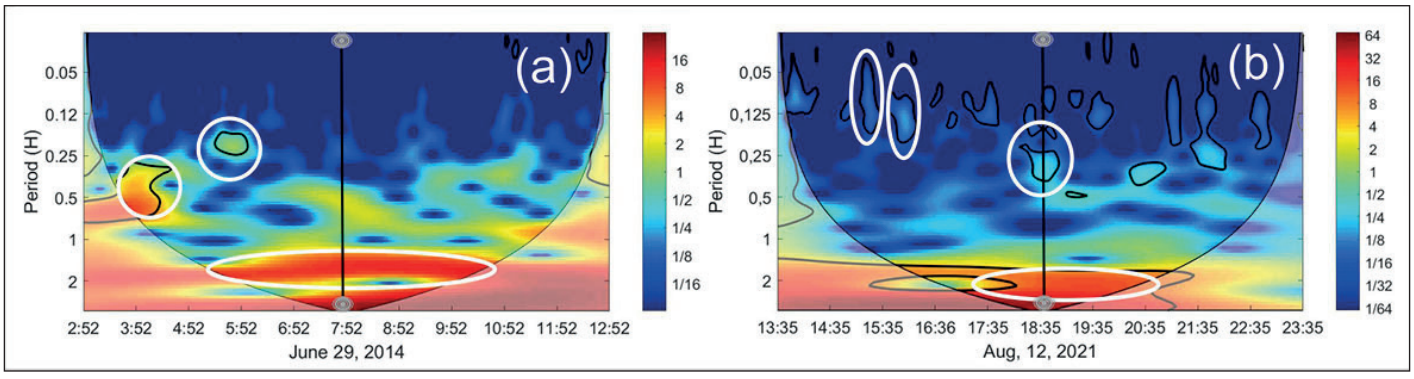

Figure 8. Continuous wavelet transform ΔH, centered on the moment when the earthquake occurred, with a ± 5 hours range; (a) ΔKEP-ORC: June 29, 2014; (b) ΔKEP- PST: August 12, 2021. Earthquake (black bar).

in an interval between 1 and 2 hours before the events, a certain correlation for a period of 1 to 2 hours (medium to high frequencies) can be seen.

An HPF with a cutoff wavelength of 4 min was applied to the ΔH among observatories ORC, PST and KEP. Oscillations with an amplitude between ±0.2 and 0.5 nT, occurring approximately 6 hours before the earthquake on June 29, 2014, are shown (Figure 10a). The filtering shows two periods of significant amplitudes for 10 and 20 minutes, separated by 15 minutes, which are similar to the duration interval of the series of earthquakes occurring with the event on June 29, 2014. The filtering of the earthquakes on August 12, 2021 shows maximum oscillations of ± 0.2 nT, 2.5 hours before and for a period of 1.5 hours before the occurrence of ten earthquakes (M_w 5 to 8.1), which were chained together every 2 to 3 minutes after the first one (M_w 7.5). These results are consistent with the results yielded by the continuous wavelet transform (Figure 10b).

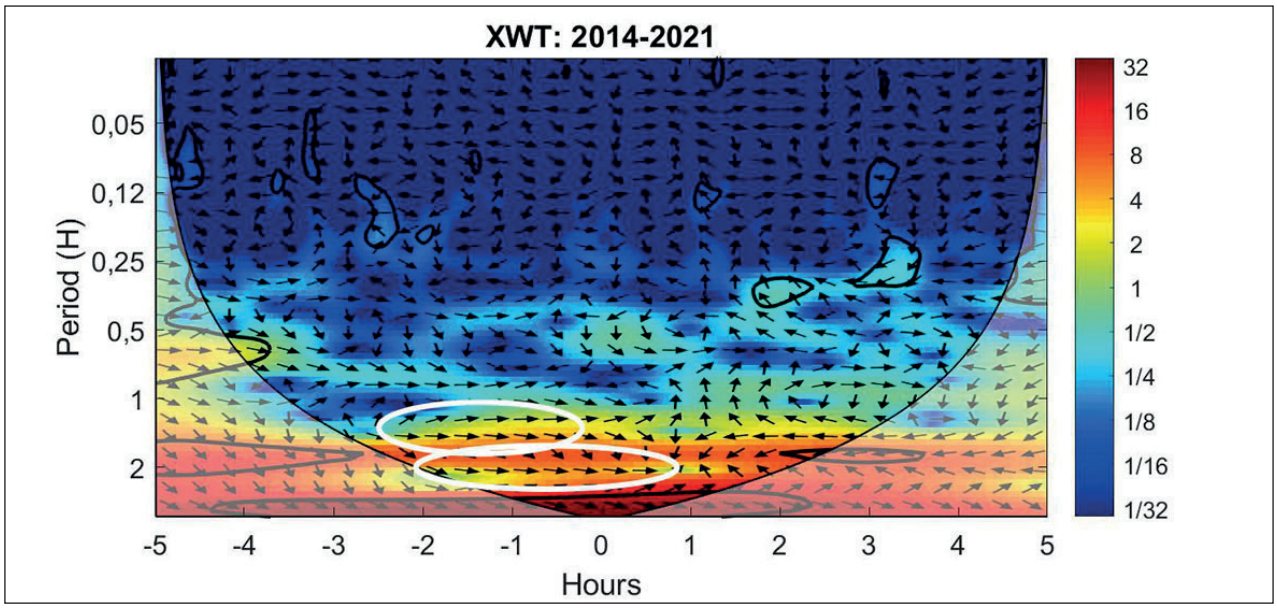

Figure 9. Crossed wavelet correlation (XWT) centered on the earthquake, between the events on June 29, 2014 and August 12, 2021. High significance level (black curves). Direct correlation (white ovals). COI edge effects (blurry image).

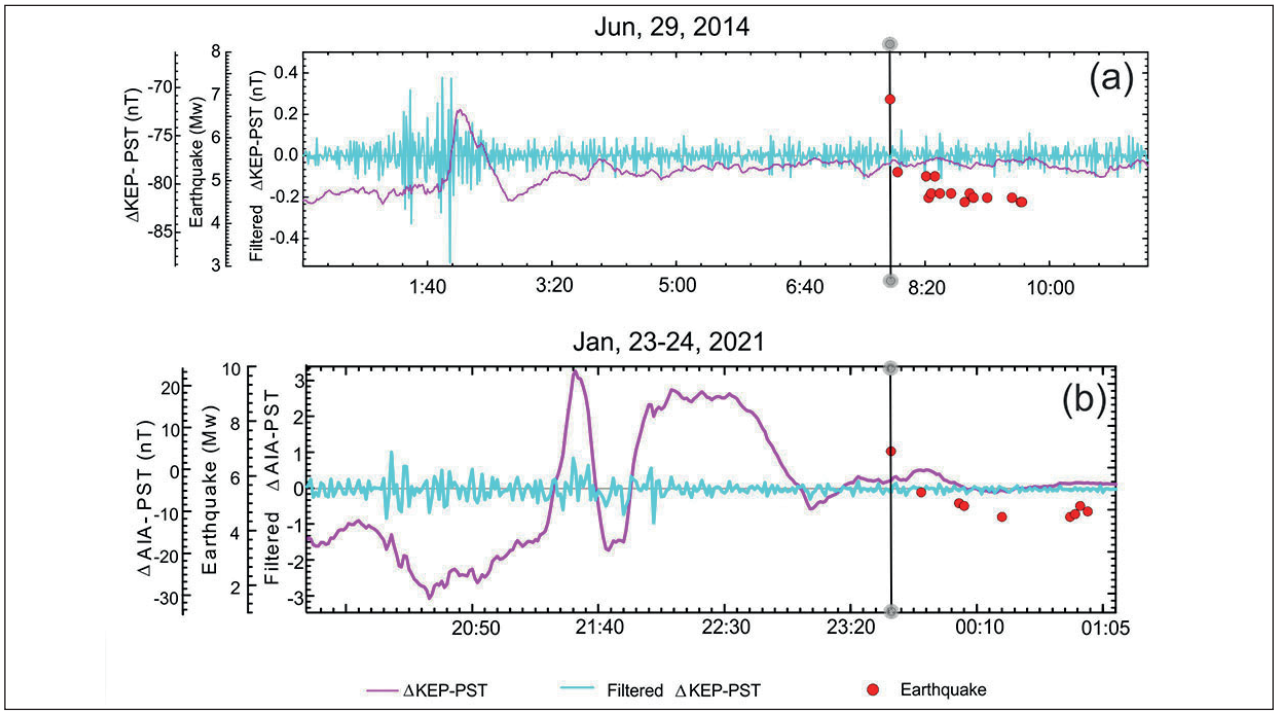

Figure10. Difference of the H component of the magnetic field between observatories (ΔH) (magenta line). Filtered ΔH (cyan line). Earthquake (red dot). (a) ΔKEP-PST June 29, 2014; (b) ΔKEP-PST August 12, 2021.

Unlike in the South Scotia Ridge area, in this region there is WL information available for 6 $M_w \geq 7$ events, of which only those occurring on December 11, 2018 (M_w7.1) and August 12, 2021 (M_w8.1) are shown (Figures 11a and b).

In the events occurring on June 30, 2008 (M_w7.0), July 15, 2013 (M_w7.3), May 28, 2016 (M_w 7.2) and August 22, 2021 (M_w7.1), the effect of the earthquake on the WL is not clearly identified, except for, in some cases, small variations below 0.10 m, which may suggest its occurrence, but are not conclusive as they may be due to other phenomena.

The duration of the water surface disturbance may be identified with greater amplitudes at the stations, without exceeding, in any case, two days from the occurrence of the earthquake on December 11, 2018 780 km away from KE and 1900 km away from BP (Figure 11a). By contrast, the event occurring on August 12, 2021 does allow for the clear identification of the earthquake effect on the WL variation in nearly all the stations analyzed, and the time of arrival of the tsunami at each station can also be calculated. The tsunami amplitudes vary according to the station analyzed, from values around 1.3 m at KE to values around 0.10 m at PM or MP (Figure 11b).

Figure 12 shows the space-time analysis of the sea-level pressure behavior in the area of the convergent margin on June 29, 2014, between 7:00 and 9:00 (UTC), and on August 12, 2021, between 18:00 and 19:00 (UTC). Around the

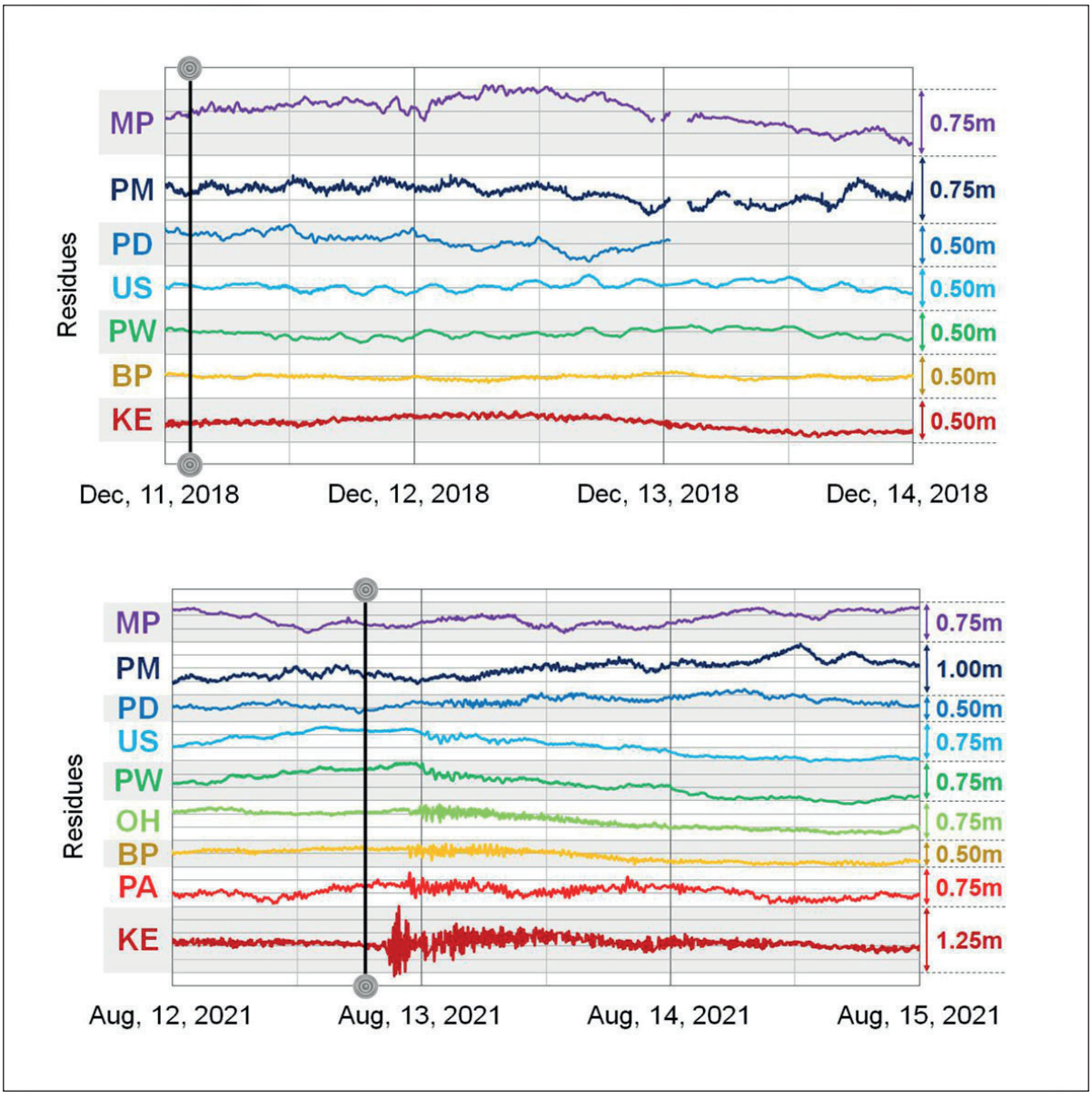

Figure 11. WL measurement from tide stations King Edward (KE), Puerto Argentino (PA), Base Prat (BP), O'Higgins (OH), Puerto Williams (PW), Ushuaia (US), Puerto Deseado (PD), Puerto Madryn (PM) and Mar del Plata (MP): (a) after the earthquake on December 11, 2018 (M_w7.1) at 02:26 (UTC), at a depth of 133 km; (b) after the earthquakes of August 12, 2021 (M_w7.5 and M_w8.1) at 18:32-18:35 (UTC), at a depth of 47 and 55 km, respectively. Event (black vertical line).

earthquake epicenter (gray bar), an area of disturbance in the isobars and pressure variation in the time series can be seen. Throughout the area, the isobar pattern is not uniform. Table 3 shows the period and magnitude of this variation for each event analyzed.

Figure 12a shows a non-uniform isobar distribution pattern, coinciding with great seismic activity due to the occurrence of 7 earthquakes (between M_w4.4 and 6.6) in a period not longer than one hour within 50 km from the area studied. It is a set of superficial earthquakes occurring at a depth of 8-10 km.

In addition, the pressure variation at the earthquake epicenter is altered when it increases (Figure 12c). Figure 12b shows an irregular isobar distribution pattern associated with the M_w7.5 and M_w 8.1 earthquakes resulting from a reverse fault sharply dipping northwestwards in the subduction area of the Scotia Arc, at a depth of ~56 km and 47 km, respectively. The earthquakes occurred with a difference of 3 minutes and at a distance of ~90 km. It should be noted that, within 30 minutes after 18:32, there was a series of earthquakes with a considerable magnitude aligned to the convergent margin that may have caused the pressure to drop from 18:30 to 21:30 (Figure 12d).

North Scotia Ridge

In this area, two earthquakes occurred on November 25, 2013 (M_w7.0) and on August 19, 2016 (M_w 7.4) at a depth of 11.8 and 10 km, respectively. The former was considered as a significant earthquake by the USGS.

We observed that the earthquakes on November 25, 2013, close to Malvinas (PST), and on August 19, 2016, close to KEP, even though they occurred at the same depth (~10 km)

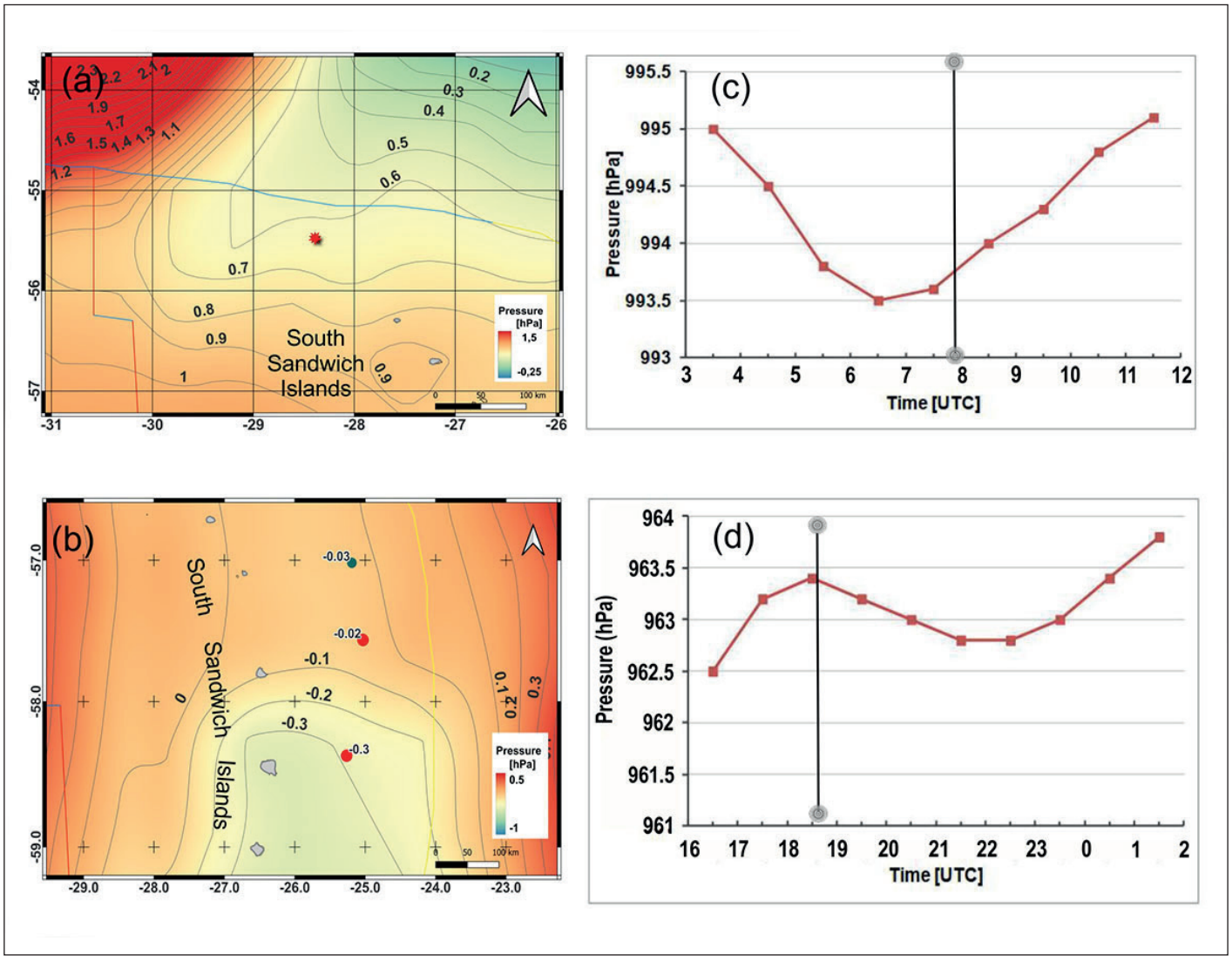

Figure 12. Differences of ocean-level AP grids on: (a) June 29, 2014 (7:00-9:00); (b) August 12, 2021 (18:00-19:00). Time series of sea-level hourly AP: (c) June 29, 2014 (3:30-11:30); (d) August 12-13, 2021 (16:30-1:30). Plate margins: divergent margin (red line): convergent margin (yellow line); transcurrent margin (blue line). Earthquakes: position according to the coordinates of their epicenter (left) (red dots). Local difference (green dots); time location (right) (gray bar).

and on the same type of margin, do not show common frequencies in the wavelet analysis. Because of this, no results can be obtained from the cross correlation.

The HPF does not allow for the identification of anomalous oscillations before the earthquake on November 25, 2013. Nevertheless, for the earthquake on August 19, 2016, the filter shows oscillations of ± 0.4 nT to 0.2 nT, around 3 hours before its occurrence, separated by 30 minutes in a consistent manner with a period of 22 minutes separating the 5 earthquakes that occurred after the earthquake studied (Figure 13).

In the North Scotia Ridge area, there are WL recordings for only 2 $M_w \geq 7$ events on November 25, 2013 (M_w7) and on August 19, 2016 (M_w7.4), which are shown on Figure 14. The WL behavior at the stations analyzed does not allow for a clear identification of the effect of either earthquake, except for KE, where a small disturbance below ±0.30 m about 8 hours and 30 minutes later, 1200 km and 290 km away, respectively, could be attributed (Figure 14a and b). The behavior in this area is similar to the one observed in the previous ones for earthquakes with similar magnitudes, not posing a risk for coastal populations.

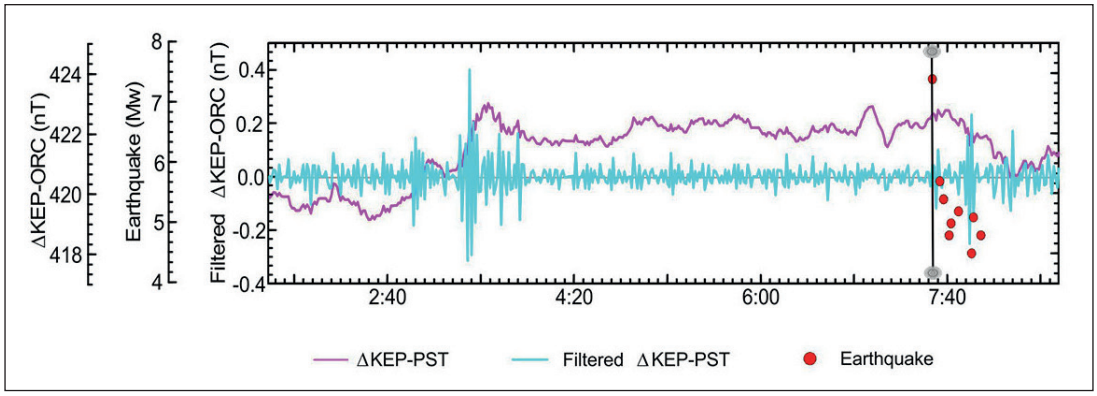

Figure 13. Difference of the H component of the magnetic field between observatories (ΔH) (magenta line). Filtered ΔH (cyan line). Earthquake (red dot). For ΔKEP- ORC: August 19, 2016.

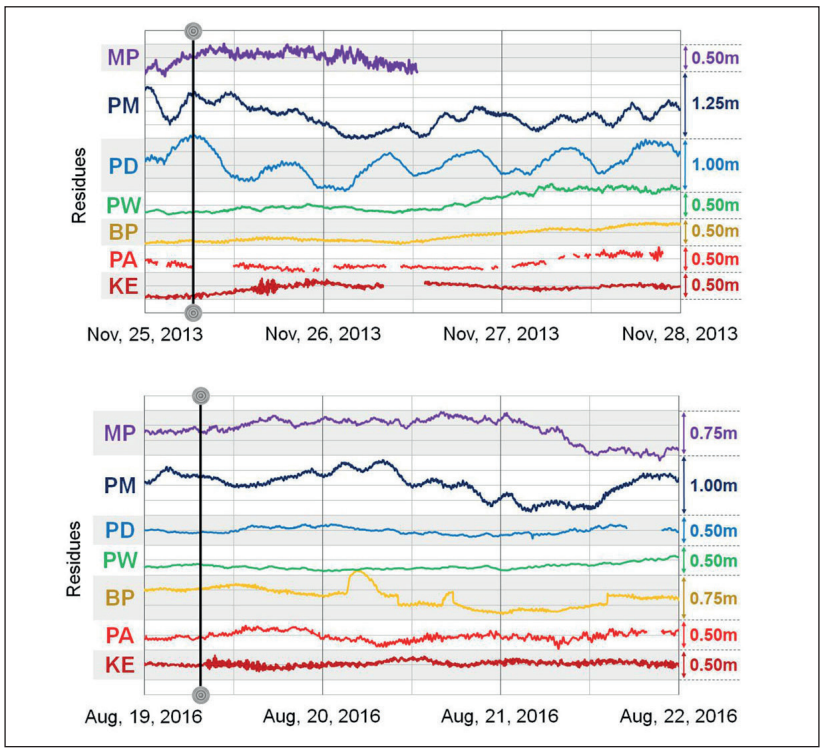

Figure 14. WL measurement from tide stations King Edward (KE), Puerto Argentino (PA), Base Prat (BP), O'Higgins (OH), Puerto Williams (PW), Ushuaia (US), Puerto Deseado (PD), Puerto Madryn (PM) and Mar del Plata (MP): (a) after the earthquake on Nov 25, 2013 (M_w 7) at 6:27 (UTC) at a depth of 11.8 km; (b) after the earthquake on August 19, 2016 (M_w7.4) at 7:32 (UTC), at a depth of 10 km. Event (black vertical line).

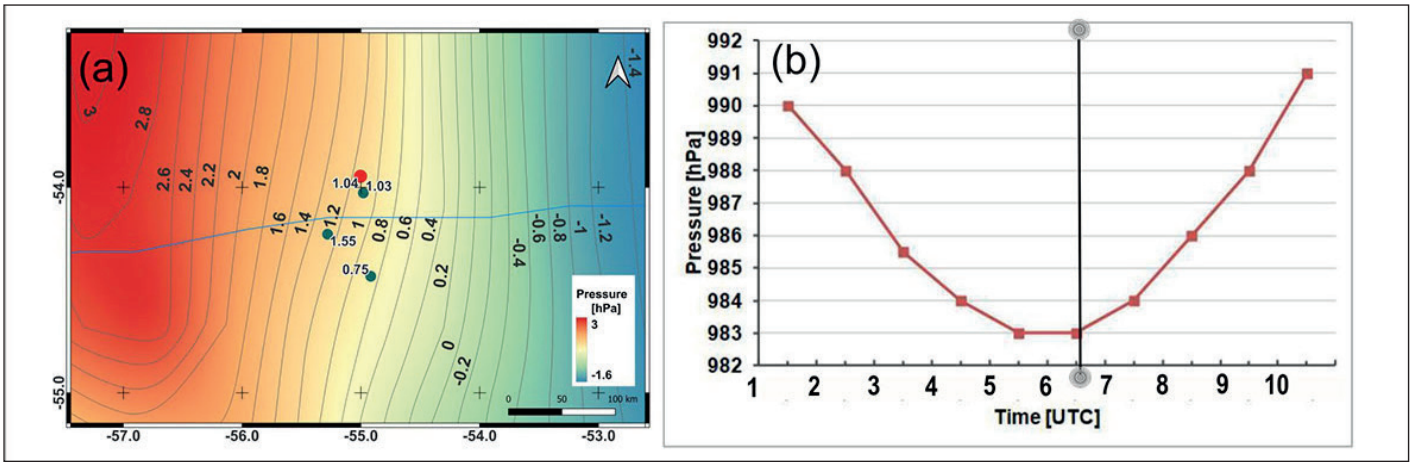

Figure 15. Differences of ocean-level AP grids on: (a) November 25, 2013 (5:00-7:00). Time series of sea-level hourly AP: (b) November 25, 2013 (1:30-10:00). Plate margins: transcurrent margin (blue line). Earthquakes: position according to the coordinates of their epicenter (left) (red dot). Local difference (green dots); time location (right) (gray bar).

Figure 15 shows the results of the space-time analysis of the sea-level pressure behavior in this area for the event on November 25, 2013 between 5:00 and 7:00 (UTC). A behavior pattern that appears to be different from the previous ones can be distinguished with regard to the transcurrent margin. Nevertheless, around the earthquake epicenter, an area of disturbance in isobars and pressure variation in the time series can be seen. This behavior can be seen in the grid (Figure 15a) by means of the concave curvature towards the location of the M_w7 earthquake, which is consistent with the fault strike (SSW) evidenced by the alignment of five earthquakes (from M_w 4.9 to 5.6) occurring in a period of 10 minutes after the earthquake under study (Figure 15a). In addition, the time pressure recording, measured at the location of the earthquake (1:30 – 10:06), shows a change in tendency. While some hours before the event the pressure tends to drop, some hours later it increases. Table 3 shows the period and magnitude of this variation for each event analyzed.

Study of medium and low GMF frequencies

It was found that 70% of the ΔH analyzed 24 hours before and after the earthquakes studied showed medium to low frequencies with an anticipation of 12 to 4 hours, while only 10% showed an anticipation in a range below 4 hours, and 20% did not show any frequency whatsoever. In some cases, an alteration in low to medium frequencies could be found after their occurrence; 20% in a range of 0 to 4 hours and 30% in a range of 4 to 12 hours. No typical frequencies could be observed after the earthquakes in 50%. Table 4 displays the data recorded.

Table 4. Compilation of frequencies from the Continuous Wavelet Transform analysis before and after the earthquakes on disturbed days.

Date and time	Frequencies (Hz)	Depth (km)	Mag (M_w)	Disturbed day	Anticipation period (hs)	Delay period (hs)
2003/08/04; 4:37	0.004 to 0.26	10	7.6	No	6	8
2006/01/02; 6:10	0.004 to 0.03	13	7.4	No	6	No
2006/08/20; 3:41		13	7	No	0-12	0-12
2008/06/30; 6:17	0.004 to 0.266	8	7	No	0-8	0-8
2013/07/15; 14:03		11	7.3	No	0-4	0-4
2013/11/17; 9:04		10	7.7	No	3-4	3-4
2013/11/25; 6:27	0.001 to 0.002	11.8	7	No	No	No
2014/06/29; 7:52		8	6.9	No	4-5	No
2016/05/28; 9:46		78	7.2	No	4-8	8
2016/08/19; 7:32	0.004 to 0.033	10	7.4	No	No	No
2018/12/11; 2:26		133	7.1	Yes	No	No
2019/08/27; 23:55		11.8	6.6	No	1-2	1-2
2021/01/23; 23:36		9.8	6.9	No	3-7	No
2021/08/12; 18:32		55.7	7.5	No	1-2	1-2
2021/08/12; 18:36	0.004 to 0.033	14	8.1	No	1-2	1-2
2021/08/22; 21:33		47.2	7.1	No	6	No

Conclusions

It is possible to distinguish different responses of the GMF, WL and AP according to the type of margin where the seismic event occurs.

It is possible to detect anomalous variations in geomagnetic field records in spans from 1 to 12 hours before and after the manifestation of seismic events with a magnitude above M_w6.6. By means of a high-pass filter, anomalous peaks with amplitudes of up to ±0.4nT were recognized on the geomagnetic signals of ΔH with an anticipation of up to 6 hours and durations compatible with the results of the continuous wavelet transform and the series of earthquakes occurring with the $M_w \geq$ 6.6 earthquake. In the WL residues, amplitudes of up to ±0.3m and compatible arrival times were detected according to the distance from the tide sensor to the earthquake. The isobar distribution pattern was consistent with the fault planes of the earthquakes.

In the South Scotia Ridge, the geomagnetic field showed anomalies in ranges from 3 to 5 hours before the seismic activity. In addition, there were anomalous WL values in the sensors closest to the events with amplitudes of ~ 0.30 m. The cases analyzed do not necessarily represent the behavior of the WL variation of earthquakes occurring in this area, but, as the occurrence frequency and magnitude is one of the most significant in the region, they may be considered as a first indicator of the amplitude expected on nearby shores. Additionally, isobars can have AP anomalies of up to 0.3 hPa at the earthquake epicenter.

In the plate subduction area, the geomagnetic field study did not highlight the greatest magnitude earthquake (M_w8.1) due to a series of earthquakes occurring in less than three minutes, even though it made it possible to observe the typical low frequencies due to the plate friction. In addition, the filters showed even amplitudes during the 5-hour period studied without yielding specific and identifiable frequencies. Similarly, the isobar distribution was very irregular. After the M_w 8.1 earthquake, the WL residues showed disturbances at most stations; only at King Edward amplitudes reached 1.30 m. Although it did not pose a potential risk, even when combined with storm surge events, like in Puerto Madryn and Mar del Plata, and given its significant magnitude, it may be considered as a first indicator of the amplitude expected on nearby shores in the region.

The transcurrent margin of the North Scotia Ridge showed a low response of the geomagnetic field to the presence of seismic activity. Nevertheless, there are anomalous variations in the WL at close tide stations (0.10 m), as well as 0.3 hPa atmospheric pressure variations both in isobars and the time series after the seismic activity. The WL behavior in this area is similar to the behavior of previous ones for earthquakes with similar magnitudes, not posing a risk for coastal populations as long as the same depth characteristics are maintained.

Results vary according to the area under study as the tectonic characteristics of the margins of the Scotia and Sandwich plates yield different results of geomagnetic signals. The selection of earthquakes in three areas with different characteristics leads us to think that results largely depend on their tectonogenesis. They either make it possible to see frequencies or not, based on their particular characteristics. This is worthy of a more thorough and detailed analysis to be addressed in future research.

Moreover, given that one of the magnitudes to study was the GMF that is affected by solar activity, it was proposed to evaluate periods of solar activity, based on the number of sunspots, in comparison with the 23 selected earthquakes, concluding that more than a half of the earthquakes occurred in the period of decrease or minimum of solar activity.

Acknowledgements

We thank the referees for their valuable comments. This study was partly subsidized by projects UNDEFI No. 259/2020 and UBACyT 20020190100236BA.

References

Arai N., Iwakuni M., Watada S., Imanishi Y., Murayama T. and Nogami M., (2011). Atmospheric boundary waves excited by the tsunami generation related to the 2011 great Tohoku-Oki earthquake, *Geophys. Res. Lett., 38*, L00G18. **https://doi.org/10.1029/2011GL049146**.

Ayca, A., & Lynett, P. J., (2016). Effect of tides and source location on nearshore tsunami-induced currents. *Journal of Geophysical Research: Oceans,121*, n8807– 8820. **https://doi.org/10.1002/2016JC012435** 2011GL049146.

Arecco, M.A. Larocca P.A., Mora M.C., (2020). Geomagnetismo y su relación con sismos. Un estudio en la microplaca de Sandwich del Sur, *Revista Defensa Nacional*, v 4, 263-281. **http://www.cefadigital.edu.ar/handle/1847939/1558**.

Banegas L., Grismeyer W.H., Fiore M.M.E., Oreiro F.A., (2021). Actualización de la interfase para la descarga de datos de marea Publicados por la Comisión Oceanográfica Intergubernamental Informe Técnico Nº 04/21. Departamento Oceanografía del Servicio de Hidrografía Naval, 12p.

Beniest A., Schellart W.P., (2020). A geological map of the Scotia Sea area constrained by bathymetry, geological data, geophysical data and seismic tomography models from the deep mantle, Earth-Science Reviews, Volume 210, 103391. **https://doi.org/10.1016/j.earscirev.2020.103391**.

Dalziel I.W.D., Lawver L.A., Norton I.O. and Gahagan L.M., (2013). The Scotia Arc: Genesis, Evolution, Global Significance. *Annual Review of Earth and Planetary Sciences 41:* 767–793. **https://doi.org/10.1146/annurev-earth-050212-124155**.

Dragani, W. C., D'Onofrio, E. E., Grismeyer, W., Fiore, M. M., Violante, R. A., and Rovere, E. I., (2009). Vulnerability of the Atlantic Patagonian

coast to tsunamis generated by submarine earthquakes located in the Scotia Arc region. Some numerical experiments. *Natural hazards, 49*(3), 437-458. **https://doi.org/10.1007/s11069-008-9289-4**.

Eagles G., (2010). The age and origin of the central Scotia Sea. *Geophysical Journal International 183:* 587–600. **https://doi.org/10.1111/j.1365-246X.2010.04781.x**.

Flanders Marine Institute (VLIZ), Intergovernmental Oceanographic Commission (IOC), (2021), *Sea level station monitoring facility.* VLIZ. **https://doi.org/10.14284/482**.

Gao, Y., Chen, X., Hu, H., Wen, J., Tang, J., and Fang, G., (2014), Induced electromagnetic field by seismic waves in Earth's magnetic field, *J. Geophys. Res. Solid Earth*, 119, 5651–5685, doi:10.1002/2014JB010962.

Gulyaeva, T. L., Arikan, F. E. Z. A., & Stanislawska, I. (2014). Probability of occurrence of planetary ionosphere storms associated with the magnetosphere disturbance storm time events. *Advances in Radio Science, 12*, 261-266.

Hayakawa, M., Kasahara, Y., Nakamura T., et al., (2010). A statistical study on the correlation between lower ionospheric perturbations as seen by subionospheric VLF/LF propagation and earthquakes, *Journal of Geophysical Research*, A, vol. 115, no. 9, Article ID A09305. **https://agupubs.onlinelibrary.wiley.com/doi/full/10.1029/2009JA015143**.

Jia, Z., Zhan, Z. and Kanamori, H., (2022). Earthquake: A Slow Event Sandwiched Between Regular Ruptures, *Geophysical Research Letters, 49*, (3). **https://doi.org/10.1029/2021GL097104**.

Kowalik, Z., and Proshutinsky, A., (2010). Tsunami–tide interactions: A Cook Inlet case study. *Continental Shelf Research*, 30, 633– 642. doi 10.1016/j.csr.2009.10.004.

Larocca, Patricia A.; Arecco, María A.; Mora, Mariana C., (2021). Wavelet-based Characterization of Seismicity and Geomagnetic Disturbances in the Sandwich del Sur Microplate Area. *Geofísica Internacional*. Vol 60, N°4, 320-332, **http://revistagi.geofisica.unam.mx/index.php/RGI/article/view/2119/1882**.

Larocca, P., Fiore, M., Oreiro F., Vilariño, I. and Arecco, M.A., (2019). Estudio de parámetros geomagnéticos y su posible influencia sobre anomalías sismo-ionosféricas. In Proceedings of the Sixth Biennial Meeting of Latinmag, Fernando Poblete, C. I. Caballero M, (Eds), Latinmag Letters, 9, Special Issue, Proceedings A18, 1-6, Rancagua, Chile. **https://www.geofisica.unam.mx/LatinmagLetters/LM19-0101SP/A-P/A.18-P.pdf**.

Leat P.T., Day S.J., Tate A.J., Martin T.J., Owen M.J. and Tappin D.R. (2013). Volcanic evolution of the South Sandwich volcanic arc, South Atlantic, from multibeam bathymetry. *Journal of Volcanology and Geothermal Research 265*: 60–77. **https://www.sciencedirect.com/science/article/abs/pii/S0377027313002552**.

Leat P., Fretwell P., Tate A., Larter R., Martin T., Smellie J., Jokat W. and Bohrmann G. (2016). Bathymetry and geological setting of the South Sandwich Islands volcanic arc. *Antarctic Science 28* (4), 293-303. doi:10.1017/S0954102016000043.

Lee, H. S., Shimoyama, T., & Popinet, S. (2015). Impacts of tides on tsunami propagation due to potential Nankai Trough earthquakes in the Seto Inland Sea, Japan. *Journal of Geophysical Research*: Oceans, 120, 6865– 6883. **https://doi.org/10.1002/2015JC010995**.

Maldonado A., Dalziel I. and Leat P.T. (2013). Understanding the evolution of the Scotia arc. *EOS 94*: 272–272. **https://agupubs.onlinelibrary.wiley.com/doi/pdf/10.1002/2013EO310004**.

Maldonado A., Dalziel I.W.D. And Leat P.T. (2015). The global relevance of the Scotia Arc: An introduction. *Global and Planetary Change 125*: 1–8.

Paudel, S. R., Banjara, S. P., Wagle, A., & Freund, F. T. (2018). Earthquake chemical precursors in groundwater: a review. *Journal of Seismology, 22*(5), 1293-1314. **https://link.springer.com/article/10.1007/s10950-018-9739-8**.

Rabinovich, A. B. (2010). Seiches and harbor oscillations. In Handbook of coastal and ocean engineering (pp. 193-236). **https://doi.org/10.1142/9789812819307_0009**.

Roucco M.I. and Del Valle, R. A. (2021, 12 de julio). Tsunami tectónico en las islas Orcadas del Sur de la Antártida Argentina. Fundación Marambio. **https://www.marambio.aq/tsunamiorcadas.html**.

Ruiz, F., Sánchez, M., Martínez. P., Giménez, M., Leiva, F., Álvarez, O., Introcaso, A. (2011). La estación magnética Zonda: estudio de perturbaciones magnéticas relacionadas con terremotos. San Juan, Argentina. Proceedings of Second Biennial Meeting of Latinmag, Special Issue, A.M. Sinito (Ed.), Latinmag Letters, Vol. 1, Special Issue, A16, 1-7. **https://www.geofisica.unam.mx/LatinmagLetters/LL11-0102P/A/A16-Ruiz-corregido.pdf**.

Shelby, M., Grilli, S. T., and Grilli, A. R. (2016). Tsunami hazard assessment in the Hudson River Estuary based on dynamic tsunami-tide simulations. *Pure and Applied Geophysics, 173* (12), 3999 – 4037. **https://doi.org/10.1007/s00024-016-1315-y**.

Sierra Figueredo, P., Mendoza Ortega, B., Pazos, M. et al. (2021). Schumann Resonance anomalies possibly associated with large earthquakes in Mexico. *Indian J Phys 95*, 1959–1966. **https://doi.org/10.1007/s12648-020-01865-6**.

Spivak, A. A., & Riabova, S. A. (2019). Geomagnetic variations during strong earthquakes. Izvestiya, *Physics of the Solid Earth, 55*(6), 811-820. **https://link.springer.com/article/10.1134/S1069351319060077**.

Takahashi, S., T. Iyemori y M. Takeda (1990). Ring current response to impulsive southward IMF: A cause of second development of the Dst index, *J. Geomag. Geoelectr., 42*, 1325-1331. **https://www.jstage.jst.go.jp/article/jgg1949/42/11/42_11_1325/_pdf**.

Takeuchi, A. Okubo, K., Takeuchi, N. (2012). Electric Signals on and under the Ground Surface Induced by Seismic Waves, *International Journal of Geophysics Volume 2012*, Article ID 270809, 10 pages, doi:10.1155/2012/270809.

Takla E., A. Khashaba, Abdel Zaher M., Yoshikawa A. and Uozumi T. (2018). Anomalous ultra-low frequency signals possibly linked with seismic activities in Sumatra, Indonesia. NRIAG *Journal of Astronomy and Geophysics, 7*:2, 247-252. doi: 10.1016/j.nrjag.2018.04.004.

Thomas H.J. and Juarez A. (2021). Stress–strain characterization of seismic source fields using moment measures of mechanism complexity, *Geophysical Journal International*, Volume 227, Issue 1, October 2021, Pages 591–616, **https://doi.org/10.1093/gji/ggab218**.

Varotsos P. A., Sarlis N.V., Skordas E.S., Lazaridou M.S. (2013). Seismic Electric Signals: An additional fact showing their physical interconnec-

tion with seismicity, Tectonophysics, Volume 589, 116-125. **https://www.sciencedirect.com/science/article/pii/S0040195113000024**.

Woodworth, P. L., Pugh, D. T., Meredith, M. P., and Blackman, D. L. (2005). Sea level changes at Port Stanley, Falkland Islands. *Journal of Geophysical Research: Oceans, 110* (C6). **https://agupubs.onlinelibrary.wiley.com/doi/full/10.1029/2004JC002648**.

Zhao, J., Gao, Y., Tang, J., Klemperer, S. L., Wen, J., Chen, C.-H., and Chong, J. (2021). Electromagnetic field generated by an earthquake source due to motional induction in 3D stratified media, and application to 2008 M_w 6.1 Qingchuan earthquake. *Journal of Geophysical Research: Solid Earth, 126*, e2021JB022102. **https://doi.org/10.1029/2021JB022102**.

Geofísica Internacional (2023) **62-3**: 563 - 579

Modeling Forest Wildfires at Regional Scales

José de Jesús Graciano-Luna[1], Felipa de Jesús Rodríguez-Flores[2], Sacramento Corral Rivas[3]* y José Návar[4]

Abstract

This paper sets the following objectives: (i) presenting, (ii) testing, and (iii) evaluating a set of mathematical techniques to forecast the number of forest wildfires (No), the burned area (A), and the mean burned area (MA), on annual basis at regional scales. A comprehensive wildfire data set for coniferous forests of the State of Durango, Mexico was used to fit (1970-2011) and to validate (2012-2016) some modeling techniques. Most tested probabilistic and stochastic models hardly explain 70% of the wildfire variance. However, the teleconnection approach using a combination of large scale and local hydroclimate anomalies better predicted both data sets; explaining nearly 80% of the wildfire variance for fitting and for validating models. Results stress the complexity of interactive factors including the stochastic and underlying physical process that makes the prediction of wildfires losing precision and they should be further considered in future conceptual models. Therefore, proposing a more physical-based and conceptual models including Montecarlo models is an integral component of this paper; with the goal of increasing prediction capabilities and assisting decision-makers on the prevention activities inherent to better control wildfires. This proposed conceptual model stresses the need for using the probabilistic, stochastic and physical techniques to improve sub-model parameterization. Furthermore, the use of Monte Carlo simulation techniques would extract the most likely future scenarios for predicting the risk of high-severity wildfire regimes in temperate forests elsewhere.

Key words: Probabilistic, Stochastic, Physically-based and Conceptual models; Regional scales.

Resumen

Este artículo tiene por objetivos: (i) presentar, (ii) probar y (iii) validar un conjunto de técnicas matemáticas para predecir el número de incendios (No), la superficie incendiada (A), y la superficie promedio incendiada (A_M), en bases anuales a escalas regionales. Una fuente de datos extensa proveniente de los bosques de coníferas de Durango se usó para ajustar (1970-2011) y validar (2012-2016) las técnicas de modelaje. La mayoría de los modelos probabilísticos y estocásticos explican menos del 70% de la varianza de los incendios. Sin embargo, el método de teleconecciones que emplea variables a escala oceánica y a escala local del hidroclima aumentó el nivel de precisión hasta cerca del 80% de la varianza total para ambas bases de datos. Los resultados muestran la complejidad de los factores que interactúan, incluyendo los procesos estocásticos y los físicos que hacen que las técnicas de predicción sean modificadas substancialmente. Por estas razones, se propone un modelo más físicamente basado y también un modelo conceptual más comprensivo. El modelo conceptual requiere del uso de todas las técnicas presentadas en este reporte, incluyendo los modelos probabilísticos, estocásticos y físicos en la parameterización de los diferentes submodelos. El uso del modelo conceptual además de sus técnicas de simulación Monte Carlo extraerían los escenarios futuros mas probables en la predicción del riesgo de incendios forestales severos en bosques templados del mundo.

Palabras clave: Correlación cruzada, Ondas de Rayleigh, Dispersión de velocidad de grupo, Efectos de sitio.

Received: August 13, 2019; Accepted: October 25, 2022; Published on-line: July 1, 2023.

Editorial responsibility: Dr. Arón Jazcilevich-Diamant

* Corresponding author: Sacramento Corral Rivas, sacra.corral@gmail.com
[1] Professor of Silviculture. Tecnológico Nacional de México/Instituto Tecnológico de El Salto. Av. Mesa del Tecnológico s/n. El Salto, P.N., Durango, México. CP 34942. Email: gracluna@hotmail.com
[2] Professor of Forestry. Universidad Politecnica de Durango. Carretera Durango-Mexico Km 9.5. Localidad Dolores Hidalgo, Durango,México. C.P. 34300. Email: jesu_regz@hotmail.com
[3] Professor of Forest Management. Tecnológico Nacional de México/Instituto Tecnológico de El Salto. Av. Mesa del Tecnológico s/n. El Salto, P.N., Durango, México. CP 34942. Email: sacra.corral@gmail.com.
[4] Professor of Forest Hydrology and Watershed Management, Tecnológico Nacional de México/Instituto Tecnológico de Ciudad Victoria. Blvd. Emilio Portes Gil No 1301 Pte. Cd Victoria, Tamaulipas, México. 87010. jose.navar@itvictoria.edu.mx. Tel&Fax: 52-8341532000 ext 333.

https://doi.org/10.22201/igeof.2954436xe.2023.62.3.1713

Introduction

The prediction of forest wildfires has been the objective of intensive research for many years. Main components of the occurrence of wildfires are forest fuels, ignition sources and oxygen supply. The mass of forest fuels and its moisture content directly impact wildfire intensity and spread rate (Oliver and Larson, 1996; Shlisky *et al.*, 2007). Forest fuels are usually classified as ground (organic soil, duff, and moss), slash (litter), living trees and miscellaneous (Reinhardt and Crookston, 2003). Hydro-climate is the single most important factor desiccating forest fuels and in particular unusual drought episodes associated with dry warm winds originated by large scale climate circulation events control the moisture content of fuels (Andrade and Sellers, 1988; Swetnam and Betancourt, 1989; Návar and Lizárraga, 2014). Sources of ignition can be natural (lighting) and anthropogenic (direct and indirect ignition) and stable and migrant population density in forests correlate well with wildfire features.

Fires regimes in northern forests of Mexico and probably elsewhere in the World are featured by infrequent high-severity wildfires with a small probability of occurrence and small-severity wildfires with a large probability of occurrence (Rodriguez-Trejo, 1996; Drury and Veblen, 2008). Limiting factors in the later regimes (fuel loadings, moisture content, climatic factors, among others) keep under control the area burned; while the former ones have commonly no limiting factors for wildfires to spread until nature itself controls them. Small-severity wildfires keep fuel loads under control mimicking prescribed burns retarding the presence of high-severity wildfires (Fule *et al.*, 2004; Shlisky *et al.*, 2007). Unfortunately, these wildfires are most often quickly controlled interfering with the natural build up of forest fuel loads. These natural variations and human interventions have important fingerprints on wildfire regimes; e.g., the number and the area burned by wildfires. Given the limited data, predictions are difficult to carry out at this time because even conventional forecasting techniques convey a large unexplained variation (Johnson & Miyanishi, 2001).

Recent research has revealed high-severity wildfires occur when a series of local and large scale events develop continuously over time scales of months: e.g., unusual intense winter frosts that add large amounts of fresh foliage onto the forest soil; infrequent spring drought spells; and late spring-early summer heat waves that provide additional fuels and the environmental conditions to unleash high-severity wildfires (Fernandes *et al.*, 2012; Návar, 2015). However, conceptual models that describe more objectively each one of these perturbation components are lacking elsewhere. Other major random sources of fresh foliage input little studied and quantified are: (i) tree dieback by dry spells associated with intense heat waves (Allen *et al.*, 2010; Návar, 2015); (ii) tree mortality by pests and diseases; (iii) frosting winds; (iv) hurricanes; (v) among others. These large-scale perturbations, in part, control the amount of fresh fuel loads and the moisture content impacting directly on the spread rate, intensity and extent of high-severity wildfires.

Technologies available to predict the risk factor of wildfires have been continuously updated, amongst which just to mention a few are: a) The Canadian Forest Fire Danger Rating System (**http://fire.cfs.nrcan.gc.ca**); b) The Integrated System of Italy (Fiorucci *et al.*, 2004); c) The Meterological Institute of Portugal (Bugalho y Pessanha, 2007), d) The CFS-Conafor for México (CONAFOR, 2012); among others. Fulé and Covington (1997; 1999), Aguado *et al.* (2003), Hernández-Leal *et al.* (2005), Sebastian *et al.* (1999; 2000; 2007) proposed other empirical assessments of wildfire regimes for several sites or regional-specific uses. In general, all these systems model several major components; the meteorological index and the forest wildfire behavior. The meteorological index includes the quantification of the moisture content with climate variables and more recently with the presence of hotspots. Most frequently climatic data collected from instrumental devices and satellite techniques such as: air temperature, relative humidity, evapotranspiration, wind speed and direction, precipitation, hotspots, among others are used individually or in combination to evaluate the meteorological or climatic index (**http://fire.cfs.nrcan.gc.ca**). A few investigations have considered hydrologic balances of e.g., the moisture content of soils that are closely related with the fuel moisture content as a major variable to predict one of the major controls of wildfires (Lawson *et al.*, 1997; Návar, 2011; 2015). The forest wildfire behavior accounts for all fuels, climatic and topographic factors (Rodríguez-Trejo, 1996). However, most of these models and techniques hardly include more physically-based techniques to predict most wildfire components.

Given this brief literature review, this report aimed to predict three wildfire variables using conventional: a) stochastic and b) probabilistic; and propose non-conventional: c) physical and d) conceptual models as an aid for preparedness for the worst case scenarios. Wildfire data in number and area burned for the State of Durango, México was used to test set models with the hypothesis they would significantly account for part of the wildfire variance.

Materials And Methods

Study Area. Wildfire data was collected for temperate forests of the State of Durango, Mexico. The State is located in the north-central portion of Mexico and has an area of approximately 12.3 M ha (Figure 1). It spans 22º35' NL and 104º50' WL; 24º44' NL and 22º58' WL; 26º83' NL and 104º27' WL, and 23º52' NL and 107º21' WL; neighboring the States of Chihuahua and Coahuila to the north and east; Coahuila and Zacatecas to the east, Zacatecas and Nayarit

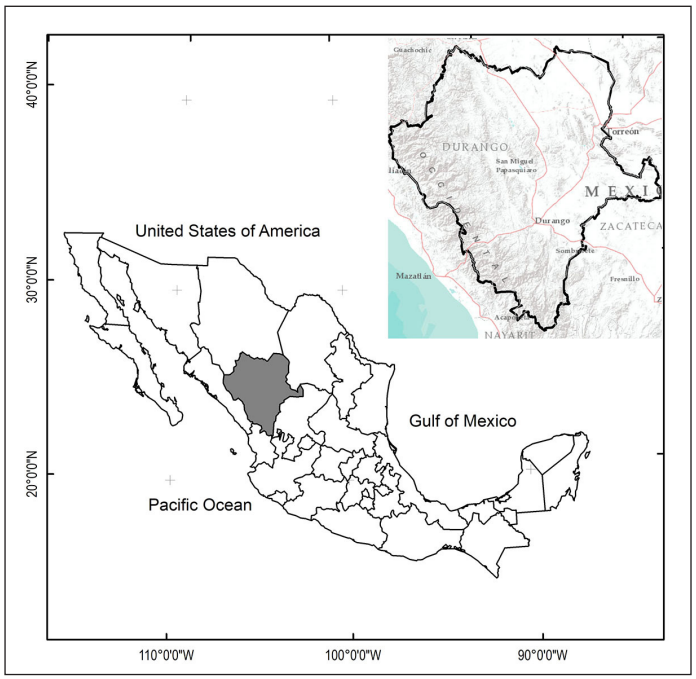

Figure 1. Location of the State of Durango in México.

to the south and Sinaloa and Nayarit to the west. Four main physiographic regions characterize the State; a) the Western Plains of the Pacific Ocean, b) the Sierra Madre Occidental Mountain Range, SMW, c) the Central Valleys of Durango and Chihuahua, and d) the Chihuahuan Desert.

The SMW Mountain Range is the continental divide and rises West of the Chihuahuan Desert and East of the Plains of the Pacific Ocean up to 3000 m above sea level, masl, crossing the State from North to South in its Central-Western portion. Temperate forests with mixtures of pines, oaks, and other conifers cover this Mountain Range; with common species *Pinus cooperi*, *P. durangensis*, *P. engelmannii*, *P. teocote*, *P. herrerae*, *P. leiophylla* and *P. ayacahuite*. The most frequent oak species found are *Quercus sideroxyla*, *Q. durifolia*, *Q. rugosa* and *Q. candicans. Juniperus* , *Cupressus Pseudotsuga* and *Abies* are other temperate conifer species that make up the forest community. Other broad leaf species growing within these forests are *Arbutus* spp. and *Alnus* The lower strata are conspicuous and dominated by manzanita (*Arctostaphylos pungens*) and encinilla (*Quercus striatula*).

The SMW features several microclimates, according to the Köppen climatic classification scheme and modified for Mexico (García, 1987): a) in the highlands, the temperate-cold, humid climate, with summer rains and mean annual temperature and precipitation of 14°C and 1000 mm, respectively. The interior lower ridges are characterized by semi-arid, dry temperate forests with mean annual temperature and precipitation of 16°C and 800 mm. The Pacific Ocean ranges are characterized by subtropical warmer dry climates.

Forest wildfire data. Annual data covering the number of wildfires, the total burned area and a derived variable the mean burned area (e.g., total burned area / number of wildfires) was available for the State of Durango Mexico from 1970 to 2011 (Figure 2).

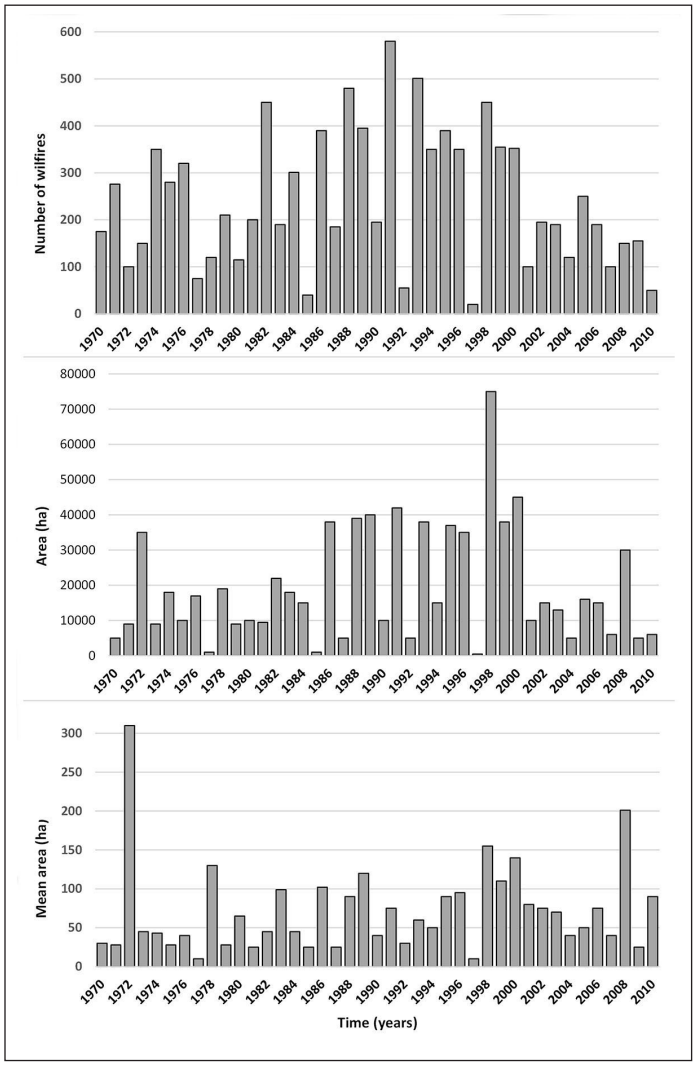

Figure 2. Forest wildfire data (number of forest fires, area burned annually, and mean annual burned area) recorded for the State of Durango, Mexico (Source: CONAFOR, 2018).

Conventional mathematical techniques used to forecast wildfires

Testing the time series for stationarity. Conventional linear regression analysis usually tests the hypothesis for changes in the first momentum of the time series wildfire data; e.g., $Y = a + bX$; where Y = the wildfire variable; X is just a consecutive year number (1970 to 2011 for annual data); a, b are statistical parameters to be estimated using statistical programs such as SAS v 8.1. If Ho (B = 0) is correct then no statistical significant temporal tendencies are depicted by the wildfire data. Autoregressive integrated moving average, ARIMA, models have also fitted the annual time series data to statistically test for stationarity by fitting linear and quadratic trends as well. Monthly and annual wildfire

data variables are sometimes smoothed; then the ARIMA models fitted to the data set. The conducted statistical tests show whether the wildfire data is stationary and independent using the probability of the F-Fisher and/or t-Student statistics. Wildfire data was stationary in the first momentum ($P \geq 0.05$).

Stochastic Methods. Stochastic methods include a series methods and techniques that are available for the prediction of wildfire variables. These include at least all regression equations that convey physical or none physical meaning at all.

Teleconnections. The term tele-connection refers to a recurring and persistent, large-scaleclimate pattern (pressure- and circulation anomalies) thatspans vast geographical areas (CPC: www.cpc.ncep.noaa.gov) that could be associated with local e.g., wildfire events. Synoptic scale climate variables depicted by sea surface temperature anomalies, SST, such as El Niño/Southern Oscillation, ENSO (Cavazos and Hastenrath, 1990), and its different indices such as the Southern Oscillation Index, SOI, or the Ocean El Niño Index, ONI, has been previously correlated with wildfires in Durango (Návar, 2011). The SST in the regions 1, 1+2, 3+4 and 4 are also indices of ENSO. In addition, the Pacific Decadal Oscillation, PDO, (Mantua *et al.*, 2002) and the Atlantic Multidecadal Oscillation, AMO, (NOAA, 2020) could be correlated to local wildfire variables since they modify the regional climate of several places of Earth.

Large and local spatial scales. Forests and soils have the capacity to regulate several variables of the hydro-climate as they store and release sometimes slow water fluxes out of the forest ecosystem buffering the effect of hotspots or acute short dry episodes on for example the moisture content of fuels. Hence the joint association between large scale (ENSO, PDO, AMO) and local (θ) variables would provide better predictions of wildfire variables.

Autoregressive integrated moving average, ARIMA, models. ARIMA models capture the dependence between observations at t previous times by removing a persistent mean value. ARIMA models may include all three, two, or one component: (i) the autoregressive, (ii) integrated, or (iii) the moving average components. When one autoregressive component is sufficient the model is said to be ARIMA (1,0,0), and so on. The autoregressive component is usually the regression equation of the wildfire variable a t t= ti versus the wildfire variable at $t=t^{-1}$. Most often a first or second order autoregressive ARIMA model would predict the wildfire variable of interest. The problem with ARIMA models is that they require a quite comprehensive data set in order to extract a robust model.

Simple regression equations. Regression analysis use single or multiple independent exogenous variables that may or may not be physically related to the wildfire data. Classic regression equations include the association of instrumented data such as precipitation, temperature, evaporation with the wildfire variables.

Probabilistic Models. Probability density functions. Probabilistic models project random values of the variable of interest, in this case the wildfire data, by fitting probabilistic density functions, pdf (Haan, 2003). Several pdf models had been fitted to wildfire data amongst which the Frechet, Truncated Pareto, Weibull are the most commonly cited (Alvarado *et al.*, 1998). The selection of the pdf that best fit the random data commonly uses the classic goodness of fit tests the xi2 and the Kolmogorov-Smirnoff tests.

Markov chain matrices and models. A second stochastic approach to forecast wildfire data or events divides process into states. For example, the burned area time series can be considered a process with a mean value of 17,753 ha and minimum and maximum values of 435 and 68,960 ha indicating that any size of burned area within these boundaries is possible. The division of this process into for example 2 or 3 different states would be to classify values into states 1 and 2 or 1, 2 and 3. Of interest would be to classify as many states as possible with the major interest of understanding and predicting the risk of high- severity wildfires. Unfortunately the data matrix is sometimes not long enough to divide it into many states.

First order Markov model. Markov models or processes is a stochastic model describing the sequence of possible events in which the probability of each event depends on the state reached in the previous events. A first order Markov model uses only the understanding of the state attained the previous time step.

Results

Predicting Wildfires

As an example, forest wildfires in number, area and mean area were predicted using stochastic, probabilistic, and physical models as well as a conceptual more comprehensive model was proposed.

A. Stochastic Models.

1. Tele-connections between large-scale synoptic events and wildfires. In this research, No, A, and A_M were regressed against ENSO indices (SST, SSTA, SOI) for the four regions of the Southern Pacific Ocean (1, 1+2, 3+4, 4) and PDO and AMO anomalies using multiple regression analysis. Table 1 reports the degree of association of the individual synoptic climate variables with No, A, and A_M for the State of Durango, Mexico.

The amount of variability significantly ($P \leq 0.05$) explained by the SST anomaly variables is from low to moderate since the coefficient of determination hardly exceeds 55% of the total wildfire variance, stressing other local variables have also a marked influence on wildfire regimes

Table 1. The degree of linear associations of several synoptic scale climate variables with forest wildfires in the State of Durango, Mexico.

Wildfire Variable	Variable	R^2	N
No	$SST1_{JUNE}$	0.19	21
No	PDO_{JUNE-1}	0.15	41
A	$SST3_{MAY}$	0.23	21
A	$SST1_{FEBRUARY}$	0.27	21
A	AMO_{JUNE-1}	0.09	41
AM	$SST3_{MAY}$	0.53	21
AM	$SST2_{MAY}$	0.22	21
AM	PDO_{DIC-1}	0.14	41

The amount of variability significantly ($P \leq 0.05$) explained by the SST anomaly

as well. Of importance is the A_M predicted by the $SST3_{MAY}$ index of region 3+4 that individually accounts for by 53% of the total A_M variability.

Large spatial scale and local hydro-climate variables. Monthly and seasonal combined SST anomalies in addition to local precipitation, P, and soil moisture content, θ, also predicted moderately well with statistical significance the wildfire data set (Table 2).

These kinds of teleconnection regression equations improve the power prediction by explaining an important part of the wildfire variance ($P \leq 0.05$) although they still convey an important portion of unexplained variation. Of importance is how the synoptic climate components in conjunction with the local variables (θ) describe better the wildfire variability. In particular, the equation of the L(A) model accounts for by 73% of the total area burned variance and include a combination of local hydro-climatic (θ) and the SST (AMO and SOI) anomalies. These combination of exogenous variables partially test the independence of local and long spatial scale variables. That is, the local regulation by the forest and soil can play an important role in wildfires. The power prediction of these tele- connections regression equations reported in Table 2 in logarithmic fashion are depicted in Figure 3.

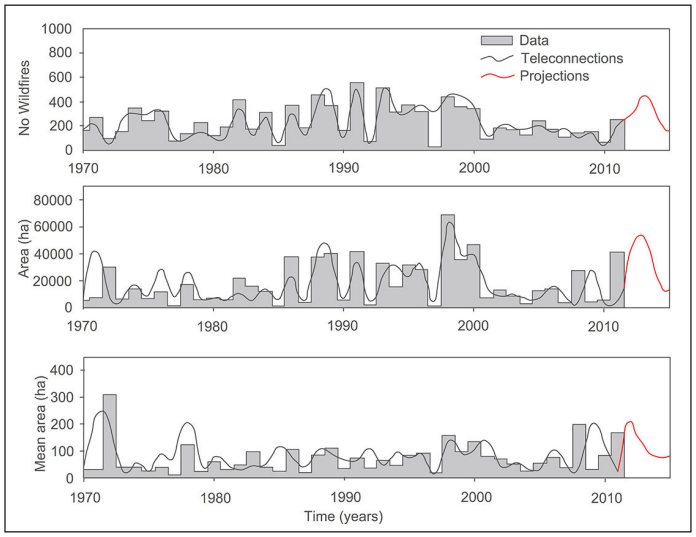

Figure 3. Modeling wildfire data using teleconnection regression equations coupled with local climate and soil data.

Table 2. The degree of association of several synoptic scale climate variables with wildfires in Durango, Mexico.

Wildfire Variable	Variable	R^2	N
No	$SST1_{OCT-1-MAR}$, $SST3_{OCT-1-MAR}$	0.50	21
A	$SST3_{OCT-1-MAR}$, $SST1_{OCT-1-MAR}$	0.31	21
L(AM)	PDO_{NOV-1}, PDO_{AG-1}, AMO_{NOV-1}, AMO_{SEP-1},	0.44	41
AM	PDO_{DEC-1}, PDO_{OCT-1}, PDO_{AG-1}, PDO_{JUL-1}, AMO_{JUL-1}, AMO_{AG-1}	0.53	41
L(No)	$L_{(PDOJAN-MAR)}$, AMO_{FEB}, SOI_{JUL}	0.51	41
L(A)	$L(PDO_{JAN-MAR})$, $L(\theta_{JAN-MAY})$, AMO_{JUN}, SOI_{FEB}	0.73	41
L(AM)	$L(PDO_{JAN-MAR})$, $L(\theta_{JAN-MAY})$, SOI_{FEB}	0.48	41

Where: OCT=October, MAR=March, NOV=November, AG=August, SEP=September, DEC=December, JUL=July, FEB=February, JAN=-January, SST=Sea surface temperature anomaly, PDO=Pacific decadal oscillation, AMO=Atlantic multidecadal oscillation, SOI=Southern oscillation index, Prec=precipitation, θ=Soil moisture content, L = natural logarithm, 1=Region 1, 3=Region 3+4; -1= the previous year.

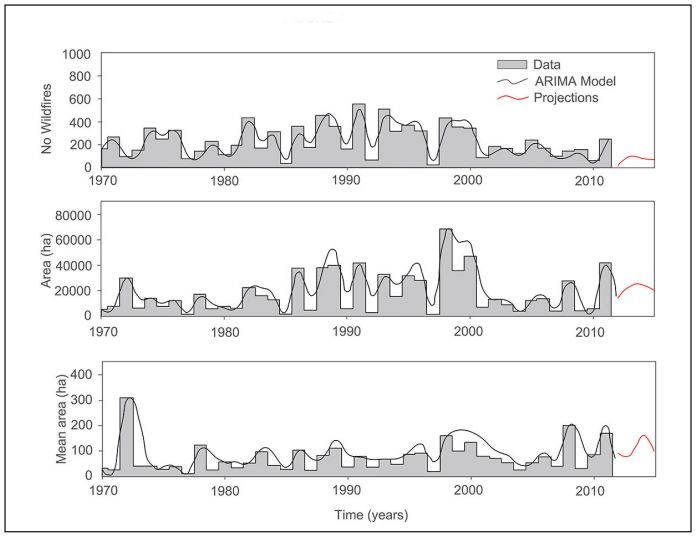

Figure 4. Autoregressive integrated moving average models projecting the number, the total area and the mean area burned by wildfires in Durango, Mexico.

Other single independent teleconnection equations were reported previously by Návar (2011), as follows: A= 31600-12224ENSO$_{NOV_DIC-1}$, with an r^2 of 0.37.

2. Autoregressive integrated moving average, ARIMA, models. All ARIMA models of the type ARIMA (1,0,0) in a log transformation data explained 48%, 45%, and 32% of the wildfire data set (No, A, A_M, respectively). Examples of ARIMA models fitted to this data set are displayed in Figure 4.

The advantage or disadvantage in rapid changing world climate extreme variability events, when using these stochastic models is that they can predict the future wildfire data with the same statistical properties as the original data set. Other ARIMA models using heterogeneous variance (ARCH and GARCH) had been recently developed that improve the predictability power for the time series with heteroscedasticity properties. However, the wildfire time series for Durango was tested for stationarity and independence and it is not long enough to show the likely heterogeneous variance that must have the high-severity in contrast to the small-severity wildfires and to fit the new ARIMA models. Other composed ARIMA models in conjunction with explanatory variables that may lead to the development of parametric models are under development and they will become better prediction techniques once they are tested and become available in the near future.

3. Regression equations. Annual, seasonal or weighted rainfall, evaporation, mean seasonal soil moisture content or the number of dry days during the dry season have been associated with some degree of confidence with forest wildfires. Using the single most representative climatic station of El Salto, Dgo., Mexico (2570 masl), regression equations associated with wildfires are reported in Table 3.

These local variables have a low to medium predictive power as the r^2 hardly exceeds 50% of the wildfire variance.

Table 3. Degree of association between wildfire variables and several micro-climatic variables for the State of Durango, Mexico.

	Variable	**Coefficient of Determination (r^2)**		
	X = θ	No	A	A_M
Number of Days with soil moisture content below θx	0.29	0.15	0.23	0.18
	0.31	0.14	0.23	0.18
	0.33	0.11	0.19	0.17
	0.35	0.13	0.22	0.18
	0.37	0.13	0.21	0.18
	0.39	0.12	0.21	0.17
	0.41	0.11	0.19	0.16
θ (Jan-Jun)	1-6	0.22	0.44	0.33
θ (Jan-May)	1-5	0.24	0.32	0.21
θ (Jan-April)	1-4	0.26	0.33	0.20
θ (Jan-March)	1-3	0.30	0.60	0.21
θ (Jan-Feb)	1-2	0.29	0.33	0.17
Annual Precipitation	P	0.00	0.00	0.04
Annual Evaporation	EV	0.03	0.10	0.07
Annual Evapotranspiration	ET	0.01	0.01	0.04
Dry Season (Jan-May)	P	0.36	0.47	0.27
Dry Season (Jan-May)	EV	0.07	0.14	0.08
Dry Season (Jan-May)	ET	0.12	0.16	0.09

Note: These related variables are derived from a single climatic station while the number and area burned by wildfires is for all the State of Durango, Mexico. The number of days with soil moisture content below θx value, the mean soil moisture content, θ, Evapotranspiration and Real Evapotranspiration were modeled using a water balance budget approach. Data estimated for a single climatic station at El Salto, Durango, Mexico.

Of importance is the variable spring θ that is associated to the moisture content of fuels as well as the weighted Et component that is associated with both the heat and water available in the forest ecosystem. In case of using combined exogenous variables, the solution to the problem of heteroscedasticity relays on developing single, independent equations that predicts e.g., the A= (3170Exp(0.089/(θJ_{AN-MAR}0.2451)); r^2=0.60 that would yield more reliable predictions (Návar, 2015).

Using monthly temperature and precipitation data from other climatic stations located across the SMW mountain range, we developed multiple linear regression equations reported in Table 4.

The use of instrumental climate data from other climatic stations increase prediction power of wildfires by accounting for nearly 50% of the total wildfire variance and having more stable statistical coefficients stressing the localized nature of wildfire at several times in the past and hence the aggregated nature of wildfires, as proposed earlier (Perez-Verdin *et al.*, 2014). A potential geographical escalation could be also part of the prediction of wildfire regimes as drought develops seasonally quite frequently in latitude, longitude and altitude (Vega-Nieva *et al.*, 2019).

B. Probabilistic Models.

1. Probability density functions. Examples of three pdf's fitted in addition to the goodness of fit to each of the three wildfire variables are displayed in Figure 5.

The Kolmogorov-Smirnoff, KS, goodness of fit statistic is also embedded into each of the figures. The Truncated Pareto is an excellent model for high-severity wildfire data but fails to describe well the small-severity ones. The Weibull pdf function consistently models better all three sources of wildfire information. When using the Chi^2 fitness statistic, the Weibull pdf tests the null hypothesis ($P > Chi^2 = 0.22$; 0.12; and 0.16) of significantly describing well No, A, and A_M, respectively.

The simulation of time series using random numbers retains the statistical properties of the original pdf and eventually produces similar values. The probability of high-severity burned areas (e.g., A > 20,000 ha) remains the same year after year. For this example, P(A>20,000 ha) = 31.67% for the original as well as for the simulated series. These results are important for the long term planning of the management of wildfires in the area of interest. However, they have little year to year predictive power unless the pdf is used within certain boundaries and coupling with other Bayesian techniques. For example, for these time series wildfire variables are related to each other (No = 1.9494$Area^{0.4924}$; R^2=0.66; A_M = 0.513$Area^{0.5076}$; R^2=0.67) aiding in the prediction of the total area burned larger than 20,000 ha that could be of interest in forest fire management. Using the power regression equations reported above; this burned area is produced by about 255 wildfires with a mean burned area of 78 ha per wildfire. Using the Weibull pdf, there is a 31.67% of probability of any given year to have a burned area larger than 20,000 ha and it has therefore a probability of 68.33% of having a burned area smaller than 20,000 ha. Conditional probability would also eventually enhance prediction capabilities with the use of probabilistic models. The dependence

Table 4. Multiple linear regression equations developed to predict wildfire data using climatic data from several stations placed across the Sierra Madre Occidental Mountain Range of Durango, Mexico.

Wildfire Variable	Variable	R^2	N
A	Exp(2.68+0.037ATx_{JAN}-0.1424STn_{FE}-0.4217ATn_{MAR}+0.215AP_{MAR})	0.59	29
No	Exp(2.43+0.189ATx_{JAN}-0.0038SP_{MAR}+0.043TTn_{JAN}+0.053T-Tx_{FE})	0.49	38

Where: A=Altares, b S=El Salto, T=Tarahumar, Tx=Maximum Temperature (°C), 18 Tn=minimum temperature (°C), P=monthly precipitation (mm), JAN=January, FE=February; MAR=March.

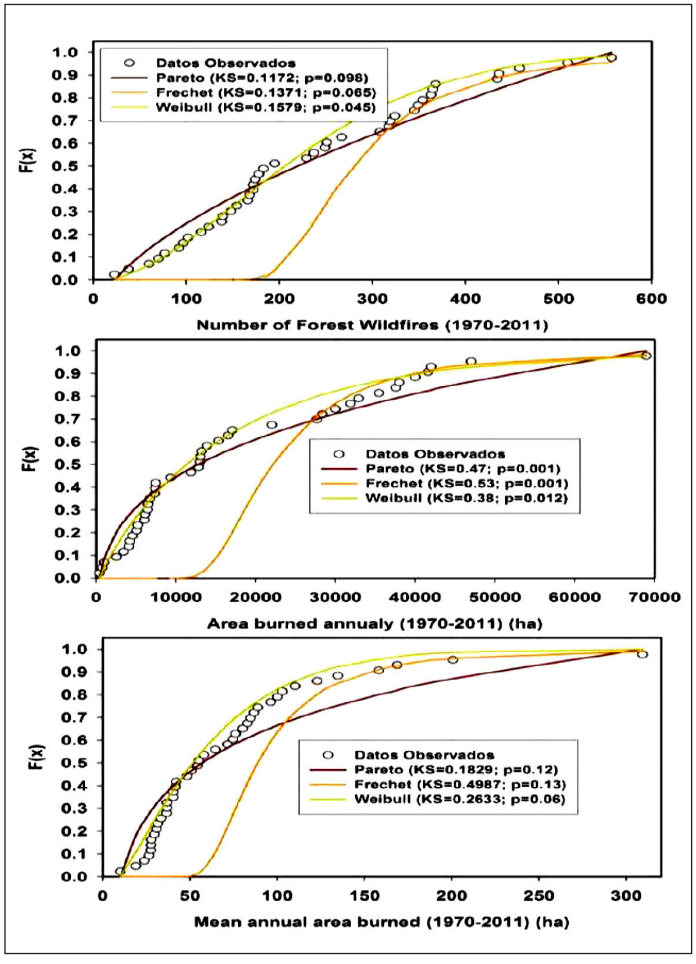

Figure 5. Three probability density functions fitted to the number of wildfires, the total area burned and the mean area burned in the State of Durango, Mexico.

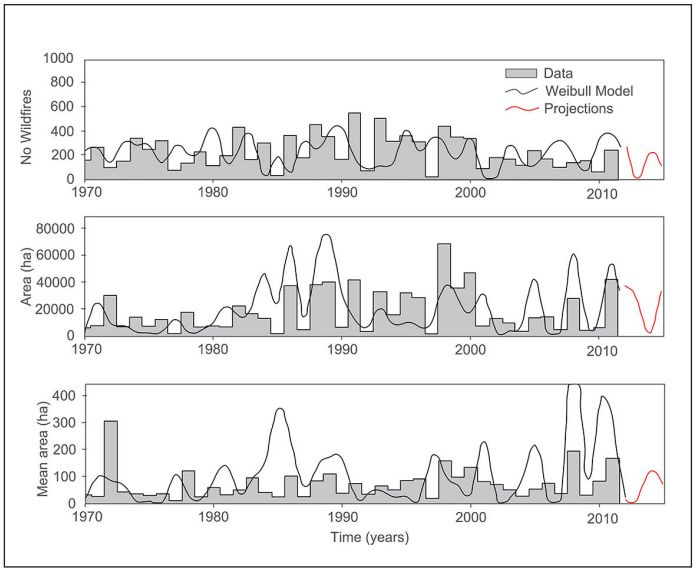

Figure 6. Measured and simulated random wildfire area data using Weibull probability density functions for northern temperate forests of Durango, Mexico.

of the probability on the explanatory X variables has been proposed in several statistical packages and they will eventually become techniques of wide acceptance and usage as the predictive power increase.

Assuming the Weibull pdf is a good model for the burned area; the generation of random values using this pdf function would provide predictions of past, present and future wildfire data. In this exercise using a simple Monte Carlo analysis generated 100 sets of 51 values (1970-2020) with the aim to use the series that correlates better with the measured wildfire data for the State of Durango, Mexico. Results are displayed in Figure 6.

The simulated burned area time series retains the statistics (e.g., for the mean burned area; mean = 20189 ha; standard deviation = 18373 ha; skew coefficient = 1.27) in contrast to the original measured time series (mean = 17753 ha; standard deviation = 15925 ha; skew coefficient = 1.18). The predictive power of these probabilistic models decrease in contrast with the ARIMA models ($r^2 \leq 0.45$) using a single realization of random numbers. Stronger Monte Carlo simulations may or may not improve the predictive power but they will probably extract better the true probabilities as well as any tendencies if any that would yield most robust likely future scenarios.

2. Markov chain matrices and models. For 2 states 1 was the burned areas of less than 20,000 ha and 2 burned areas larger than 20,000 ha. For 3 states; 1, 2 and 3 states could be for burned areas of less than 15,000; 15,001 ≤ 29,999; and ≥ 30,000, respectively.

The transition probabilities and their convergence matrices for two and three states for the total burned area are displayed next.

$$\begin{vmatrix} 0.6786 & 0.3214 \\ 0.7692 & 0.2308 \end{vmatrix} \quad \begin{vmatrix} 0.7053 & 0.2947 \\ 0.7053 & 0.2947 \end{vmatrix}$$

and

$$\begin{vmatrix} 0.6250 & 0.2083 & 0.1667 \\ 0.5714 & 0.1429 & 0.2857 \\ 0.6000 & 0.1000 & 0.3000 \end{vmatrix} \quad \begin{vmatrix} 0.6103 & 0.1735 & 0.2162 \\ 0.6103 & 0.1735 & 0.2162 \\ 0.6103 & 0.1735 & 0.2162 \end{vmatrix}$$

Both types of matrices for 2 and 3 states coalesce rapidly at steady state showing the stationary and the independence of the burned area time series. That is, for a Markov chain process with two states, the probability of shifting from a small-severity burned area (< 30,000) to a high-severity one (e.g., >30,000 ha) is exactly the same as if the process shifted from a high-severity burned area (>30,000 ha) to a small-severity one (<30,000 ha). For the 3 states Markov chain process, the steady state probabilities are also exactly the same for shifting back and forth from <15,000 ha; 15,0001 ha ≤ x ≥ 29,999 ha; and to ≤ 30,000 ha, respectively.

Future predictions of the area burned can be conducted using the three states matrix if for one moment it is assumed wildfires are not independent year after year by observing the area burned e.g., in 2012 (51626 ha; State = 3), the probability that A≤ 30000 ha in 2013 is then 99%; the probability that A ≤ 15000 ha in 2013 is then 72%; and the probability that 15000 ≤ A ≤ 30000 ha in 2013 is then 28%. The probability of the occurrence of wildfires with A ≥ 30000 ha in 2014 is 22%.

3. First order Markov Model. Measurements and predictions of wildfire data using a first order Markov model is depicted next in Figure 7.

The first order Markov model provides moderate ($0.44 \leq r^2 \leq 0.47$) predictions comparing the goodness of fit

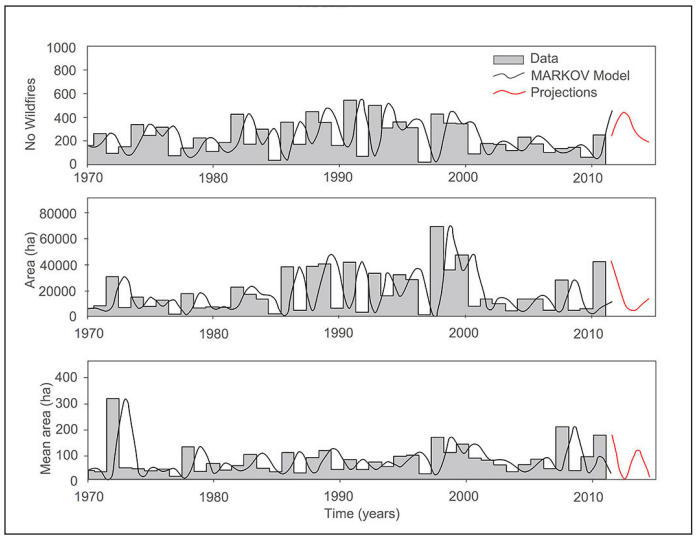

Figure 7. Wildfire data measurements and predictions using a first order Markov model.

statistics of the ARIMA models. A second advantage of Markov models is that they retain the same wildfire statistics (average, standard deviation, skew coefficient) as those of the original, measured data sets.

Short term wildfire predictions

Four single examples of measured and simulated wildfire data using five years of wildfire data set aside for validation of mathematical techniques is displayed in Table 5. The final row shows the coefficient of determination of the measured versus the predicted wildfire variables for each of four different prediction techniques.

The teleconnection technique using large scale as well as local hydroclimate exogenous variables provide more consistent results when validating the proposed equations (Table 5). However, large errors are expected when contrasting predictions with independent measured values left aside for validating models (Table 5). Most likely, using the properties of the Central Limit Theorem an average statistic using all available model predictions presented in this report would most likely improve assessment of the number or the area burned by wildfires in contrast to any single prediction equation by any mathematical approach tested in this report. This procedure would improve only average but not the extreme values that are important for the prediction of high-severity wildfires. As we are often interested in wildfire events such as those measured in 1998 during the strongest El Niño event of the last Century, other kinds of models must be developed to capture the variance of these high-severity wildfires.

Proposed New Models.

C. Physically-based models. More physically-based models should count for by the deterministic prediction of the three main components of forest wildfires; fuels and their moisture content, sources of ignition, and oxygen.

Fuels. Reinhardt and Crookston (2003) classified forest fuels as ground (organic soil, duff, and moss), slash (litter), living trees and miscellaneous (grass). These forest fuels can be further classified into: (i) litter, (ii) necromass, (iii) tips & stumps, (iv) branches, (v) foliage, (vi) living aboveground biomass. Litter has its origins in litter fall while foliage in the mass of leaves left on-site during harvesting operations.

Modeling litter and necromass stocks. Evaluations of forest fuel loadings on the forest floor conventionally measure altogether organic soil, duff, moss, litter and necromass.

Litter stocks. A physical model that predicts litter stocks and accumulation rates as a function of total aboveground biomass, the rate of losses weighted by site productivity was proposed for northern non-industrial reforested stands of Mexico (Návar, 2019). The physically-based model predicts cumulative litter stocks, LS, in growing forests. The model is parameterized using a mass balance budget approach as described below;

$$LsS = \frac{\partial LR}{\partial t} - \frac{\partial LO}{\partial t} \pm \frac{\partial LS}{\partial t} \quad [1]$$

$$\frac{\partial LR}{\partial t} = 13.55(1 - \exp(-0.003AGB))^{0.48} \quad [2]$$

$$LI - LO = \pm LS \therefore \frac{LO}{LI}(LI) = f(LI, \frac{P}{Et}, SI) \therefore LI(LO) = LS \quad [3]$$

The final model is described in Eq. [4] and Eq. [5], as follows:

$$LS = \left[\int_{t=0}^{t=t1} \frac{\partial LR}{\partial t} \cdot \partial t\right] - Exp\left[-0.85 + 1.12 * Ln(LI) - 0.77 * Ln\left[\frac{P}{ET}\right]\right] \quad [4]$$

$$LS = \int_{t=0}^{t=t} I \cdot \partial t - \int_{t=0}^{t=t} 0 \cdot \partial t \quad [5]$$

Where: LR = litter fall rate (Mg ha^{-1} y^{-1}); LO = rate of litter losses (Mg ha^{-1} y^{-1}); LS = litter stocks (Mg ha^{-1} y^{-1}); AGB = aboveground biomass (Mg ha^{-1}); P, ET = mean annual precipitation and Thornthwaite evapotranspiration, respectively (L).

The litter stock and accumulation model was previously validated with measured litter stock data for local Mexico's forests (Renteria *et al.*, 2005; Acosta-Mireles, 2003; Rodríguez-Laguna *et al.*, 2009; Mendoza-Ponce & Galicia, 2010; Aryal *et al.*, 2018; Caballero-Cruz *et al.*, 2018), as well as for average data reported for Mexico (CONAFOR, 2012),

Table 5. Validation of four mathematical techniques to predict wildfire data for the State of Durango, Mexico.

	Measured Data			ARIMA Models			Weibull pdf			Markov Model			Tele-connections		
Year	**No**	**A**	**A_M**	**No**	**A**	**A_M**	**No**	**A**	**A_M**	**No**	**A**	**A_M**	**No**	**A**	**A_M**
2012	270	22802	84	308	43705	149	373	37352	11	446	10376	4	200	42005	210
2013	231	12359	54	251	6893	3	10	26273	16	273	4891	109	450	53000	118
2014	199	5463	27	74	39541	118	224	2268	121	190	13323	1	300	25000	83
2015	68	517	8	347	1933	6	97	35417	66	396	17567	13	160	13323	83
2016	254	7277	29	635	53403	84	43	22219	30	197	9800	0	340	45000	132
R^2				0.03	0.13	0.24	0.07	0.13	- 0.40	0.05	-0.33	0.05	0.25	0.43	0.78

North American (Kohl *et al.*, 2015) and World (Kohl *et al.*, 2015) temperate forests (Figure 8).

Necromass: tree mortality by competition. Tree mortality is the main source of necromass accumulating atop the forest soil. Tree mortality occurs by competition and by stochastic processes. Tree competition can be predicted using the conventional technique of mortality by demography, as competition for space and resources is the main driver of tree mortality in overstocked forests and plantations. Overstocking develops in forests as trees grow in size. The Reineke equation predicts quite well tree density as a function of mean diameter, with a typical log-log relationship and the universal exponent of -3/2 ensures the reduction of the number of trees as they grow in diameter. Using this principle, an equation evaluating stand density, *Den* (No ha^{-1}), is developed. In this example, using available data for North American forests, the *Den* Eq. was developed, as follows;

Where: *Den* = stand density (No ha^{-1}); D = diameter at breast height (L).

$$Den = 87021 \cdot D^{-1.62} \quad [6]$$

Fortunately Eq. [6] reproduces similar *Den* data as the equation reported by Aguirre-Bravo (1987) for *Pinus cooperi* stands of Durango, Mexico. Then, the number of trees dying by competition was evaluated using Eq. [7],

$$Den_i - Den_{i+1} = \left[87021 \cdot D_i^{-1.62}\right] - \left[87021 \cdot D_{i+1}^{-1.62}\right] \quad [7]$$

The total number of trees killed by competition at t=t is evaluated using Eq. [8],

$$\int_{t=0}^{t=t}\left[Den_i - Den_{i+1}\right] \cdot \partial t = \int_{t=0}^{t=t}\left[87021 \cdot D_i^{-1.62}\right] - \left[8702 \cdot D_{i+1}^{-1.62}\right] \cdot \partial t \quad [8]$$

Using the diameter growth Eq. (D = f(T)) described by the sigmoid Chapmna- Richards function for local forests (Corral-Rivas and Návar-Cháidez, 2005); the Den = f(D) by Eq. [6], as well as the AGB =f(D) equation for individual trees reported earlier (Návar, 2009), we derived the cumulative AGB of killed trees by competition that are eventually aggregated to the forest floor as the main necromass input. Figure 7 presents the AGB density of killed trees by competition.

The annual tree mortality rate by intrinsic competition has an average of 2.0 Mg ha^{-1} y^{-1}. As expected it is more acute in the most productive forests. In temperate forests of Durango, Mexico, high-severity wildfires present an average frequency of approximately 30 years (Rodriguez-Trejo and Fule, 2003; Drury and Veblen, 2008) and using this information, under no management practices of on-site killed trees by competition, this forest would accumulate an average of 60 Mg ha^{-1}. However, because necromass has a half life time in the environment of 20 years as it decays over time; the final necromass density would be in the range of 20 to 30 Mg ha^{-1} during any average time interval between two consecutive high-severity wildfires.

Tree mortality by random processes. The forestry institutions over the world report forest inventories with the number and volume of dead on-site trees. For Mexico, the CONAFOR (2012) reports the total annual volume of harvested dead on-site trees, with a mean of 50,000 (±10,000) Mg. However, the total volume of dead on-site trees is approximated in the forest inventory and this volume

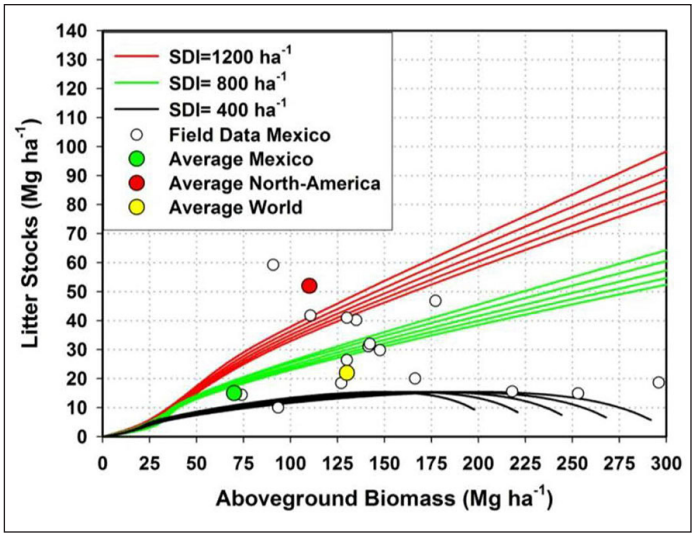

Figure 8. Modeling litter stocks & accumulation rates using a mass balance litter budget approach for northern temperate forests of Mexico coupled with a whole stand growth and yield model with three stand density scenarios (Source: Navar, 2019).

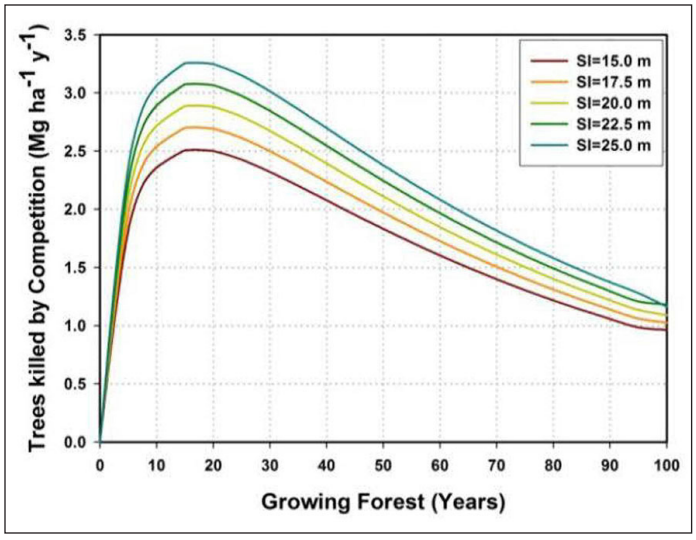

Figure 9. Quantifying the aboveground biomass density input of trees killed by competition in northern native forests of Durango, Mexico.

can be sometimes twice as large as the total official harvested timber volume. For example, Návar (2015) reported two important episodes (1998-2001 and 2012-2012) that killed on-site large number of trees by a combination of infrequent drought-related disturbances with heat waves, frosts, wildfires and bark beetle outbreaks. Official reports recorded an area affected of nearly 200,000 ha by these disturbances in each of these two dry spells that may have accounted for a standing biomass of approximately 1 M Mg.

The rate of tree mortality in the presence of other stochastic processes such as frosting winds, strong cold-dry winds, pests & diseases, drought spells associated with heat waves, among others require further attention since these stochastic events add large amounts of fuels in the form of litter and necromass to the forest floor. This explains why in some regression analysis, the minimum extreme temperature explains a significant portion of the large wildfire variability as it was the case for the data set of in Durango, Mexico. Unfortunately the data base comprising these random events is non-existent or at least a couple of data points in time are available making developed models to have a limited predictive power. More efforts are required to enriching the data base using paleo climate & historic wildfire data techniques.

Other forest management practices producing forest fuels Forest fuels as residues of conventional forest management operations. Timber harvesting also add considerable mass of litter, branches, stumps, and tree tops on the forest floor that can be predicted in advance quite well. Most of the stem component is harvested, with the exception of stumps, branches and tree tips. With the use of taper functions, the stem can be partitioned into merchantable or harvestable and non- merchantable or non-harvestable components. Most branches and all foliage components are usually left on site. With the use of aboveground biomass allometry, the mass of branches, foliage and timber stump & top components can also be predicted in advance.

Timber stumps & tips left on-site. Timber stumps are the basal portions of the main bole left standing on site. Timber tips are the distal portions of logs that do not meet the size requirements for its transformation into merchantable components. They are sometimes collected for the transformation of secondary forest products and sometimes they are left on-site as well. Mathematical functions that predict the stem profile had been developed over the years for many forests. An example for northern temperate tree species of Mexico reported by Návar *et al.*, (2013) is presented next. The equation of Newnham (1990) depicted by Eq. [9] with recorded parameters for local pines and oaks (Table 6) predicted total, merchantable, stump and tip volumes.

$$\left[\frac{d}{D}\right] = b_1 \cdot \left(\frac{H - hi}{H - 1.3}\right)^{b_2} \qquad [9]$$

Where: H = top height (m); hi = relative height (m); D = diameter at breast height (cm); d = relative diameter (cm)

Table 6. Coefficients of the Newnham (1990) taper model and their standard errors for tree species of northern Mexico.

		Parameters	
Species	Statistic	b_1	b_2
Quercus spp	Mean	0.010400	0.916300
	SE	0.000036	0.011100
Pinus spp	Mean	0.010300	0.595400
	SE	0.000017	0.003200

Source: Návar *et al.*, (2013).

The difference between total, Vt, and merchantable, Vc, timber volume evaluated the timber tip volume, Vtt, as explained mathematically by Eq. [10], as follows:

$$Vtt = Vt - Vc \therefore Vt = 0.7854 di^2 H$$

$$Vtt = 0.7854 \cdot \left[\int_{hi=0}^{hi=H} D \cdot b_1 \left(\frac{H - hi}{H - 1.3}\right)^{b_2} \delta hi\right]^2$$

$$- 0.7854 \cdot \left[\int_{hi=0}^{hi \therefore di=20} D \cdot b_1 \cdot \left(\frac{H - hi}{H - 1.3}\right)^{b_2} \delta hi\right]^2 \qquad [10]$$

Equation [10] cannot be analytically integrated, hence numerical analysis is conducted, e.g., using δhi=1 cm. Merchantable timber was evaluated from the base to the length of stem where diameter is > 20 cm. Logs with D ≤ 20 cm are classified as tips. Tip biomass was estimated by multiplying the tip volume times its wood specific gravity. Timber stumps are calculated using conventional empirical equations.

Branch biomass. Branch biomass of harvested timber can be quantified using allometric equations that have also been developed for many tree species for many forests. Návar (2009) reported for northwestern forests branch biomass equations for pine, Bbp, and oak, Bbq, tree species. These equations are:

$$Bbp = 0.0565 D^{2.2729}$$
$$Bbp = 0.0202 D^{2.6480} \qquad [11]$$

Where: dry biomass is in kg; D = diameter at breast height (cm).

Using this approach, the mass of fuels that remain in the forest floor is approximately 3 Mg ha^{-1} y^{-1}. An example of the calculations using the Newnham (1990) equation at the stand scale is reported in Table 7.

Table 7. Statistics for classifying biomass components of 62 overstocked stands of northern temperate, mixed, uneven-aged forests of Central Durango & Southern Chihuahua, Mexico.

	Total	Tree Tips	Stump	Biomass Components (Mg ha^{-1})				
				Branch	Foliage	Necro-mass	Sawnwood	Plywood
Mean	171.8	23.0	6.9	34.3	20.6	24.2	76.1	41.6
Standard Deviation	71.7	11.6	2.9	14.3	8.6	14.5	40.5	39.3
Confidence Interval	17.8	2.8	0.7	3.5	2.1	3.6	10.0	9.7

Evaluations of biomass components of Table 7 assume all trees are harvested in these forest stands. This is of course not possible as clear cutting practices are forbidden by the Mexican Forestry Law. Then, ratios can be used to predict the biomass components left on the forest floor as a function of the allowable harvest. These ratios must also be weighted by the half life in the environment of each forest fuel component.

Live trees. Live trees become also important sources of forest fuels especially when they reach very los internal moisture contents (<7%). The aboveground biomass contained in standing live trees can be evaluated using already developed allometric regression equations. A wide range of allometric equations at the species and temperate species were developed and reported by Navar (2009) that were applied to the Mexican Forest Inventory for Durango, Mexico. An example of this approach is presented in Figure 8 where close to 1700 forest inventory sites are displayed.

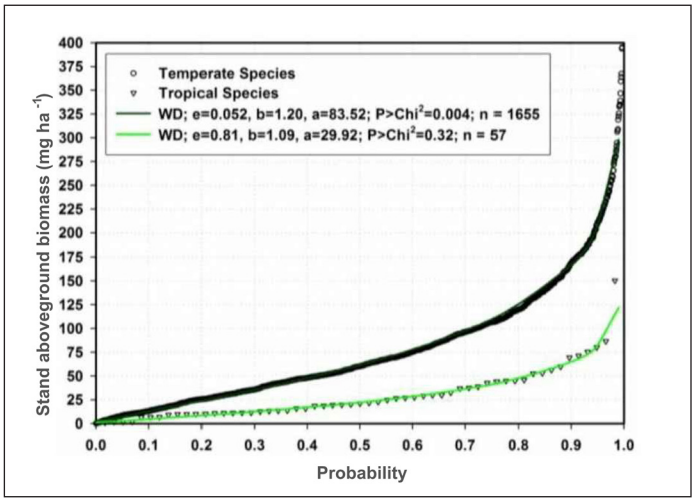

Figure 10. The aboveground biomass density for nearly 1700 forest inventoried sites of Durango, Mexico.

The climatic component. The moisture content of forest fuels is the single most important hydro-climatic component controlling wildfires because depending on the fuel water content the wildfire can simulate a prescribed burn, a small-severity or a high-severity wildfire. Due to the difficulty of continuously measuring and evaluating the moisture content of fuels, numerous climatic indices have been proposed with little predicting power; e.g., see statistics of Table 3.

The moisture content of forest fuels. The moisture content of forest fuels (ground, litter, grass, trees) can be deterministically evaluated using several approaches. Návar (2015) assumed the soil moisture content is in equilibrium with the forest fuel moisture content as they are in close contact and developed a physical water balance budget model to evaluate changes in soil moisture content, $\delta\theta$, over time, δt, that is depicted by the next set of equations.

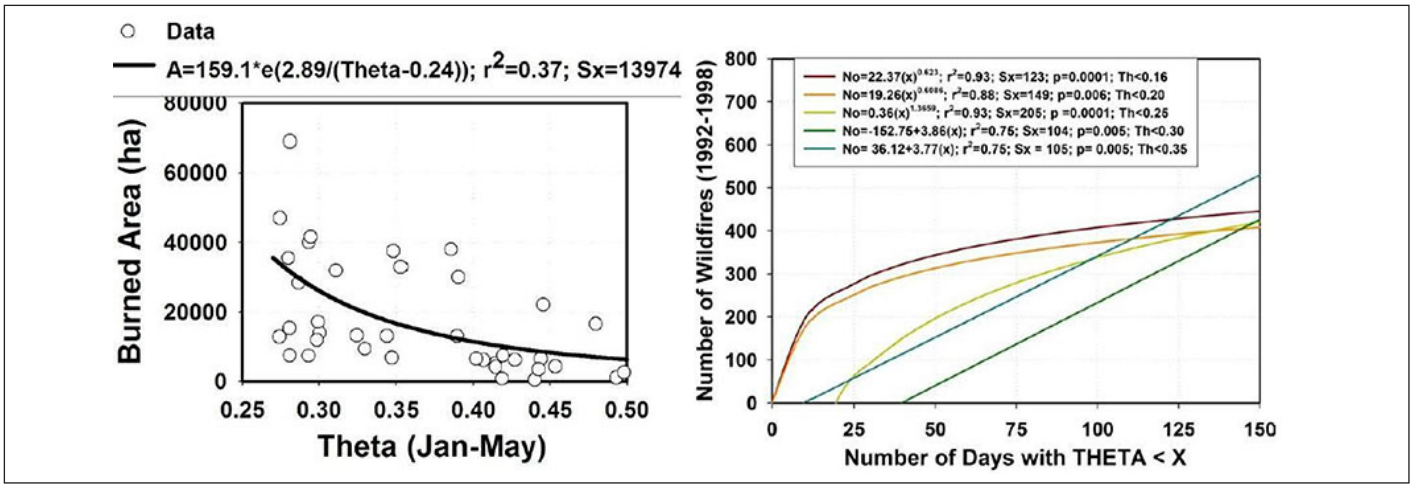

Figure 11. Predicting wildfire data with predicted soil moisture content for temperate forests of Durango, Mexico.

$$In - Ou = \frac{\partial \theta}{\partial t};\ In = P \quad [12]$$

$$Ou = \left[I_c + I_L + E_V + T_R + Q_s + Q_{SF,AR} \right];\ E_T = \left[E_V + T_R \right] \quad [13]$$

$$P - \left[I_c + I_L + E_T + Q_S + Q_{SF,AR} \right] = \frac{\partial \theta}{\partial t} \quad [14]$$

$$Q = \left[Q_S + Q_{SF,AR} \right] \quad [15]$$

$$Q = P - \left[I_c + I_L + E_T \right] \pm \frac{\partial \theta}{\partial t} \quad [16]$$

Where: In = water inputs (L); Ou = water outputs (L); θ = soil moisture content (L L^{-1}); P= precipitation (L); $I_{C,LS}$ = Interception loss of forest canopy and litter, respectively (L); E_V= Pan evaporation (L); T_R= transpiration (L); Q_S= Surface runoff (L); $Q_{SF,AR}$ = Subsurface runoff and aquifer recharge (L).

Making several further assumptions, the θ is evaluated with very good preliminary expectations as it correlates well with wildfires ($0.34 \leq r^2 \leq 0.95$); tree growth and productivity ($0.40 \leq r^2 \leq 0.50$); pulses of tree dieback ($0.34 \leq r^2 \leq 0.50$) (Návar, 2015). In fact, the best prediction equations of Tables 2 and 3 include θ as the most significant explanatory variable. However, Návar (2015) has found the predictive power of θ weakens as the wildfire time series data lengthens.

D. The proposed conceptual model. Wildfires are associated and significantly synchronized but complex manner with SST oscillations (ENSO, PDO, and AMO) because other local variables such as the availability of fresh foliage and its moisture content also contribute to set the right environmental conditions to unleash these perturbations. Extreme Ocean temperatures beyond average values, dT, are well associated with high-severity 1wildfires and this effect magnifies when all three major SST (ENSO, PDO, AMO) 1anomalies converge over time. As the Oceans warm, the heat waves would eventually 1reach the continents and forest ecosystems, which are from Holartic origin, suffer the consequences through a series of perturbations where the increasing frequency of high-severity wildfires is just one of them.

The ENSO disrupts world climate and it has a profound influence on the precipitation and temperature in many places on Earth, as it is the case for Mexico (Cavazos y Hastenrath, 1990; Méndez-González *et al.*, 2008). In the presence of ENSO, Northern Mexico shifts climate in winter and spring to wetter and colder that correlate very well with the southern displacement of the Lower Aleutian convergence zone in the Northern Pacific Ocean in combination with a stronger Inter-tropical Convergence Zone jet stream of the Central Pacific Ocean (Andrade y Sellers, 1988). Swetnam y Betancourt (1989) in California & Arizona; Drury and Veblen (2007) and Návar (2011) in Durango, México noted the weak but significant synchrony of wildfires with ENSO t+1 events. Due to these conditions, at ENSO t=t, soil moisture content also becomes wetter reducing the risk of high-severity wildfires to nearly 0 and increasing forest productivity (González- Elizondo *et al.*, 2005; Arreola-Ortiz and Návar-Cháidez, 2010; Návar, 2011; 2015).

The joint effect of ENSO, PDO, and AMO on wildfires combines to produce more complex environmental settings (Fig 10). A further explanation of the conceptual framework is given next. These SST oscillations appear to unleash a chain of large-scale bio-climate anomalies in northern forests of Mexico as follows: (i) warming of the Eastern South-Central Pacific Ocean (ENSO, t=t) strengthens Arctic Westerlies (PDO is a good signal) bringing unseasonal winter and spring below average temperatures and above- average precipitation; (ii) as the warm ENSO (t=t+1) Eastern Pacific Ocean current displaces north and arrives in Mexico temperature shifts to above normal and precipitation to below normal that last until the warm Ocean Current migrates or vanishes over time or La Niña takes over the Equatorial Pacific Ocean temperatures; (iii) next seasonal winter and spring climate feature unusual flashy northwestern Ocean waves of frosting air masses or dry flashy intermittent strong arctic cold front systems entering the country controlled partially by the PDO anomaly and probably given by the difference in Ocean temperatures where the two Pacific Ocean currents (ENSO and PDO) meet promoting leaf senescence of frosted foliage of several forest species and adding important amounts of fresh foliage to the forest floor; and (iv) in the presence of a warm-phase AMO, warm Eastern Atlantic air masses (easterlies) arrive in late winter and early spring with air temperatures that depend on the AMO signal and the Gulf Current temperature. Combined warm Equatorial Pacific and Atlantic Ocean currents would bring higher than normal temperatures to the country. Hotspots are good indicators of the convergence of AMO and the Gulf Currents. In addition to high temperatures, the Bermuda-Azores anticyclone strengthens creating the ideal conditions that inhibit precipitation magnifying further the dry spell in most of northern Mexico. Figure 12. The conceptual model for predicting high-severity wildfires in northern forests of Mexico.

Intense flashy frosts usually make several tree species shed an important part of the foliage in the course of weeks; adding important amounts of biomass composed of fresh foliage and branches to the forest floor (Rocha-Loredo and Ramírez-Marcial, 2009; Návar- Cháidez and Jurado-Ybarra, 2009). Warm easterlies temperatures further desiccate fuel loads; set erratic hot-temperature waves of air masses (promoting hotspots in forests) further weakening live forests and frequently promoting tree die off increasing further on-site fuel loads (Allen *et al.*, 2010; Raffa *et al.*, 2010; Návar, 2015). The dry spell intensifies and magnifies in spatial

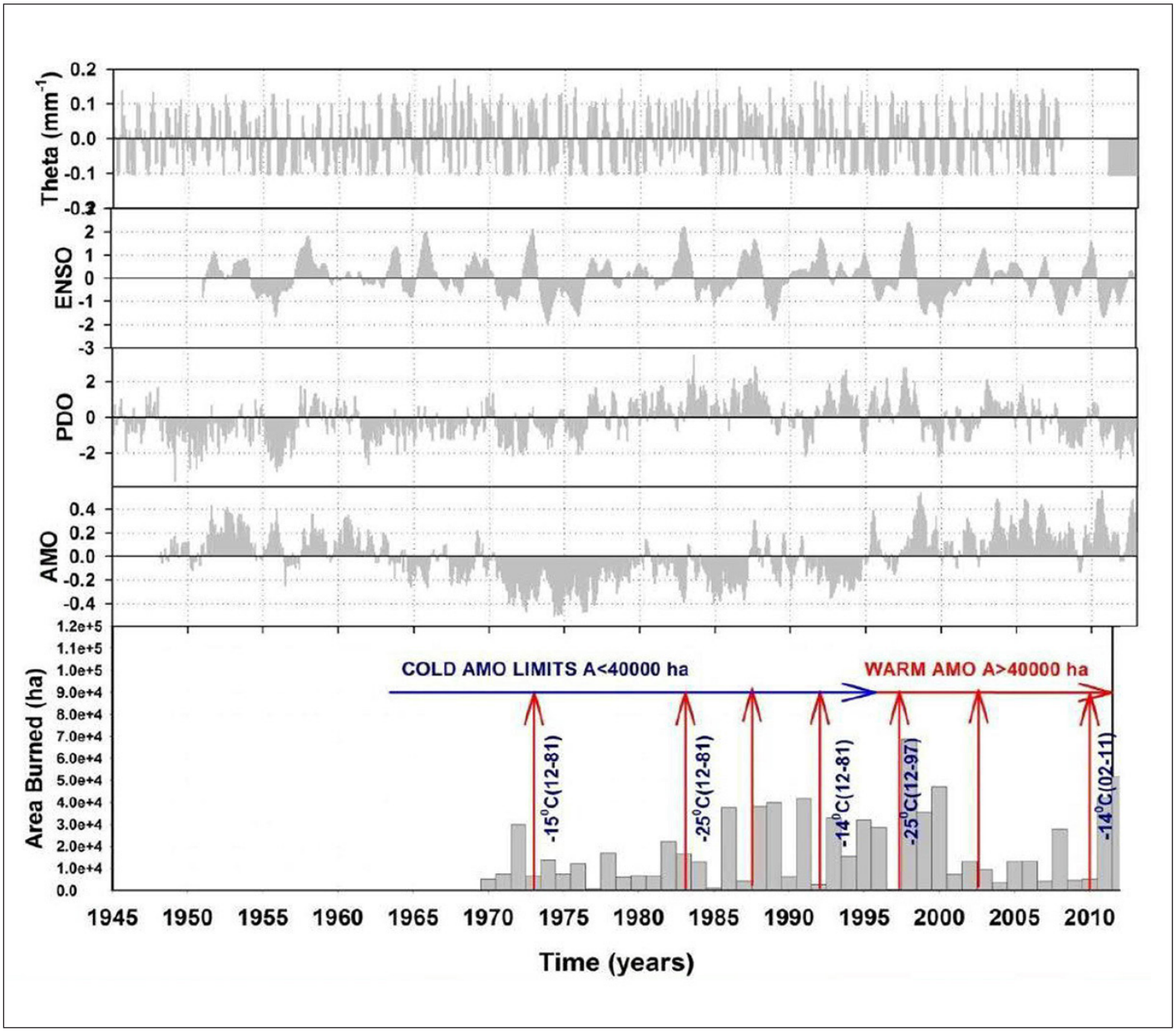

Figure 12. The conceptual model for predicting high-severity wildfires in northern forests of Mexico.

extent drying further any additional fuel load including live trees, shrubs, forbs and grasses. This scenario has repeated several times in the past and set free the presence of important high-severity wildfires in Northern forests of Mexico. Note that when the AMO is in a cold phase (1970-1995), the burned area by wildfires hardly exceeds; A $\leq$ 40,000 ha; in contrast to when it is in a warm phase; A>40,000 ha. Same thing happens to the intensity or failure of each or both the ENSO and PDO anomalies that control part of the wildfire variability. This is the partial reason why any of these SST anomalies alone would account for only a small portion of the wildfire variance.

Wildfires are then a complex function of several bio-climatic processes that can be modeled using most of the mathematical techniques described above. The cycle may start from: (i) modeling the future ENSO anomaly using the conventional ARIMA techniques, large-scale climate models, or NOAA reports; (ii) model the fuel load using the physical model proposed above as well as using the probabilistic or stochastic techniques, yet to be developed, to evaluate the effect of unusual intense frosts (associated with PDO) and hot temperature waves of air masses (associated with AMO) on fresh fuel loads; (iii) use the physical hydrologic mass balance budget model whenever possible to predict the moisture content of the fuel load itself (yet to be developed) or of the forest soil to predict dryness of fuel loads (see Návar, 2015), including the moisture content of live forests; and (iv) prepare for the worst-case scenario by using all the information available.

Discussion

The right hydro-climate conditions that promote high-severity wildfires recorded in the historic data set prevailed in Durango during the most intense ENSO event of the last century (1997-1998) (dT ≥ +2.45°C); combined with AMO (dT ≥ +0.50C) and PDO (dT ≥ +2.0°C) anomalies that caused the record statistic of burned area in Durango (A ≥ 80,000 ha), as elsewhere in the world. These environmental conditions persisted across most forests of the country (CONAFOR, 2012; FAO, 2012). The long-term cycle for the AMO to repeat is from 60 to 80 years (Einfeld *et al.*, 2001); 24 years for the PDO (Mantua, 1999) and 3 to 7 years for the ENSO anomaly (Cavazos and Hastenrath, 1990). The AMO is currently in the warm phase that started in 1997 (**https://www.esrl.noaa.gov/psd/data/correlation/amon.sm.long.data**). The warm phase will likely continue its normal cycle for the next 10 to 15 years dumping warm and probably hot air masses from the Equatorial Atlantic Ocean and strengthening the anticyclone Bermuda-Azores sharpening dry spells with associated hot air masses. Using data from NOAA-US (**https://ggweather.com/enso/oni.htm),** the ENSO is not relaxing; it is in fact fortifying over time as the maximum Eastern South-Central Pacific Ocean temperature deviances, expressed as the Ocean El Niño Index, ONI, are significantly increasing over 31 time: 1957-1958 (dT=+1.7°C); 1965-1966 (dT=+2.0°C); 1972-1973 (dT=+2.05°C); 1982- 32 1983 (dT=+2.25°C); 1997-1998 (dT=+2.40°C); and 2015-2016 (dT=+2.60°C). However, the ENSO long-term cycle is yet to be assessed and the most likely future scenario would be to assume it will continue its rising trend in the years to come. If so, rising seasonal extreme temperatures and precipitation events are expected in the short run as it reinforces the temperature gradient between the arctic and the equatorial Western Pacific Ocean as well as supporting increased temperatures of the ENSO current moving northward across the shoreline of the western coasts of tropical America. The PDO is developing more erratically in modern times (**https://www.ncdc.noaa.gov/teleconnections/pdo/**) from 2005 to 2014 was in a cold phase then it entered into a short warm (2015-2017) to return to a cold phase again (2017-2019). Short-term predictions would be to assume this erratic trend will likely continue.

Under this short run future scenario, northern forests of Mexico would probably experience the most severe wildfires yet to be recorded in modern times in the next 3 ENSO events (20 years) because of the joint presence of extreme positive ENSO and AMO anomalies. However, intensification of high severity wildfire could be limited by only the erratic PDO anomaly should it be in a cold phase when the warmest ENSO and AMO climate signals meet in the near future. However, as the AMO would enter into a cold phase in the next 15-20 years, should the anomaly follow its normal track (returning to below average temperatures), after 30-40 years of a warm phase (Einfeld *et al.*, 2001) wildfire severity would most likely relax returning to a kind of normal severity, A<40,000 ha (See Fig 10 of the wildfire data during the cold phase of AMO). The cold-phase PDO keeps normal or below-average temperatures over Western North America dumping seasonal erratic infrequent cold air masses over Northwestern Mexico in winter and early spring. The partial PDO effect on wildfire can be exemplified next. In spite of this rising trend in temperature deviance, the wildfire severity peaked during the 1997-1998 ENSO event (A≥80,000 ha) even though the 2015-2016 (A=40,000 ha) ENSO event exceeded the temperature deviance of that of 1997-1998. This contrasting finding is explained by the sudden weakening of the PDO entering shortly into a cold phase in 2017-2018. Other factors that may have contributed to keep wildfires in check could be a lack of fresh foliage caused by the absence of extreme cold temperatures; forest fuels were not dry enough; among others. This is a matter of further research in order to forecast the severity of wildfires of the following ENSO events.

Conclusions

This report presents, tests and validates a series of mathematical techniques to predict in advance wildfire data at regional scales. Stochastic and probabilistic models provide from medium to moderately well prediction capabilities. Proposed physical and conceptual model are underway and would probably become the next generation of models that will eventually forecast with higher precision the likelihood of high-severity wildfires. These technologies, as exemplified in this report, predict better fuel loadings and the moisture content than conventional approaches and these techniques would eventually be coupled with the prediction of large scale SST anomalies that have a marked influence on a chain of bio-climatic events unleashing high-severity wildfires in many regions of Earth. These events are proposed to be predicted in advance and coupled into the conceptual framework. These issues are a matter of further research.

References

Acosta Mireles, M. 2003. Diseño y aplicación de un método para medir los almacenes de carbono en sistemas con vegetación forestal y agrícolas de ladera en México. Tesis Doctoral. Colegio de Postgraduados. Montecillo, México. 99 p.

Aguado, I., E. Chuvieco, P. Martin y F.J. Salas. 2003. Assessment of forest fire danger conditions in southern Spain from NOAA images and meteorological indices. International Journal Remote Sensing 24: 1653-1668.

Aguirre-Bravo, C. 1987. Stand average and diameter distribution growth and yield models for natural uneven-aged stands of Pinus cooperi. Ph.D Dissertation. Colorado State University. Forth Collins, CO. USA.

Allen, C.D., Macalady, A.K., Chenchouni, H., Bachelet, D., McDowell, N., Vennetier, M., Kitzberger, T., Rigling, A., Breshears, D., Hoggi, E.H., Gonzalez, P., Fensham, R., Zhang, Z., Castro, J., Demidova, N., Lim, J.H, Allard, G., Running, S.W., Semerci, A., and Cobb, N. 2010. A global overview of drought and heat-induced tree mortality reveals emerging climate change risks for forests. Forest Ecology and Management 259: 660-684.

Alvarado, E., D.V. Sandberg y S.G. Pickford. 1998. Modeling large forest fires as extreme events. Northwest Science 72: 66-75.

Andrade, A.R. and Sellers, W.D. 1988. El Niño and its effect on precipitation in Arizona and Western New Mexico. Journal of Climatology 8: 403-410.

Aryal, D., Gómez-Castro, H., García, N., Ruiz, O., Molina, L., Jiménez, J., Venegas, J. Pinto, R., Ley, A., Guevara, F. 2018. Potencial de almacenamiento de carbono en areas forestales en un sistema ganadero. Revista Mexicana de Ciencias Forestales. DOI: **https://doi.org/10.29298/rmcf.v8i48.184**.

Bugalho, L. y L. Pessanha. 2007. The forest fire risk index (ICRIF) operational process and validation. En '4a Conferencia Internacional sobre Incendios Forestales'. Organismo Autónomo de Parques Ncionales. Ministerio del Medio Ambiente. Sevilla, España. Pp. 8.

Caballero-Cruz, P., Santiago-Juárez, W., Martínez-Santiago, D., Cruz-Santiago, O., Pérez Silva, E., Aguirre, O. A. 2018. Combustibles forestales y susceptibilidad a incendios de un bosque templado en la Mixteca Alta, Oaxaca, México. Foresta Veracruzana. 20: 1-10.

Cavazos, T y S. Hastenrath. 1990. Convection and rainfall over Mexico and their modulation by the Southern Oscillation. International Journal of Climatology 10: 377-386.

CONAFOR (Comisión Nacional Forestal). 2012. Reporte nacional de incendios forestales. Publicación interna de trabajo. Conafor. Guadalajara, Mex. Disponibleen **http://www.mexicoforestal.gob.mx/files/120427%20reporte%20nacional%20incendios.pdf** (Último acceso mayo 12, 2012).

Corral-Rivas, S., and Návar-Chaidez, J.J. 2005. Analisis del crecimiento e incremento de cinco pinaceas de los bosques de Durango. Mexico. *Madera y Bosques* 11: 29-47.

Drury, S.A. y T.T. Veblen. 2007. Spatial and temporal variability in fire ocurrent within the Las Bayas Forestry Reserve, Durango, Mexico. Plant Ecology 197: 299-316.

FAO. 2012. Food and Agriculture Organization. United Nations. Forest Wildfire in the World. Rome Italy.

Fiorucci, P., F. Gaetani y R. Minciardi. 2004. Sistema integrado para evaluar el riesgo estático y dinámico a nivel nacional de incendios forestales. En '2nd Symposium on FIRE, Economics, Planning and Policy: A Global View'. Córdoba, España. Pp 1-20.

Fernandes, P.M., Loureiro, C., Magalhaes, M., Ferreira, P., Fernandes, M. 2012. Fuel age, weather and burn probability in Portugal. International Journal of WIldland Fire 454 **http://doi.org/10.1071/WF10063**.

Fulé, P.Z. and W.W. Covington. 1997. Fire regimes and forest structure in the Sierra Madre Occidental, Durango, Mexico. Acta Botánica Mexicana 41: 43-79.

Fulé, P.Z. and W.W. Covington. 1999. Fire regime changes in La Michilia Biosphere Reserve, Durango, Mexico. Conservation Biology 13(3):640-652.

García, E. 1987. Modificaciones al sistema de clasificación climática de Koppen (para adaptarlo a las condiciones de la República Mexicana). 4ª Edición. Instituto de Geografía, UNAM. México. 217 p.

Haan, C.T. 2003. Stochastic Models in Hydrology. Iowa State University Press. 3rd Edition. Iowa. USA.

Hernández-Leal, P.A., M. Arbelo y A. González-Calvo. 2005. FIRE risk assessment using satellite data. Advances in Space research 37: 741-746. **http://fire.cfs.nrcan.gc.ca**. 12. Diciembre de 2010. **https://www.esrl.noaa.gov/psd/data/correlation/amon.sm.long.data** August 2019. **https://ggweather.com/enso/oni.htm** August, 2019. **https://www.ncdc.noaa.gov/teleconnections/pdo/** August 2019. **https://www.cpc.ncep.noaa.gov.** 2018.

Johnson, E.A. y K. Miyanishi. 2001. Forest fires. Behaviour and ecological effects. San Diego, Academic Press. USA. 412 p.

Kohl, M., Lasco, R., Cifuentes-Jara, M., Jonnson, O., Korhonen, K.T., Mundhenk, P., Návar, J.J., and Stinson, G. 2015. Changes in forest production, biomass and carbon: Results from the 2015 UN FAO Global Forest Resource Assessment. Forest Ecology and Management 352: 21-34.

Lawson, B.D, G.N. Dalrymple y B.C. Hawkes. 1997. Predicting forest floor moisture contents from Duff Moisture Code values. Canadian Forest Service, Pacific Forestry Centre, Victoria, BC. Technology Transfer Note 6.

Mendoza-Ponce, A., and Galicia, L. 2010. Aboveground and belowground biomss and carbon pools in highland temperate forest landscape in Central Mexico. Forestry: An International Journal of Forest Research 83: 497-506.

Navar, J. 2009. Allometric equations for tree species and carbon stocks for forests of northwestern Mexico. Forest Ecology and Management doi:10.1016/j.foreco.2008.09.028.

Návar-Cháidez, J.J., and L.G. Lizárraga-Mendiola. 2013. Hydro-climatic variability and forest fires in Mexico's northern temperate forests. *Geofísica Internacional* 52: 5–20 **https://doi.org/10.1016/S0016-7169(13)71458-2**.

Návar, J. 2015. Hydro-climatic variability and perturbations in Mexico's northwestern temperate forests. Ecohydrology DOI: 10.1002/eco.1564.

Návar, J. 2019. Modeling litter stocks and accumulation rates in planted forests of northern Mexico. Submitted to Geoderma.

Návar, J., Rodriguez-Flores, F.J., Domínguez-Calleros, P.A. 2013. Taper functions and merchantable timber for temperate forests of northern Mexico. *Annals of Forest Research 56(1)*, 3-15.

Newnham, R.M. 1990. Variable-form taper functions for four Alberta tree species. *Canadian Journal of Forest Research, 22*, 210-223.

Oliver, C.D. y B.C. Larson. 1996. Forest stand dynamics. McGraw Hill. Nueva York, 509 p.

Pérez-Verdin, G., M.A. Márquez-Linares, A. Cortés-Ortiz, and M. Salmerón-Macías. 2013b. Análisis espacio-temporal de la ocurrencia de incendios forestales en Durango, México. *Madera y Bosques* (2): 37–58 **https://doi.org/10.21829/myb.2013.192339**

Reinhardt, E., and Crookston, N.L. 2003. The fire and fuels extension to the forest vegetation simulator. Gen. Tech. Rep. RMRS-GTR-116. USDA FS. Odgen, Utah.

Renteria, J.B., E.J. Trevino, J.J. Navar, O.A. Aguirre and I. Cantu, 2005. Woody fuel assessment in Ejido Pueblo Nuevo, Durango. Revista Chapingo, 11: 51-56.

Rodriguez-Laguna, R., Jiménez, J., Aguirre, O., Treviño, E., and Raso, R. 2009. Estimación de carbono almacenado en el bosque de pino-encino en la Reserva de la Bipsfera El Cielo, Tamaulipas, México. Ra Himhai 5: 317-327.

Rodríguez-Trejo, D.A. 1996. Incendios forestales. Mundi Prensa-Universidad Autónoma Chapingo-División de Ciencias Forestales y del Ambiente-Instituto Nacional de Investigaciones Forestales y Agropecuarias. México, D. F. 630 pp. Rodríguez-Trejo, D.A. y P.Z. Fulé. 2003. Fire ecology of Mexican pines and fire management proposal. International Journal of Wildland Fire 12:23-37.

Rodríguez-Trejo, D.A. 2008. Fire regimes, fire ecology and fire management in México. *AMBIO: A Journal of the Human Environment* (7): 548–556 **https://doi.org/10.1579/0044-7447-37.7.548**.

Rodríguez-Trejo, D.A. 2015. *Incendios de vegetación: su ecología, manejo e historia.* México. Chapingo: Colegio de Post Graduados [In Spanish]. Sebastián L.A., R.E. Burgan, A. Calle y A. Palacios-Orueta. 2007. Calibration of the fire potential index in different seasons and bioclimatic regions of southern Europe. En '4a Conferencia Internacional sobre Incendios Forestales'. Organismo Autónomo de Parques Nacionales. Ministerio del Medio Ambiente. Sevilla. España.

Sebastián L.A., J. San Miguel-Ayanz y G. Libertá. 2000. An integrated forest fire risk index for Europe. En '20th EARSeL Symp: Remote Sensing in the 21st Century: A decade of trans-European remote sensing cooperation'. Dresden, Germany. Pp 137- 142.

Sebastián L.A., G. Libertá y J. San Miguel-Ayanz. 1999. An integrated forest fire risk index for European regions. Fire Potential Index. Joint Research Centre. www.etsea2.ud1.es.

Shlisky, A., J. Waugh, P. González, M. González, M. Manta, H. Santoso, E. Alvarado, A. Ainuddi-Nuruddin, D.A. Rodríguez-Trejo, R. Swaty, D. Schmidt, M. Kaufmann, R. Myers, A. Alencar, F. Kearns, D. Johnson, J. Smith y D. Zollner. 2007. Fire, ecosystems and people: Threats and strategies for global biodiversity conservation. The Nature Conservancy Global Fire Initiative Technical Report 2007-2. IV Conferencia Internacional sobre Incendios Forestales. Sevilla, España. 13-17 de mayo de 2007.

Swetnam, T.W. y J.L. Betancourt. 1989. El Niño-Southern Oscillation (ENSO) phenomena and forest fires in the Southwestern United States. In J.L. Betancourt and A.M. MacKay, editors, 1990. Proceedings of the Sixth Annual Pacific Climate (PACLIM) Workshop. March 5-8, 1989. California Department of Water Resources, Interagency Ecological Studies Program. Technical Report 23. Vega-Nieva, D.J., Nava-Miranda, M.G., Calleros-Flores, E. et al. fire ecol (2019) 15: 28. **https://doi.org/10.1186/s42408-019-0042-z** .

Geofísica Internacional (2023) **62-3**: 581 - 590

Assessment of Indoor/outdoor Particulate Matter in Residential Building: Tehran Metropolis, Iran

Balal Oroji[1]*

Abstract

Indoor Air Quality and the prediction of indoor pollution levels have become more important subjects for health risks. This research will be investigated the ratio of the concentration of particles inside and outside residential houses in Tehran. The particulate matter (PM) sampling was performed in four seasons from August 2020 to July 2021. Four stations were selected as fixed sampling stations and sampling time varied from 6 hours to 12 hours. Due to the risk of fine particles and the possibility of their impact on human health, in this study, $PM_{0.4}$ and $PM_{2.5}$ were examined. A multi-stage virtual shock absorber that traps particles on steel plates with a constant airflow was used for sampling. The Scanning Electron Microscope (SEM) and Inductively Coupled Plasma-Mass Spectrometry (ICP-MS) methods were used to study the size, morphology, and chemical composition and analyze the total concentration of particulate matter (PM). The results showed that in most stations, the penetration of outdoor particles into the building in the cold season was more than in the hot season. Due to the use of natural ventilation in most residential buildings in the study area, the I/O ratio of $PM_{2.5}$ and $PM_{0.4}$ was on average more than 0.752. At some stations in March, April, and May the I/O ratio was over 0.965. According to these results, in the eastern area, the exposure to particulate matter (PM) with a diameter of less than 0.4 µm was higher than in other areas.

Also, the results showed that the average effect of the ventilation factor in the studied area for the whole year was about 38.4%. Meanwhile, this amount was 19.4 and 13% for the factors of cooking and activity, respectively. The average effect of factors of building age and smoking were 7.6 and 21.6%, respectively. The results of the SEM method showed that the penetration of pollutants outdoor the building has a great effect on the concentration of particles indoor.

Key words: Residential Building; Indoor/Outdoor concentration; $PM_{0.4}$; $PM_{2.5}$; SEM

Resumen

La calidad del aire interior y la predicción de los niveles de contaminación interior se han convertido en temas más importantes para los riesgos para la salud. Esta investigación se investigará la proporción de la concentración de partículas dentro y fuera de las casas residenciales en Teherán. El muestreo de material particulado (PM) se realizó en cuatro temporadas desde agosto de 2020 hasta julio de 2021. Se seleccionaron cuatro estaciones como estaciones de muestreo fijas y el tiempo de muestreo varió de 6 horas a 12 horas. Debido al riesgo de partículas finas y la posibilidad de su impacto en la salud humana, en este estudio se examinaron $PM_{0.4}$ y $PM_{2.5}$. Para el muestreo se utilizó un amortiguador virtual de etapas múltiples que atrapa partículas en placas de acero con un flujo de aire constante. Se utilizaron los métodos Microscopio Electrónico de Barrido (SEM) y Espectrometría de Masas de Plasma Acoplado Inductivamente (ICP-MS) para estudiar el tamaño, la morfología y la composición química y analizar la concentración total de material particulado (PM). Los resultados mostraron que en la mayoría de las estaciones, la penetración de partículas exteriores en el edificio en la estación fría fue mayor que en la estación cálida. Debido al uso de ventilación natural en la mayoría de los edificios residenciales del área de estudio, la relación I/O de $PM_{2.5}$ y $PM_{0.4}$ fue en promedio superior a 0.752. En algunas estaciones en marzo, abril y mayo, la relación I/O fue superior a 0.965. De acuerdo con estos resultados, en el área oriente, la exposición a material particulado (PM) con un diámetro menor a 0.4 µm fue mayor que en otras áreas. Asimismo, los resultados mostraron que el efecto promedio del factor de ventilación durante el año fue del orden del 38.4%. En tanto, esta cantidad fue de 19.4 y 13% para los factores de cocción y actividad, respectivamente. El efecto promedio de los factores de vida del edificio y tabaquismo fue de 7.6 y 21.6%, respectivamente. Los resultados del método SEM mostraron que la penetración de contaminantes en el exterior del edificio tiene un gran efecto sobre la concentración de partículas en el interior.

Palabras clave: Edificio residencial; Concentración interior/exterior; PM≤0,4; PM2,5; SEM/EDX

Received: July 26, 2022 ; Accepted: March 12, 2023 ; Published on-line: July 1, 2023.

Editorial responsibility: Dra.Ofelia Morton-Vermea

* Corresponding author: Balal Oroji

[1] Water, Energy and Environment Center, Faculty and Research Institute of Civil Engineering, Water and Energy, Imam Hossein Comprehensive University, Tehran, Iran. E-mail: Balaloroji@yahoo.com Tel: +98 918 819 0443 Fax: +98 21 741 685 25

https://doi.org/10.22201/igeof.2954436xe.2023.62.3.1714

Introduction

$PM_{2.5}$ emission is known as a major challenge to environmental health and is the cause of approximately 7 million deaths annually (Alikhani *et al.* 2021). Epidemiological research has shown that $PM_{2.5}$ will be a serious threat to human health (Ortega-Rosas *et al.* 2021; Thangavel *et al.* 2022). Based on this research, $PM_{2.5}$ has been shown to damage the cardiovascular system, nervous system, respiratory system and immune system and so on (Du *et al.* 2016; Yang *et al.* 2020). This can seriously affect long-term economic, social, welfare and national health development (Ranft *et al.* 2009; Lim *et al.* 2011; Meza-Figueroa *et al.* 2022). PM is one of the primary air pollutants that pose a constant threat to health, well-being and quality of life. These compounds are composed of a complex mixture of chemical, physical and biological components (Schneider *et al.* 2015; Schneider *et al.* 2016; Ramirez *et al.* 2020; Rojas *et al.* 2019; Hu *et al.* 2020; Mellouki *et al.* 2020; Silva *et al.* 2020a; Silva *et al.* 2020b; Zamberlan *et al.* 2020; Schiavo *et al.* 2021). The fine particles stay in the atmosphere longer than coarse particles, so these can enter the respiratory system very quickly (Juginović *et al.* 2021). Due to their aerodynamic properties, these particles can be easily removed during the wet and dry deposition process. The fine particles are also able to be easily transported through the respiratory system by penetrating the pulmonary alveoli and thus lead to pulmonary deposition and systemic displacement (Schiavo *et al.* 2021).

The results of studies in this field have shown that long-time exposure to atmospheric particles leads to complications and various respiratory and lung diseases (Xiao *et al.* 2016; Bourdrel *et al.* 2017; Liu *et al.* 2020; Moller *et al.* 2020; Gao and Sang 2020; Nho 2020; Schiavo *et al.* 2021; Zhao *et al.* 2022; Voss *et al.* 2022). Also, recent studies show that fine particles (diameter less than 2.5 μm) and ultrafine particles (diameter less than 0.1 μm) are the most toxic airborne particles (Xiao *et al.* 2016; Soppa *et al.* 2019). Depending on the source of the contamination, the PM varies in size and composition. Major sources of primary particles are industrial processes, traffic characteristics (i.e. traffic volume and percentage of gasoline and diesel vehicles) and topography, biomass burning (as agricultural products incineration, forest and range fires and Garbage disposal), road traffic, power plants, domestic burning (coal, wood, etc.), incineration, and resuspension of road and construction dust. (Dias *et al.* 2014; Goel and Kumar 2015; Dalmora *et al.* 2016; Kecorius *et al.* 2016; Abramesko and Tartakovsky 2017; Chen *et al.* 2017; Habre *et al.* 2018; Islam *et al.* 2019; Stacey 2019; Moller *et al.* 2020; Agudelo-Castaneda *et al.* 2019; Li *et al.* 2021). Due to the differences in air quality in different regions (like some cities in Europe, North America and China), many studies inside and outside the country have examined factors that are closely related to changes in air quality, such as meteorological conditions, changes in surface coverage, urbanization and economic development, transportation methods and urbanization (Oroji *et al.* 2018b; Oroji *et al.* 2019; Zhao *et al.* 2020; Isaev *et al.* 2022; Domhagan *et al.* 2022). Therefore, further investigations into the impacts on health effects of short-term and long-term exposures to urban air pollution are warranted. One of the indicators which are widely used for evaluating the impacts of indoor pollution resulting from outdoor pollution is the ratio of indoor to outdoor (I/O ratio) air pollution (I/O ratio) (Meng *et al.* 2005; Brunekreef *et al.* 2005).

Some factors, such as distance from polluting resources, smoking, cooking, climate, the life of the building, and its architectural characteristics can affect indoor air pollution which is resulted from outdoor air pollution (Ji *et al.* 2015; Parajuli *et al.* 2016; Zhou *et al.* 2018). Several studies have been conducted to measure the PM concentration and levels of exposure to particle in indoor air. Branis and Šafránek (2005), investigated the mass concentration, mineral composition, and morphology of suspended particles re-emitted by children during scheduled physical exercise in urban, suburban, and rural elementary school gymnasiums in Prague (Czech Republic). Oroji *et al.* (2021) investigated the penetration and deposition of indoor particles and found that the penetration of indoor particles is determined by particle size and air tightness. Bhangar *et al.* (2011) investigated the sources of and daily exposure to indoor and outdoor particle by measuring ultrafine particles in houses in California. This research revealed that residential exposure to particle was determined by indoor sources and the infiltration factor. Mullen *et al.* (2011) measured the ultrafine particles in elementary schools in California and found that the main cause of particle exposure was outdoor sources.

The metropolis of Tehran, the capital of Iran, is one of the most polluted cities in the region and the world, and increasing the concentration of PM is one of the biggest challenges for its inhabitants. A significant volume of atmospheric particle concentrations in Tehran is related to human resources, which are produced by motor vehicles, industrial factories, and home heating systems. Another part of the source of atmospheric particles in Tehran is local storms (Heger and Sarraf 2018). In recent years increased personal vehicle traffic in the city and the construction of high-rise buildings have raised the concentration of atmospheric particles in the area to dangerous levels and drastically reduced the air quality (Oroji 2018a; Oroji 2021). In this study, we intend to determine the I/O ratio in residential houses by examining the concentration of particles inside and outside. Because so far, the amount of exposure of people living in homes in Tehran with suspended particles has not been calculated. Study and research in the field of physical and chemical

properties of suspended particles, identifying their behavior in different climatic conditions and recognizing the sources that produce them can improve decisions about air pollution control and management.

Methods and Materials

Area of study

The city of Teheran (capital of Iran), located on the southern slops of the Alborz Mountains with and area of about 73 km^2, is one of the most populous metropolises in the world with a population of about 15 million people (Arhami *et al.* 2018). The geographical location of the study area is shown in Figure 1. Population growth, land cover, land-use change and, most importantly, a significant increase in the number of moving pollutants (motor vehicles) have led to an increase in air pollution, which has posed significant risks to the ecosystem and human health and safety (Alizadeh Choobari *et al.* 2016). In the last decade, air pollution, including the presence of PM, are recognized as the most important environmental problem in Tehran. Local storms, industries (such as manufacturing industries, electricity generation with fossil fuels and sand mines), urban transport (such as motor vehicle) and soil erosion are the most are the most important sources of pollution in Tehran. The geographic location and prevailing wind direction (specify wind direction in Teheran) limits natural ventilation, increase Temperature inversions in wet seasons and the effects of local dust storms (Halek *et al.* 2010a; Halek *et al.* 2010b).

Sampling method

Atmospheric PM sampling was performed in four seasons from August 2020 to July 2021. Due to the area, four fixed sampling station were used. Sampling time varied from 6 to 12 hours. The sampling process was performed to determine the concentration of particles inside while people were at home. Sampling stations were between 250 and 600 meters from the first huge traffic street. Also, the age of the buildings at the sampling stations was between 12 and 19 years. More than 98% of the particles are less than 1 µm. They can advance far more deeply into the human organism and even pass alveoli and cellular membranes. In this way, they reach the blood circulation directly, where they are frequently triggering cardiovascular illnesses. They arise mostly in the case of combustion processes (e.g., traffic, heating systems) and with industrial processes (e.g., production, power generation) and are not visible to the human eye (Juginović *et al.* 2021). Due to the risk of fine particles and the possibility of their impact on human health, in this study, $PM_{0.4}$ and $PM_{2.5}$ were examined. A multi-stage virtual shock absorber that traps particles on steel plates with a constant airflow was used for sampling. The sampling airflow in this collector was 28.3 liters per minute. The fiberglass filters were used to collect suspended particles. The collected samples were prepared for chemical analysis. Also, the Scanning Electron Microscope (SEM) method was used to study the size and morphology of suspended particles. In this method, particle surfaces with magnifications of 5000x, 10000x, 20000x and 50000x were studied. The particles were imaged a Zeiss EV050XP SEM, and also, X-ray energy spectra were measured using a Bruker Quantax 200 EDS system with a Peltier-cooled X Flash silicon detector. The Inductively coupled plasma-mass spectrometry (ICP-MS) method was used to study the chemical composition of PM.

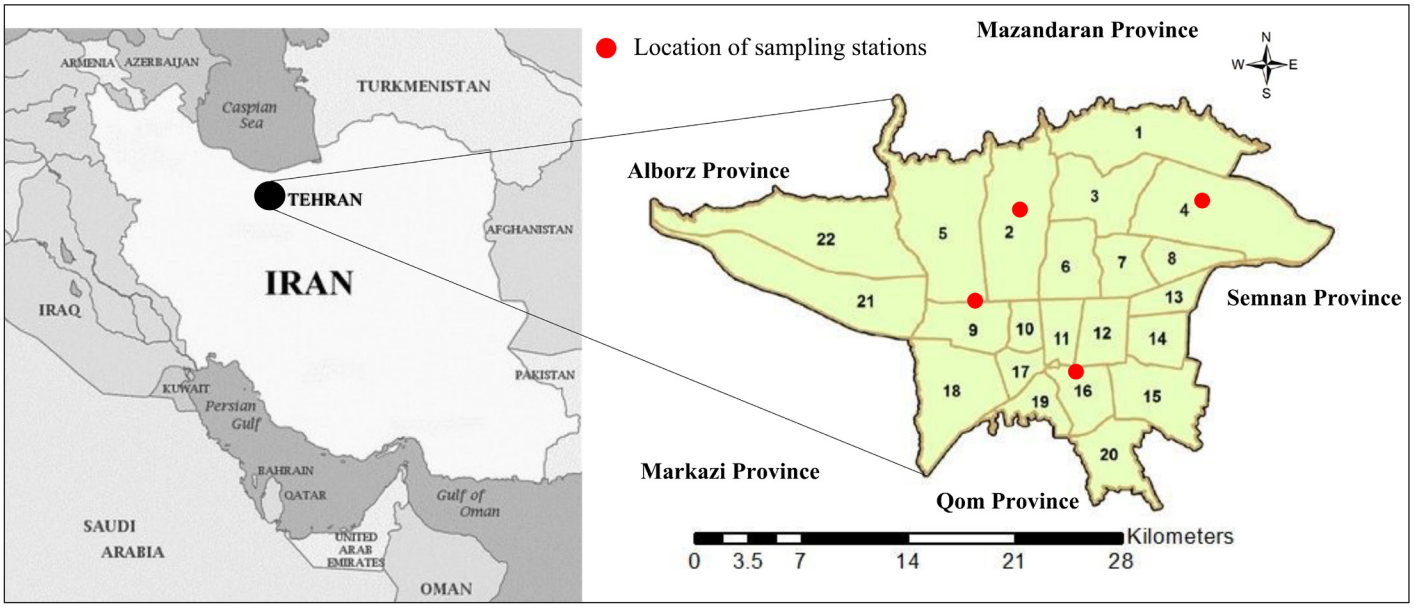

Figure 1. Geographical location of the study area.

Results and Discussion

Outdoor Particle Concentration

Table 1 shows the monthly report of PM concentrations in stations in the study area. According to the measurement results in the Velenjak station, the highest concentration of $PM_{2.5}$ was 161±24.6 μg/m^3 that recorded in October. Also, the lowest concentration was recorded at 25±4.3 μg/m^3, in November. The average of $PM_{2.5}$ in this area was 75±11.1 and 69.9±12.6 μg/m^3 for the dry months (June to November) and wet months (December to May), respectively. The results of the aerodynamic distribution of particles in this area showed that in hot and dry months (such as August and September), the highest and lowest average concentrations of $PM_{0.4}$ in this area were recorded at 11.2±1.3 and 10.1±1.1 μg/m^3, respectively. For cold and wet months (such as December and January), the highest and lowest average concentrations of $PM_{0.4}$ in this area were recorded at 16.3±2.6 and 8.4±1 μg/m^3, respectively. The average concentration of $PM_{2.5}$ and smaller for the whole sampling period in this area was 72.74±15.4 μg/m^3. The results of measurement at the Azadi square station showed that the highest concentration of $PM_{2.5}$ was 187±25.6 μg/m^3 that recorded in November. Also, the lowest concentration was recorded at 55±14.5 μg/m^3, in February. The average concentration of $PM_{2.5}$ was 109.5±17.4 and 127.27±21.7 μg/m^3 for the dry months and wet months, respectively. The results of the aerodynamic distribution of particles in this area showed that in hot and dry months, the highest and lowest average concentrations of $PM_{0.4}$ in this area were recorded at 26.6±4.4 and 13.2±2.1 μg/m^3, respectively. Also, for cold and wet months, the highest and lowest average concentrations of $PM_{0.4}$ in this area were recorded at 18.1±2.3 and 9.1±1.2 μg/m^3, respectively. The results showed that the average concentration of $PM_{2.5}$ was 117.4±19.5 μg/m^3. In the South station, the highest and lowest concentration of $PM_{2.5}$ was 160±18.6 and 41±6.8 μg/m^3, which were recorded in December and January, respectively. Also, the average concentration of $PM_{2.5}$ was 90.4±16.7 and 85.1±15.2 μg/m^3 for the dry months and wet months, respectively. The results showed that in hot and dry months, the highest and lowest average concentrations of $PM_{0.4}$ in this area were recorded at 19.2±3.6 and 14.6±3.3 μg/m^3, respectively. Also, the highest and lowest average concentration of $PM_{0.4}$ for cold and wet months, were recorded at 17.8±2.2 and 10.3±2.1 μg/m^3, respectively. The average concentration of $PM_{2.5}$ was 87.9±19.4 μg/m^3. Based on the sampling results in the Hakimiyeh station, the highest concentration of $PM_{2.5}$ was 153±18.4 μg/m^3 that recorded in December. While the lowest concentration was recorded at 28±4.4 μg/m^3, in November. Also, the average concentration of $PM_{2.5}$ in this area was 79.81±12.6 and 70.62±14.8 μg/m^3 for the dry months and wet months, respectively. The results of the aerodynamic distribution of particles in this area showed that in hot and dry months, the highest and lowest average concentrations of $PM_{0.4}$ in this area were recorded at 13.4±1.6 and 11.6±2.4 μg/m^3, respectively. Also, for cold and wet months, the highest and lowest average concentrations of $PM_{0.4}$ in this area were recorded at 16.8±2.3 and 11.4±1.2 μg/m^3, respectively. The average concentration of $PM_{2.5}$ for the whole sampling period in this area was 76.5±18.5 μg/m^3.

Indoor Particle Concentration

The results of indoor particle concentration are showed in Table 2. In residential houses in the northern areas of the city, due to excessive use of natural ventilation in the cold months, smoking, and cooking, see a significant increase in indoor suspended particles. Meanwhile, the houses in this area are

Table 1. Monthly report of particle concentrations Outdoor in the study area (μg/m^3).

Date	Velenjak		Hakimiyeh		Azadi squar		South	
	$PM_{0.4}$	$PM_{2.5}$	$PM_{0.4}$	$PM_{2.5}$	$PM_{0.4}$	$PM_{2.5}$	$PM_{0.4}$	$PM_{2.5}$
April 2021	13.5	73.87	12.2	67.1	13.2	97.77	11.8	85.58
May 2021	13.3	67.71	11.6	54.96	13.1	96.67	12.3	77.22
June 2021	14.8	69.4	12.8	68.56	12.4	106.51	13.5	78.78
July 2021	15.7	83.9	14.1	79.75	15.7	123.46	14.7	93.41
August 2020	14.3	72.41	15.3	66.21	17.6	107.11	16.3	70.96
September 2020	14.6	84.5	17.8	77.54	17.2	122.8	17.2	84.71
October 2020	11.2	73.46	10	81.63	13.4	121.16	11.1	90.6
November 2020	11.5	61.83	10.7	67.92	12.2	119.61	11.5	82.56
December 2020	10.4	84.93	9.5	105.1	11.8	153.13	10.4	119.48
January 2020	8.2	67.65	7.2	85.66	11.7	124	10.2	97.1
February 2020	8.7	59.6	7.6	78.96	9.3	117.4	8.7	86.92
March 2020	9.3	58.7	7.4	77.56	9.2	102.47	8.5	86.64

equipped with modern cooling, heating, and air conditioning systems. At Velenjek station, the average concentration of fine particles ($PM_{2.5}$) for spring was 48.74±9.4 μg/m^3. The concentration was higher than other stations. The highest concentration was recorded in the spring for Azadi station with a value of 68.21±7.5 μg/m^3. This value was 10.65±2.35 μg/m^3 for $PM_{0.4}$. According to the results, the increasing trend in the concentration of indoor particles in the warm months of the year was more than in the cold months of the year. These changes were significant in residential homes that an adequate ventilation. In residential houses that did not have proper cooling and ventilation systems, the I/O value was close to 1. This increase in concentration in 22.5% of residential homes was due to the type of cooking in the kitchen as well as smoking. In the Hakimiyeh station, the concentration of indoor particles was not much different from the concentration of outdoor particles in the building. The mean Pearson correlation coefficient (r) was 0.785. Also, in the northern areas (such as Velenjak station), due to the difference in temperature and relative humidity, the lowest difference between the concentration of outdoor and indoor particles was observed. The concentration of indoor particles in South station was less different from the concentration of outdoor particles. At this station, the average $I/OPM_{2.5}$ was 0.732. While this value was about 0.788 for $PM_{0.4}$.

Indoor/Outdoor Particle Concentration

The results indoor/outdoor particle concentration ratio are shown in Table 3. The results showed that the indoor/outdoor particles concentration ratio is high (~1) in the study area. This rate (I/O) was higher in the cold and wet months of the year in northern areas. Also, in the southern area (Southern station) concentration of the indoor/outdoor particles was high in most months of the year. Using natural ventilation instead of mechanical ventilation is the main factor for the high indoor/outdoor particle concentration ratio. Field research in these areas showed that many residential houses use natural systems for air conditioning. Also, the life of the building, long life of doors and windows, cooking and cigarette smoke are the factors that cause high indoor/out-

Table 2. Average Concentration of the size distribution of the indoor.

Stations	Diameter Particle (μm)	Concentration (μg/m^3)			
		Spring	Summer	Autumn	Winter
Hakimiyeh	$PM_{0.4}$	8.22	9.2	10.34	6.25
	$PM_{2.5}$	52.15	49.54	55.61	50.45
South	$PM_{0.4}$	9.13	10.22	12.45	8.64
	$PM_{2.5}$	53.17	60.55	60.16	55.34
Velenjak	$PM_{0.4}$	7.56	8.32	9.22	5.76
	$PM_{2.5}$	48.74	45.24	50.46	45.62
Azadi square	$PM_{0.4}$	8.82	9.73	10.31	7.14
	$PM_{2.5}$	52.63	58.56	58.25	50.42

Table 3. Monthly reporting indoor/outdoor particle concentration ratio in the study area.

Date	Velenjak		Hakimiyeh		Azadi square		South	
	$I/OPM_{0.4}$	$I/OPM_{2.5}$	$I/OPM_{0.4}$	$I/OPM_{2.5}$	$I/OPM_{0.4}$	$I/OPM_{2.5}$	$I/OPM_{0.4}$	$I/OPM_{2.5}$
April 2021	0.78	0.62	0.87	0.72	0.83	0.77	0.87	0.72
May 2021	0.81	0.64	0.82	0.64	0.84	0.78	0.85	0.76
June 2021	0.82	0.68	0.75	0.68	0.81	0.68	0.82	0.78
July 2021	0.72	0.64	0.71	0.67	0.8	0.58	0.84	0.71
August 2020	0.71	0.58	0.68	0.65	0.82	0.72	0.77	0.68
September 2020	0.68	0.55	0.66	0.76	0.75	0.67	0.76	0.67
October 2020	0.67	0.43	0.71	0.67	0.74	0.71	0.72	0.72
November 2020	0.65	0.47	0.7	0.66	0.73	0.7	0.74	0.77
December 2020	0.55	0.57	0.65	0.68	0.72	0.72	0.67	0.71
January 2020	0.74	0.58	0.66	0.72	0.76	0.68	0.67	0.77
February 2020	0.75	0.63	0.72	0.73	0.68	0.8	0.88	0.87
March 2020	0.8	0.7	0.8	0.77	0.78	0.83	0.87	0.85

door particles concentration ratio in these areas. The eastern regions of the study area, due to being in the direction of the prevailing wind direction, are more affected by atmospheric PM. Based on these results, the concentration of PM with a diameter of less than 0.4 µm in these areas was higher than in other stations. Accordingly, the ratio of I/O was higher in the eastern area than in other areas. Due to the concentration of PM produced by pollutant sources in the western parts of the study area, the ratio of I/O was at a high level. The I/O ratio in spring was close to 1 in all stations. This ratio was higher for particles with a diameter of 0.4 µm (more than 2.5 µm). Also, the results showed that the penetration of particles produced from external pollutants into residential houses is high. So, people living in the area are likely to be exposed to PM for a long time. These conditions can cause respiratory and cardiovascular diseases.

Morphology and Chemical Composition of Particles

Figure 3 shows the SEM image of indoor/outdoor particles collected in the study area. The results of SEM analysis of the samples showed that most of the particles are irregular, fibrous and spherical in shape as well as crystalline shapes. Most of the elements in the samples taken in this area include Chlorine (Cl), Calcium (Ca), Iron (Fe), and Potassium (K), which are found in combination with Zinc (Zn). In the samples of these areas, crystalline, spherical and amorphous shapes are seen in particles with diameter less than 2 µm with compounds rich in Oxygen (O), Fe, Silicon (Si) and Titanium (Ti) along with Magnesium (Mg) and Aluminum (Al). The Si ratio of these compounds with Sodium (Na) and Al indicates feldspar and clay mineral compounds (Shao *et al.* 2007). These results were similar to the findings of the research of Bhardwaj *et al.* (2017) in urban and rural areas of Delhi, India; Kushwaha *et al.* (2013) in the Allahabad region of India. PM with a diameter of 0.4 microns had irregular, spherical, rod and crystalline shapes. These particles are observed in the samples collected in the wet season. These samples contain compounds rich in Ca, and Zn along with Al, Ti and O. This result indicates the origin of construction and urban transportation (Tiwari *et al.* 2014; Tiwari *et al.* 2015). The results of SEM analysis showed that the chemical composition of the indoor particles was similar to the outdoor particles. In some cases, there was a difference in the chemical composition of the indoor particles. This difference was related to the origin of the indoor particles produced (such as cooking and cigarette smoke).

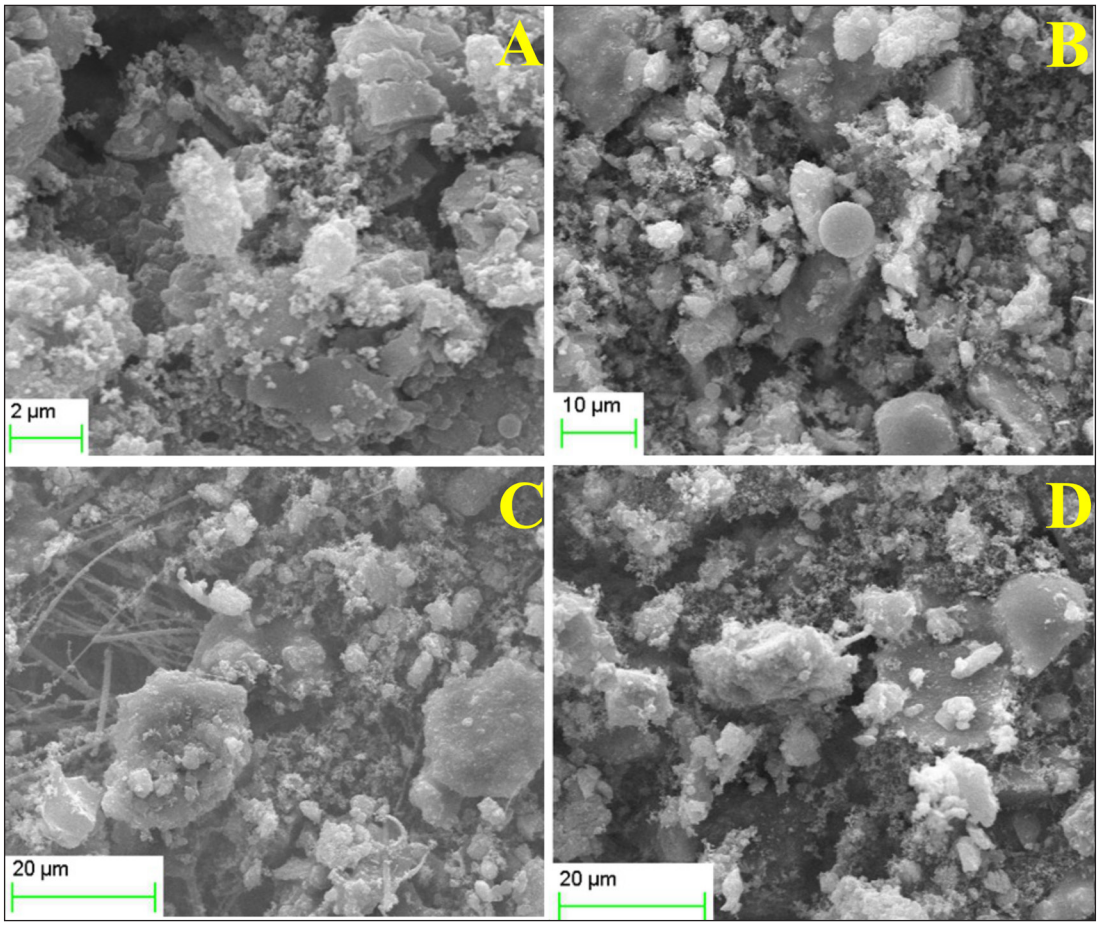

Figure 2. Image of PM collected by SEM method in the study area (A and B outdoor particles, C and D indoor particles).

The results of SEM analysis of the samples taken from the Southern areas in the study area show that most of the particles are spherical and fibrous. Most of the elements in the samples taken in this area include Ca, Fe and K, which are found in combination with Ti. Amorphous structures rich in Si and Fe, Mg and Na, were observed in PM smaller than 2.5 µm. In the samples of these areas, spherical and amorphous particles are seen in particles with a diameter greater than 0.4 micrometers with compounds rich in K, Mg, Zn and Ti along with Si and Al. The ratio of Al and Na of these compounds with Si indicates feldspar and clay mineral compounds (Shao *et al.* 2007). PM with irregular, rod-shaped and crystalline shapes was characteristic of particles smaller than 0.4 µm collected from the characteristics of samples taken in the dry season. The size of the collected particles also varied and ranged from nanometers to several tens of micrometers. Smaller particles accumulate in the atmosphere due to collisions with other particles, forming larger particles (Papastefanou 2008). As the particle dimensions grow, their deposition and removal conditions are provided (Schiavo *et al.* 2022). Particles with irregular and amorphous shapes are of internal origin and these particles mainly include particles produced from mobile sources (Transportation), industry and fossil fuel consumption. After suspension in the atmosphere, these particles collide with surfaces form larger dimensions and precipitate cumulatively (Geng *et al.* 2011; Zhai *et al.* 2012). While particles with regular and mostly spherical shapes are of organic origin and are caused by biomass burning in the environment (Campos-Ramos *et al.* 2009; Geng *et al.* 2011). According to the results of other studies, fine particles are emitted during fuel combustion processes by industry and urban transportation, and larger particles during human activities such as dust emitted on roads by vehicles, construction and Industries are produced and disseminated (Adachi and Tainosho 2004; Viana *et al.* 2006; Oroji *et al.* 2019).

The Factors Affecting Indoor Pollution

The monthly average contribution of the factors affecting the increase in the concentration of indoor particles showed in Table 4. These results showed that natural ventilation is the most important factor in increasing the concentration of indoor particles. During the year, the average share of natural ventilation in increasing the concentration of indoor particles was more than 39%. Also, the daily activities of people living in the building play a role in increasing the concentration of indoor particles by about 12%. On average, about 19% of the indoor particle was related to cooking. The life of the building was very different in different areas of Tehran. In some areas, the difference can be as long as 40 years. Studies have shown that this factor is 23% involved in the penetration of external particles into the building. This amount was higher for older buildings. Also, in most stations, the penetration of outdoor particles into the building in the cold season was more than in the hot season. Due to the use of natural ventilation in most residential buildings in the study area, the I/O ratio of $PM_{2.5}$ and $PM_{0.4}$ was on average more than 0.752. At some stations in March, April and May the I/O ratio was over 0.965.

Table 4. Monthly average contribution of the factors affecting the increase in the concentration of indoor particle.

	Factors				
Date	**Ventilation (%)**	**Cooking (%)**	**Activity (%)**	**Smoking (%)**	**Building age (%)**
April 2021	45	15	12	8	20
May 2021	57	12	10	5	16
June 2021	36	25	10	7	22
July 2021	29	27	12	7	25
August 2020	31	17	17	8	27
September 2020	30	23	15	6	26
October 2020	32	21	14	5	28
November 2020	35	17	13	10	25
December 2020	32	22	12	9	25
January 2020	37	20	15	11	17
February 2020	42	18	16	10	14
March 2020	54	15	10	6	15

Conclusions

The results showed that internal resources are related to human activities and the intended use of space. In living environments, an important role is played by smoking and cooking, followed by heating, cleaning, and suspension systems due to human presence. In hot months like August and September, most indoor particles are brought in from outside with naturally ventilated buildings. These results showed that mechanical ventilation can reduce exposure to outdoor particles in residential buildings. This crisis will be seen in the future with the development of common diseases among the persons. Prolonged exposure to atmospheric particles inside and outside the workplace and living environment can lead to respiratory and heart disease. Creating awareness and education among the people, renovating places, and using modern mechanical heating, cooling, and air conditioning systems can control the occurrence of health problems to some extent.

Acknowledgments

I would like to thank Mr. Hossein Yosefi in NSCTR institute for his insight and direction on this project.

Reference

Abramesko V, Tartakovsky L (2017). Ultrafine particle air pollution inside diesel-propelled passenger trains. *Environmental Pollution 226*: 288-296. **https://doi.org/10.1016/j.envpol.2017.03.072**

Adachi K, Tainosho Y (2004). Characterization of heavy metal particles embedded in tire dust. *Environmental international*. 30(8):1009-17. DOI: 10.1016/j.envint.2004.04.004

Alizadeh-Choobari O, Bidokhti AA, Ghafarian P, Najafi MS (2016). Temporal and spatial variations of particulate matter and gaseous pollutants in the urban area of Tehran. *Atmospheric Environment 141*:443-53. DOI: 10.1016/j.atmosenv.2016.07.003

Alikhani Faradonbeh M, Mardani G, Raeisi Shahraki H (2021). Longitudinal Trends of the Annual Exposure to PM2.5 Particles in European Countries. *Scientifica*, 2021. doi:10.1155/2021/8922798

Agudelo-Castañeda DM, Teixeira EC, Braga M, *et al.* (2019). Cluster analysis of urban ultrafine particles size distributions. *Atmospheric Pollution Research 10*(1):45-52. DOI:10.1016/j.apr.2018.06.006

Arhami M, Shahne MZ, Hosseini V, Haghighat NR, Lai AM, Schauer JJ (2018). Seasonal trends in the composition and sources of PM2.5 and carbonaceous aerosol in Tehran, Iran. *Environmental Pollution* 2018; 239: 69-81 DOI: 10.1016/j.envpol.2018.03.111

Bourdrel T, Bind MA, Béjot Y, Morel O, Argacha JF (2017). Cardiovascular effects of air pollution. *Arch Cardiovasc Dis* 110(11): 634-642 DOI: 10.1016/j.acvd.2017.05.003

Bhardwaj P, Singh BP, Pandey AK, Jain VK, Kumar K (2017). Characterization and Morphological Analysis of summer and Wintertime PM2.5 Aerosols over Urban-Rural Locations in Delhi-NCR. *Int Journal of Applied Environmental Science 12*(5): 1009-1030.

Bhangar S, Mullen NA, Hering SV, Kreisberg NM, Nazaroff WW (2011). Ultrafine particle concentrations and exposures in seven residences in northern California. *Indoor air*. 21(2):132-44. DOI: 10.1111/j.1600-0668.2010.00689.x

Braniš M, Šafránek J. (2011). Characterization of coarse particulate matter in school gyms. *Environmental Research*. 111(4):485-91. DOI: 10.1016/j.envres.2011.03.010

Brunekreef B, Janssen NA, de Hartog JJ, *et al.* (2005). Personal, indoor, and outdoor exposures to PM2.5 and its components for groups of cardiovascular patients in Amsterdam and Helsinki. *Research report (Health Effects Institute)* (127):1-70.

Campos-Ramos A, Aragón-Piña A, Galindo-Estrada I, *et al.* (2009). Characterization of atmospheric aerosols by SEM in a rural area in the western part of Mexico and its relation with different pollution sources. *Atmospheric Environment 43*(39):6159-6167. DOI:10.1016/j.atmosenv.2009.09.004

Chen C, Zhao Y, Zhang Y, Zhao, B (2017). Source strength of ultrafine and fine particle due to Chinese cooking. *Procedia Engineering 205*: 2231-2237. **https://doi.org/10.1016/j.proeng.2017.10.062**

Dalmora AC, Ramos CG, Querol X, *et al.* (2016). Nanoparticulate mineral matter from basalt dust wastes. *Chemosphere 144*:2013-2017. DOI: 10.1016/j.chemosphere.2015.10.047

Dias CL, Oliveira ML, Hower JC, *et al.* (2014). Nanominerals and ultrafine particles from coal fires from Santa Catarina, South Brazil. *International Journal of Coal Geology*, 122:50-60. DOI:10.1016/j.coal.2013.12.011

Domhagen F, Wahlgren P, Hagentoft CE (2022). Impact of weather conditions and building design on contaminant infiltration from crawl spaces in Swedish schools—Numerical modeling using Monte Carlo method. *In Building Simulation 15*(5)845-858. **https://doi.org/10.1007/s12273-021-0832-5**

Du Y, Xu X, Chu M, Guo Y, Wang J. (2016). Air particulate matter and cardiovascular disease: the epidemiological, biomedical and clinical evidence. *Journal of thoracic disease*. 8(1):E8. DOI: 10.3978/j.issn.2072-1439.2015.11.37

Gao, R, Sang N (2020). Quasi-ultrafine particles promote cell metastasis via HMGB1-mediated cancer cell adhesion. *Environmental Pollution 256*: 113390. DOI: 10.1016/j.envpol.2019.113390

Geng H, Ryu J, Maskey S, Jung HJ, Ro CU (2010). Characterization of individual aerosol particles collected during a haze episode in Incheon, Korea using the quantitative ED-EPMA technique. *Atmospheric Chemistry and Physics Discussions 10*(26):641-26. **https://doi.org/10.5194/acp-11-1327-2011**

Goel A, Kumar P (2015). Characterisation of nanoparticle emissions and exposure at traffic intersections through fast–response mobile and sequential measurements. *Atmospheric Environment 107*: 374-390. **https://doi.org/10.1016/j.atmosenv.2015.02.002**

Habre R, Zhou H, Eckel SP, *et al.* (2018). Short-term effects of airport-associated ultrafine particle exposure on lung function and inflammation in adults with asthma. *Environment international*, 118:48-59. DOI: 10.1016/j.envint.2018.05.031

Halek F, Kianpour-Rad M, Kavousirahim A (2010a). Seasonal variation in ambient PM mass and number concentrations (case study: Tehran, Iran). *Environmental monitoring and assessment*, 169(1):501-507. DOI: 10.1007/s10661-009-1192-2

Halek F, Keyanpour-Rad M, Kavousi A (2010b). Dependency of polycyclic aromatic hydrocarbon concentrations on particle size distribution in Tehran atmosphere. *Toxicological & Environmental Chemistry 92*(5):841-853. **https://doi.org/10.1080/02772240903173320**

Heger M, Sarraf M (2018). Air pollution in Tehran: Health costs, sources, and policies. World Bank

Hu, R., Xu, Q., Wang, S., *et al.* (2020). Chemical characteristics and sources of water-soluble organic aerosol in southwest suburb of Beijing. *Journal of Environmental Science 95*: 99-110. DOI:10.1016/j.jes.2020.04.004

Isaev E, Ajikeev B, Shamyrkanov U (2022). Impact of Climate Change and Air Pollution Forecasting Using Machine Learning Techniques in Bishkek. *Aerosol and Air Quality Research 22*: 210336.

Islam N, Rabha S, Silva LF, Saikia BK (2019). Air quality and PM10-associated poly-aromatic hydrocarbons around the railway traffic area: statistical and air mass trajectory approaches. *Environmental Geochemistry and Health 41*(5): 2039-2053. DOI:10.1007/s10653-019-00256-z

Kecorius S, Kivekäs N, Kristensson A, *et al.* (2016). Significant increase of aerosol number concentrations in air masses crossing a densely trafficked sea area. *Oceanologia 58*(1):1-12. **https://doi.org/10.1016/j.oceano.2015.08.001**

Kushwaha R, Hazarika N, Srivastava A (2013). SEM-EDX analysis of size segregated particulate matter in Allahabad located in north India. *International Journal of Advance Research1*(5): 248-255.

Ji W, Zhao B (2015). Contribution of outdoor-originating particles, indoor-emitted particles and indoor secondary organic aerosol (SOA) to residential indoor PM2.5 concentrations: A model-based estimation. *Building and Environment 90*:196-205. DOI:10.1016/j.buildenv.2015.04.006

Juginović A, Vuković M, Aranza I, Biloš V. (2021). Health impacts of air pollution exposure from 1990 to 2019 in 43 European countries. *Scientific Reports*. 11(1):22516. **https://doi.org/10.1038/s41598-021-01802-5**

Li Z, Zhou R, Li Y, *et al.* (2021). Characteristics and Sources of Organic Aerosol Markers in PM2.5. *Aerosol and Air Quality Research 21*:210180. **https://doi.org/10.4209/aaqr.210180**

Lim JM, Jeong JH, Lee JH, *et al.* (2011). The analysis of PM2.5 and associated elements and their indoor/outdoor pollution status in an urban area. *Indoor Air* (2):145-55. DOI: 10.1111/j.1600-0668.2010.00691.x

Liu X, Pan X, Wang Z, *et al.* (2020). Chemical characteristics and potential sources of PM2.5 in Shahe city during severe haze pollution episodes in the winter. *Aerosol and Air Quality Research 20*(12):2741-2753. **https://doi.org/10.4209/aaqr.2020.03.0124**

Møller KL, Brauer C, Mikkelsen S, (2020). Cardiovascular disease and long-term occupational exposure to ultrafine particles: A cohort study of airport workers. *International Journal of Hygiene and Environmental Health 223*(1):214-219. DOI: 10.1016/j.ijheh.2019.08.010

Mellouki A, George C, Chai F, *et al.* (2020). SI: Climate Friendly Air Pollution Control: Sources, Processes, Impacts, and Regulation Preface. *Environmental Science 95*: 1-1.

Meng QY, Turpin BJ, Korn L *et al.* (2005). Influence of ambient (outdoor) sources on residential indoor and personal PM2.5 concentrations: analyses of RIOPA data. *Journal of Exposure Science & Environmental Epidemiology 15(1)*:17-28. DOI: 10.1038/sj.jea.7500378

Meza-Figueroa, D., Pedroza-Montero, M., Barboza-Flores, M., Navarro-Espinoza, S., Ruiz-Torres, R., Robles-Morúa, A., Romero, F., Schiavo, B., González-Grijalva, B., Acosta-Elias, M. and Mendoza-Córdova, A. (2021). Identification of refractory zirconia from catalytic converters in dust: An emerging pollutant in urban environments. *Science of the Total Environment*, 760, p.143384. **https://doi.org/10.1016/j.scitotenv.2020.143384**

Mullen NA, Bhangar S, Hering SV, Kreisberg NM, Nazaroff WW. (2011). Ultrafine particle concentrations and exposures in six elementary school classrooms in northern California. *Indoor Air*. 21(1):77-87. DOI: 10.1111/j.1600-0668.2010.00690.x

Nho R (2020). Pathological effects of nano-sized particles on the respiratory system. *Nanomedicine: Nanotechnology, Biology and Medicine 29*: 102242. DOI: 10.1016/j.nano.2020.102242

Oroji B, Solgi E, Sadighzadeh A (2018a). Recognition of the source and nature of atmospheric aerosols in Tehran, Iran. *Aerosol Air Quality Research 18*(8): 2131-2140. **https://doi.org/10.4209/aaqr.2018.03.0098**

Oroji B, Sadighzadeh A, Solgi E, Oliaei MS (2021). Impact of air quality on students' behavior in the Educational Centers. *Air Quality, Atmosphere & Health 14*(6): 793-806. DOI:10.1007/s11869-021-00979-y

Oroji B, Sadighzadeh A, Solgi E, *et al.* (2019). Size distribution and chemical composition of indoor and outdoor particles in lab building. *Journal of Air Pollution and Health 4*(1): 15-26. **https://doi.org/10.18502/japh.v4i1.600**

Oroji B, Solgi E, Sadighzadeh A (2018). Characterization and morphological analysis of aerosols in Tehran traffic zone. *Journal of air pollution and Health 3*(1):9-16.

Ortega-Rosas CI, Meza-Figueroa D, Vidal-Solano JR, González-Grijalva B, Schiavo B. (2021). Association of airborne particulate matter with pollen, fungal spores, and allergic symptoms in an arid urbanized area. *Environmental Geochemistry and Health*. 43:1761-82. DOI: 10.1007/s10653-020-00752-7

Parajuli I, Lee H, Shrestha KR (2016). Indoor air quality and ventilation assessment of rural mountainous households of Nepal. *International Journal of Sustainable Built Environment 5*(2):301-11. DOI:10.1016/j.ijsbe.2016.08.003

Papastefanou C (2008). Radioactive aerosols. *Radioactivity in the Environment 12*:11-58.

Ramírez O, da Boit K, Blanco E, Silva LF (2020). Hazardous thoracic and ultrafine particles from road dust in a Caribbean industrial city. *Urban Climate 33*:100655. DOI:10.1016/j.uclim.2020.100655

Ramirez-Leal R, Valle-Martinez, M, Cruz-Campas M (2014). Chemical and morphological study of PM10 analysed by SEM-EDS. *Air Pollution 3*(04):121. DOI:10.4236/ojap.2014.34012

Ranft U, Schikowski T, Sugiri D, Krutmann J, Krämer U (2009). Long-term exposure to traffic-related particulate matter impairs cognitive function in the elderly. *Environmental research*. 109(8):1004-11. DOI: 10.1016/j.envres.2009.08.003

Rojas JC, Sánchez NE, Schneider I, *et al.* (2019). Exposure to nanometric pollutants in primary schools: environmental implications. *Urban Climate 27*:412-419. DOI:10.1016/j.uclim.2018.12.011

Schneider IL, Teixeira EC, Oliveira LFS, Wiegand F (2015). Atmospheric particle number concentration and size distribution in a traffic–impacted area. *Atmospheric Pollution Research 6*(5): 877-885. **https://doi.org/10.5094/APR.2015.097**

Schneider IL, Teixeira EC, Agudelo-Castañeda DM, et al (2016). FTIR analysis and evaluation of carcinogenic and mutagenic risks of nitro-polycyclic aromatic hydrocarbons in PM10. *Science Total Environmental 541*:1151-1160. DOI: 10.1016/j.scitotenv.2015.09.142

Schiavo, B., Meza-Figueroa, D., Vizuete-Jaramillo, E., Robles-Morua, A., Angulo-Molina, A., Reyes-Castro, P.A., Inguaggiato, C., Gonzalez-Grijalva, B. and Pedroza-Montero, M., (2022). Oxidative potential of metal-polluted urban dust as a potential environmental stressor for chronic diseases. *Environmental Geochemistry and Health*, pp.1-22. **https://doi.org/10.1007/s10653-022-01403-9**

Schiavo B, Meza-Figueroa D, Pedroza-Montero M, Vidal-Solano J, González-Grijalva B, Navarro-Espinoza S, Romero F, Hernández E, Gutiérrez-Ruiz ME, Ceniceros-Gómez AE. (2021). In vitro assessment oral and respiratory bioaccessibility of Mn in school dust: Insight of seasonality in a semiarid environment. *Applied Geochemistry*. 134:105102. **https://doi.org/10.1016/j.apgeochem.2021.105102**

Silva LF, Milanes C, Pinto D, *et al.* (2020a). Multiple hazardous elements in nanoparticulate matter from a Caribbean industrialized atmosphere. *Chemosphere 239*:124776. **https://doi.org/10.1016/j.chemosphere.2019.124776**

Silva LF, Pinto D, Neckel A, *et al.* (2020b). Atmospheric nanocompounds on Lanzarote Island: Vehicular exhaust and igneous geologic formation interactions. *Chemosphere 254*:126822. **https://doi.org/10.1016/j.chemosphere.2020.126822**

Steinfeld B, Scott J, Vilander G, *et al.* (2015). The role of lean process improvement in implementation of evidence-based practices in behavioral health care. *The Journal of Behavioral Health Services & Research 42*(4):504-518. DOI: 10.1007/s11414-013-9386-3

Soppa VJ, Shinnawi S, Hennig F, *et al.* (2019). Effects of short-term exposure to fine and ultrafine particles from indoor sources on arterial stiffness–A randomized sham-controlled exposure study. *International Journal of Hygiene and Environmental Health*, 222(8):1115-1132. DOI: 10.1016/j.ijheh.2019.08.002

Stacey, B., 2019. Measurement of ultrafine particles at airports: A review. *Atmospheric Environment*, 198:463-477. DOI:10.1016/j.atmosenv.2018.10.041

Tiwari S, Pipal AS, Hopke PK, *et al.* (2015). Study of the carbonaceous aerosol and morphological analysis of fine particles along with their mixing state in Delhi, India: a case study. *Environmental Science Pollution Research 22*(14): 10744-10757. DOI: 10.1007/s11356-015-4272-6

Tiwari S, Bisht DS, Srivastava AK, *et al.* (2014). Variability in atmospheric particulates and meteorological effects on their mass concentrations over Delhi, India. *Atmospheric Research 145*: 45-56. **https://doi.org/10.1016/j.atmosres.2014.03.027**

Thangavel P, Park D, Lee YC. (2022). Recent insights into particulate matter (PM2.5)-mediated toxicity in humans: an overview. *International journal of environmental research and public health*. 19(12):7511. doi: 10.3390/ijerph19127511

Viana M, Querol X, Alastuey A (2006). Chemical characterization of PM episodes in North-Eastern Spain. *Chemosphere 62*: 947–956. **https://doi.org/10.1016/j.chemosphere.2005.05.048**

Voss U, Uller L, Ansar S, *et al.* (2022). Airway exposure to urban aerosolized PM2.5 particles induce neuroinflammation and endothelin-mediated contraction of coronary arteries in adult rats. *Environmental Advances 8*:100184. **https://doi.org/10.1016/j.envadv.2022.100184**

Xiao X, Cao L, Wang R, Shen ZX, Cao YX (2016). Airborne fine particulate matter alters the expression of endothelin receptors in rat coronary arteries. *Environmental Pollution 218*: 487-496. DOI: 10.1016/j.envpol.2016.07.028

Yang L, Li C, Tang X. (2020). The impact of PM2.5 on the host defense of respiratory system. *Frontiers in cell and developmental biology*. 8:91. **https://doi.org/10.3389/fcell.2020.00091**

Zamberlan DC, Halmenschelager PT, Silva LFO, Da Rocha JBT (2020). Copper decreases associative learning and memory in Drosophila melanogaster. *Science Total Environmental 710*: 135306. **https://doi.org/10.1016/j.scitotenv.2019.135306**

Zhai YB, Fu ZM, Wang LF (2012). Characteristic, Composition, and Sources of TSP Investigated by HRTEM/EDS and ESEM/EDS. Environmental Monitoring Assessment 184: 6693-6707. DOI: 10.1007/s10661-011-2452-5

Zhao X, Zhao X, Liu P, Ye C, (2020). Pollution levels, composition characteristics and sources of atmospheric PM2.5 in a rural area of the North China Plain during winter. Journal of Environmental Science 95: 172-182. DOI: 10.1016/j.jes.2020.03.053

Zhao B, Wang M, Song W, Ma H, *et al.* (2022). Increasing risk of gestational diabetes and preeclampsia associated with long-term exposure effects of air pollution. Air Quality, Atmosphere & Health 11:1-2. DOI: 10.1007/s11356-022-20594-3

Zhou X, Cai J, Chen R, Wang C, Zhao A, *et al.* (2018). Estimation of residential fine particulate matter infiltration in Shanghai, China. Environmental pollution 233:494-500. DOI: 10.1016/j.envpol.2017.10.054